The Simulated Effect of the Lightning First Short Stroke Current on a Multi-layered Cylindrical Model of the Human Leg

Yuan-chun Harry Lee

A dissertation submitted to the Faculty of Engineering and the Built Environment, University of the Witwatersrand, Johannesburg, in fulfilment of the requirements for the degree of Master of Science in Engineering.

Johannesburg, 2015

DECLARATION

I declare that this dissertation is my own unaided work. It is being submitted for a degree of Master of Science in Engineering to the University of the Witwatersrand, Johannesburg. It has not previously been submitted for any degree or examination to any other university.

_____ _____

Yuan-chun Harry Lee Date

ABSTRACT

This research investigates the effects of the frequency components of the lightning First Short Stroke (FSS) on the current pathway through human tissues using frequency domain analysis. A Double Exponential Function (DEF) is developed to model the FSS with frequency components in the range 10 Hz $\sim$ 100 kHz. Human tissues are simulated using Finite Element Analysis (FEA) in COMSOL and comprises of two types of models: Single Layer Cylindrical Model (SLCM) and Multi-layered Cylindrical Model (MLCM). The SLCM models 54 human tissues independently and the MLCM models the human leg with five tissue layers: bone marrow, cortical bone, muscle, blood and fat.

Three aspects are analysed: current density, complex impedance and power dissipation. From the SLCM results, aqueous tissues have the lowest impedances and tissue heat dissipation is proportional to tissue impedance. Results from the MLCM show that 85% of the FSS current flows through muscle, 11% flows through blood, 3.5% through fat and the rest through cortical bone and bone marrow. From the results, frequency dependent equivalent circuit models consisting of resistors and capacitors connected in series are proposed.

The simulation results are correlated with three main clinical symptoms of lightning injuries: neurological, cardiovascular and external burns. The results of this work are applicable to the analysis of High Voltage (HV) injuries at power frequencies.

ACKNOWLEDGEMENTS

The author would like to acknowledge with gratitude the aid rendered by both Prof. Ian Jandrell and Prof. David Rubin. Gratitude is given to Eskom for their support of the High Voltage Engineering Research Group at Wits University through TESP. The author would also like to express gratitude to the Department of Trade and Industry (DTI) for THRIP funding and to thank the National Research Foundation (NRF) for direct funding of the research group.

Contents

LIST OF FIGURES

LIST OF TABLES

Glossary

COMSOL	A multiphysics simulation platform.
Maxwell's Equations	Four partial differential equations put together by Maxwell that forms the basis of electric circuits.

Acronyms

AC	Alternating Current
DEF	Double Exponential Function
EF	Electric Field
EMF	Electric and Magnetic Field
FDTD	Finite Difference Time Domain
FEA	Finite Element Analysis
FSS	First Short Stroke
HV	High Voltage
IM	Impedance Method
LEMP	Lightning Electromagnetic Pulse
MLCM	Multi-layered Cylindrical Model
MRI	Magnetic Resonance Imaging
SAR	Specific Absorption Rate
SLCM	Single Layer Cylindrical Model
VLF	Very Low Frequency

List of Symbols

σ_e	Effective Conductivity
$error_R$	Resistance Absolute Error
$error_X$	Reactance Absolute Error
$error_Z$	Impedance Magnitude Absolute Error
δ	Loss Tangent
R_{ef}	Resistance from EF approach
μ_r	Relative Permeability
ϵ_r	Relative Permittivity
R_{emf}	Resistance from EMF approach
X_{ef}	Reactance from EF approach
X_{emf}	Reactance from EMF approach
Z_{ef}	Impedance Magnitude from EF approach
Z_{emf}	Impedance magnitude from EMF approach

Chapter 1

Introduction

The First Short Stroke (FSS) is considered an impulse current with several frequency components associated with it [1]. This work uses frequency domain analysis to investigate the effects of these frequency components on the current pathway through the human body when struck by the FSS. The frequency components are extracted from an existing FSS model and applied to the proposed human tissue models, and the frequency dependant impedances are calculated. The current pathway is determined to be inversely proportional to the impedances.

Simulated models of various human tissues for the evaluation of tissue impedances under different frequency conditions are proposed. Two types of tissue models are developed: Single Layer Cylindrical Model (SLCM) and Multi-layered Cylindrical Model (MLCM). SLCMs are used to simulate 54 human tissues individually whereas MLCM is used to simulate a human leg and examines the effects of multiple tissues on the current pathway. Two simulation approaches, Electric and Magnetic Field (EMF) and Electric Field (EF), are performed on the SLCM. The results from the simulations of the SLCM and MLCM are compared with symptoms of lightning injuries and correlations are discussed.

Chapter 2 discusses the background on FSS waveforms, lightning injuries and human body models. The different FSS models are described and compared. The waveform, current magnitude and duration of each model is detailed. Lightning injuries are compared with HV injuries and possible causes are discussed. Present modelling techniques of the human body are mentioned.

Chapter 3 outlines the approach taken in the design and simulation of the human tissue models. The rationale for this research is discussed along with the research objectives.

Chapter 4 examines the FSS model and details the simulation designs for both the SLCM and the MLCM. The EF and EMF simulation approaches are presented.

Chapter 5 discusses simulation results of the SLCM and the MLCM. Comparison between the EF and EMF simulation approaches are conducted. The feasibility of using the simulation results in the prediction of current pathway is described. The results are compared with existing studies and findings of lightning injuries.

Chapter 6 and 7 concludes the work by reviewing the study along with future recommendations and a summary of the findings.

Appendix A derives Maxwell's Equations for the use in FEA. The differential equations required to solve the electromagnetic fields for the specific application of this work is given.

Appendix B includes results obtained from the SLCM. Three aspects of the results are presented: current densities, complex impedances and power losses.

Appendix C details the image segmentation process in which the structure of the MLCM is derived. This includes the construction and volumetric analysis of human leg Magnetic Resonance Imaging (MRI) images and models.

Appendix D presents a published conference paper that was submitted to the *International Conference on Lightning Protection* in October 2014 [6]. This paper provides a background on the use of dielectric properties of human tissues in the analysis of lightning injuries.

Chapter 2

Background

Overview

This chapter discusses the background and existing research on the consequences of lightning strikes on humans as well as approaches to explain these phenomena. This chapter consists of four parts. Firstly, the lightning current waveform is discussed and existing models are presented. Secondly, lightning injury mechanisms are detailed with analysis of causes and consequences of lightning injuries. Thirdly, lightning injuries are compared to HV injuries with a discussion on the differences and similarities between them. Lastly, various approaches of modelling the human body are considered.

Section 2.1 discusses two popular models of the lightning short stroke as well as current methods in lightning simulation.

Section 2.2 presents statistics on the fatalities of lightning injuries. Six lightning injury mechanisms are discussed followed by a few case studies. Clinical symptoms of lightning injuries are discussed and categorised based on medical case reports.

Section 2.3.1 details the differences and similarities between lightning injuries and HV injuries.

Section 2.4 discusses the electrical properties of human tissues. Existing human body models including electric circuit models of the human body and the numerical dosimetry models of the human body are considered.

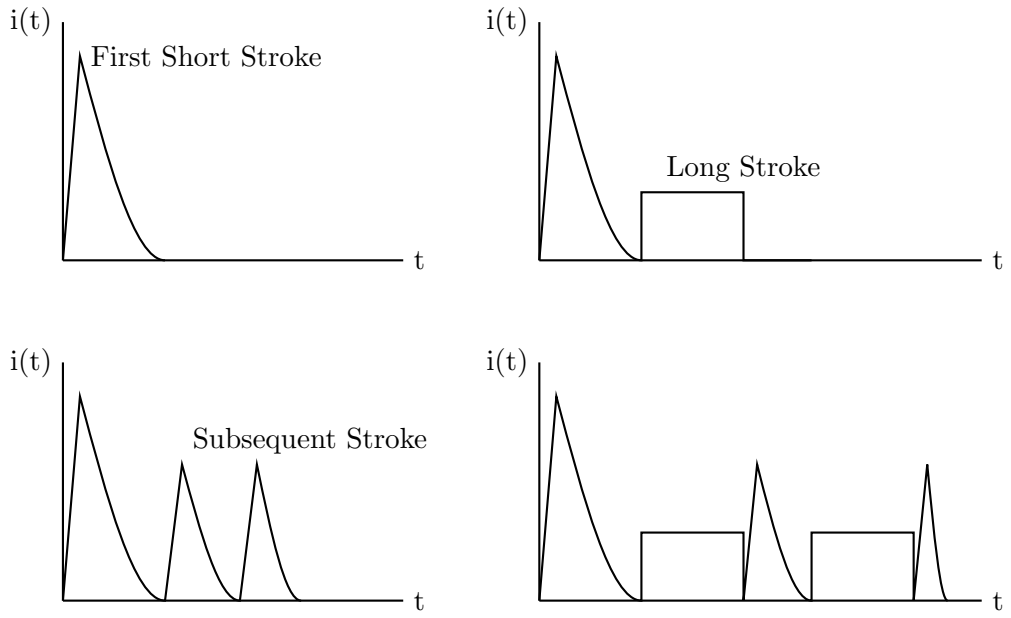

Figure 2.1: Various types of stroke components of downward flashes. Adapted from Figure A.3 [1]

2.1 Lightning Model

In essence, lightning is a visual manifestation of an extremely large electric discharge [7]. According to the IEC-62305 Std. [1], a lightning flash to earth is composed of one or more short strokes and/or long strokes. A short stroke is defined as part of the lightning flash which corresponds to an impulse current, and a long stroke is defined as part of the lightning flash which corresponds to a continuing current [1]. The different stroke combinations within cloud-to-ground negative downward flashes are shown in Figure 2.1. Only the cloud-to-ground negative downward lightning flash is considered as this is the most frequent type of lightning that results in lightning injuries [8].

Lightning is considered and modelled as a current source which suggests that the magnitude of current is independent to the resistance of the object that is struck [9]. Golde [10] referred to the current of lightning as the most crucial parameter of the lightning discharge. The FSS is considered the most significant part of the lightning flash as it causes most of the destruction to electrical systems [11]. From Figure 2.1, it can be seen that the FSS has a much higher peak value compared to the other strokes. FSS is known to be the most powerful lightning process in terms of the local energy dissipation and electromagnetic radiation [12]. Due to this, when a person is struck by lightning, the effects of the FSS on lightning injuries may be expected to be the most important aspect of the investigation.

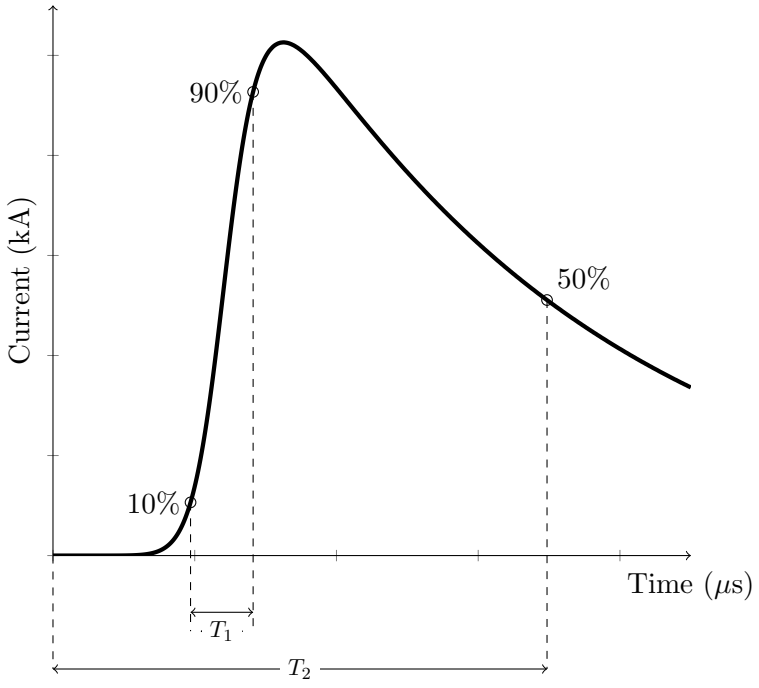

Figure 2.2: Typical lightning short stroke current waveform

To investigate the effects of the FSS on lightning injuries, the FSS current waveform needs to be surveyed and modelled. Since the FSS resembles an impulse as seen in Figure 2.1, there are multiple frequency components associated with it. A model in the time domain needs to be established such that a subsequent model in the frequency domain can be derived and the frequency components analysed. From this, the effects of the frequency components on the current pathway of the FSS can be examined.

2.1.1 Lightning Current Waveform in the Time Domain

Not all lightning occurrences are the same; the shape and magnitude of the lightning current waveform depends on various factors: terrain, electrical properties of the object that is struck and the charge contained within the cloud [4]. Since all occurrences of lightning events are different, it is important to develop a model of the lightning strokes which best describes natural lightning and can be used for analyses.

According to IEC-62305 [1], lightning short stroke waveforms are described using the following nomenclature: T_1/T_2 μs as depicted in Figure 2.2. T_1 is the time interval between the instants where the current reaches 10% and 90% of the peak current. T_2 is the time interval between the origin and the instant when the current drops to 50% of the peak current.

There are numerous methods to model the lightning short stroke. Rakov and Uman [13] defined four classes of return stroke models: gas dynamic models, electromagnetic models, distributed-circuit models and the engineering models. Engineering models include functions which describe the spatial and temporal distribution of the FSS current at the base of the channel [13]. This allows for the calculations of the Lightning Electromagnetic Pulse (LEMP) and the lightning stroke electromagnetic fields [14]. Other return stroke models primarily represent the formation of the lightning channel and the current distribution along the channel [13]. As this work concerns the current pathway of the FSS through the human body after attachment, only the channel base current is of importance and only the engineering models are considered.

Cooray [11] compares in detail the various mathematical return stroke models used in engineering models to describe the channel base current. The most popular being the Double Exponential Function (DEF) developed by Bruce and Golde [15] and the Heidler Function [16].

Double Exponential Function (DEF)

The DEF developed by Bruce and Golde [15] is shown in Equation (2.1), where I_0 is the peak current multiplier, α and β are parameters that are obtained from the electrical charge density along the path, return velocity and the charge compound ratio and t is the time variable.

$$i(t) = I_0(e^{-\alpha t} - e^{-\beta t}) \tag{2.1}$$

There are two major limitations of the DEF waveform [17]. Firstly, the parameters I_0, α and β do not provide obvious meanings to the characteristics of the DEF waveform. Secondly, the DEF waveform produces an unrealistic rise at $t = 0$ as seen in Figure 2.3. The most significant advantage of using the DEF is that analytical integration using the Fourier transform is possible such that the waveform can be analysed in the frequency domain.

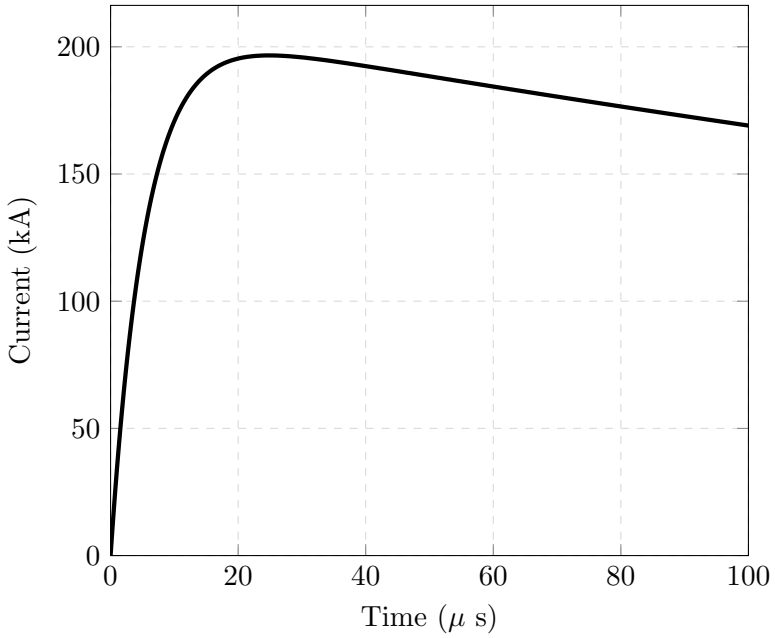

Figure 2.3: Lightning stroke model: DEF of 200 kA, 10/350 μs

Heidler Function

The Heidler function is used by the IEC-62305 to define the lightning short stroke waveform for the FSS of 10/350 μs and subsequent short stroke of 0.25/100 μs as shown in Equation (2.2) [1]. In this equation, I is the peak current, k is the correction factor, t is the time variable, τ_1 is the front time constant and τ_2 is the tail time constant. This current waveform is based on the Heidler function [16] and is plotted in Figure 2.4.

$$i(t) = \frac{I}{k} \cdot \frac{(t/\tau_1)^{10}}{1 + (t/\tau_1)^{10}} \cdot e^{(-t/\tau_2)} \tag{2.2}$$

Heidler function is widely used as it presents several improvements over other channel base current models [16]. The most significant improvement over the previously popular DEF is that the time derivative of the Heidler function at $t = 0$ does not have a discontinuity [16]. The disadvantage of the Heidler function is that it cannot be analytically integrated using Fourier transformations, only numerical approximations can be carried out to estimate the integral of the Heidler function [16].

Several studies have been conducted in the approximation of the Heidler function such that it can be transformed into the frequency domain. Slavko and Lovric [18] approximate the Heidler function by linearly combining exponential functions in the time domain which can then be analytically transformed into the frequency domain. Similar work include: Javor and Rancic [19] who introduced the CBC function

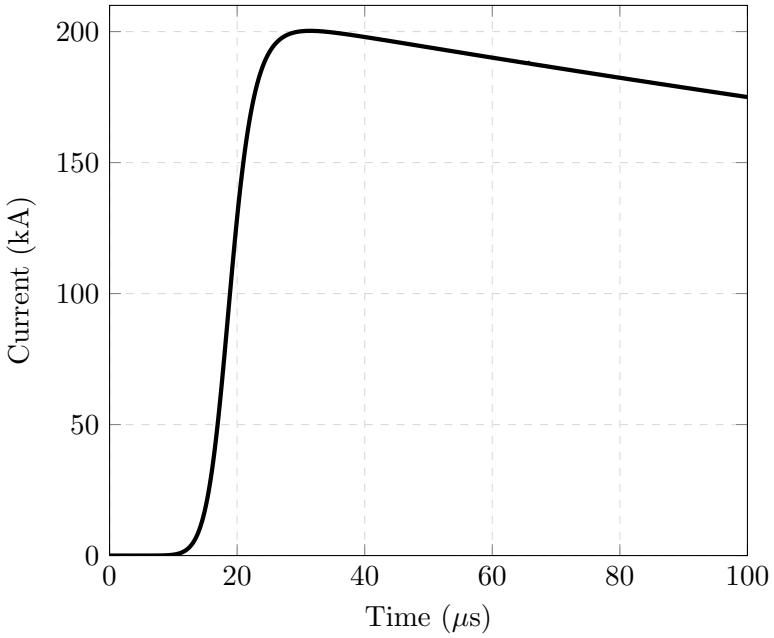

Figure 2.4: Lightning stroke model: Heidler Function of 200 kA, 10/350 μs

with Javor [14] further defines the NCBC function; Feizhou and Shanghe [20] who proposed the Pulse function which is time integrable. These studies mostly use the DEF as the foundation for the approximation of the Heidler function.

2.1.2 Lightning Studies in the Frequency Domain

Since the FSS resembles an impulse as seen in Figure 2.1 and Figure 2.2, multiple frequency components are associated with it. These frequency components arise from the rapid rate of change of current in a short duration. The FSS can be decomposed into these frequency components and analysed from the frequency spectrum.

The frequency domain transformation of the lightning stroke is required in calculations of the transient analysis of electromagnetic phenomena such as lightning protection and grounding grid analysis [18].

Several studies have focused on analysing the lightning strokes in the frequency domain [21–23]. These studies have primarily focused on the atmospheric measurements of the electromagnetic radiation from the lightning strokes during lightning events.

2.2 Lightning Injuries

A topic that has fascinated scientists and engineers for years is the mechanisms by which objects are struck by lightning, particularly when the consequences are human injuries. The effects of lightning strikes on humans have been surveyed on a broad scale and a myriad of findings as well as postulations have been suggested. These findings include work from both the medical field as well as the engineering field.

2.2.1 Statistics

Holle [24–26] estimates that lightning results in 6 deaths per million per year worldwide which translates to 24,000 deaths and 240,000 injuries per annum. In South Africa, there are limited published data on lightning morbidity [27]. Blumenthal et al. [27] estimated that there are up to 100 lightning related fatalities per annum in South Africa. They also estimated that there are at least 400-500 clinically admitted lightning strike survivors annually. This may be due to the considerable distribution of the rural population and the result of weakly constructed dwellings. The Highveld region of South Africa, which is a predominantly urban region, has an annual incidence of 6.3 deaths per million [28].

2.2.2 Mechanisms of lightning injuries

Extensive studies have been undertaken on the mechanisms of lightning strikes and related injuries. The four well known classic mechanisms of lightning injuries are: *direct strike, contact voltage, side flash* and *step voltage* [29]. In the analysis of these mechanisms, the electrical impedance of the body and the current pathway established has been the main focus from the electrical and medical perspective respectively [29]. Anderson [30] and Cooper [31] described a fifth mechanism of lightning injury, which is a result of the discharge of a weak upward streamer through the body due to an unsuccessful attachment process. A sixth mechanism has been suggested by Blumenthal et al. [32], which details a blast effect termed lightning barotrauma. The first five mechanisms can be described electrically by means of voltage and current. The sixth mechanism, however, is described as a result of the shock-wave phenomenon [32]. It is important to note that since all lightning flashes are unique, injuries from lightning vary for each lightning incident. This variation is also dependant on the environment, activity of the people and the medical treatment of the injuries [4].

According to Rakov and Uman [33], lightning damage is defined by the characteristics of the lightning discharge as well as the properties of the object that is struck. When considering the characteristics of the lightning discharge, the current waveform of the lightning discharge has been the centre of interest along with electromagnetic radiation.

Rakov and Uman [33] further describe four distinguishable properties that the lightning current waveform possesses which are significant in causing lightning damage:

- Peak Current
- Maximum rate of change of current
- Integral of current over time (Charge transferred)
- Integral of current squared over time

Andrews et al. [5] state that lightning is hazardous to the human body for four reasons: high voltage, secondary heat production, electromagnetic cellular effects and explosive force. They further stipulated that the factors which result in the severity of electrical burns are, frequency, voltage, current magnitude, resistance, current pathway and duration.

The five mechanisms of lightning injuries which involve current and voltage are detailed below:

Direct Strike

This is the mechanism of injury in which the attachment process occurs directly between the upward streamer from the victim and the downward leader of the lightning stroke [29]. The entire current discharge is delivered to the victim, however, external flash-overs may occur depending on the body resistance of the victim [9]. This is a result of the breakdown of air, in which case, the current discharge occurs over the external surface of the victim rather than internally [9].

Contact Voltage

This is the mechanism of injury in which the victim has direct contact with the conductive object that has been struck. A potential difference between the contact point of the victim with the conductive object and earth is produced [29] which results in a current flow.

Side Flash

This is the mechanism of injury in which the victim stands in close proximity to the point of strike and the current travels across the air gap and conducts through the victim to earth [29]. This occurs as the developed voltage of the object which is struck causes electrical discharge due to the electrical breakdown of air. This is dependent on the air-gap distance and the body resistance of the victim [9].

Step Voltage

According to Darveniza [9], when a strike occurs near the victim, the current discharge flows into the earth and away from the point of strike. This initiates concentric equipotential lines around the point of strike. The adjacent points of contact of the victim with the ground will have differing potentials with respect to the point of strike. This difference in potential between the adjacent points of contact results in current flowing through these points. The magnitude of the potential difference depends on the current magnitude, the soil resistivity, the radial distance from the point of strike and the length of the step.

Upward Streamer

As the downward leader progresses towards earth, there may be instances in which several upward streamers are formed. However, as the attachment process occurs with one of these upward streamers, the unattached upward streamer/s flows back down the victim/s which initiated the upward streamer [30, 31].

2.2.3 Current Discharge Pathways and Duration

From the five mechanisms of lightning injuries mentioned above, it can be seen that the current magnitude and the current pathway is the main cause of lightning injuries.

According to Lee [29], the extent of lightning injuries is dependent on the current discharge pathway through the body when struck by lightning. Hence, the analysis and identification of the critical structures (organs) which are affected along this pathway is necessary. In the case of a direct strike or side flash, the current generally traverses the body from the head, neck and shoulders to the feet.

According to Andrews et al. [5], there are two routes for the lightning current pathway: through and over the human body. The latter is the external flash-over mentioned in Section 2.2.2. While the occurrence of the external flash-over is only speculation and can be mathematically modelled, no human body model considering the flash-over has been developed which can quantify the current through and over the human body.

2.2.4 Clinical symptoms of lightning injuries

Two fatal consequences of lightning strikes are considered: ventricular fibrillation[1] and respiratory arrest. The onset of ventricular fibrillation is the result of current passing through the heart; respiratory arrest is the result of current traversing the brain stem (respiratory centre). Ventricular fibrillation and respiratory arrest are the results of functional disturbances and usually are not associated with structural changes. Due to this, post-mortem examinations do not always suggest the exact mechanisms of death [29].

Andrews and Cooper [34] classified the clinical symptoms of lightning strike victims into nine categories. The categories which constitutes the majority of clinical symptoms and worth mentioning are: neurological, cardiovascular and external burns related injuries. This is in accordance with the findings of Pfortmueller et al. [35], stating that the three most common sites of lightning injuries are the nervous system, cardiovascular system and skin respectively. Several medical studies show similar findings [36, 37]. Internal tissue breakdown resulting in damage is rarely found, the most likely medium for current conduction is via the vascular tree or through other channels containing ionic fluid [2]. The common types of lightning injuries are listed in Table 2.1.

2.3 Comparison between High Voltage (HV) injuries and lightning injuries

Current flows through the path of least impedance. The establishment of this current path depends on various factors: the frequency of the current, the electrical properties of the encountered tissues and the points of contact with the current source [38]. In the examining of electrical accidents, it is critical to determine the current pathway through the tissues in order to determine the severity of the injuries.

[1] One of the main causes of cardiac arrest. A condition in which the contraction of the ventricles are uncoordinated due to the random quivering of the cardiac muscles.

Table 2.1: Types of lightning injuries and death. Adapted from Table A.1 [4] and Andrews et al. [5].

Lightning Death	Asystole, seldom ventricular fibrillation Cardio-respiratory progression
Immediate Neurological Effects	Loss of consciousness Brain stem dysfunction Cerebellar and basal ganglion haemorrhage Peripheral neurovascular spasm Seizures
Long Term Neurological Effects	Pain syndromes Dysthesia, neuropathy Parkinsonism Neuropsychological Spinal cord change
Burns and Cutaneous Markings	Entry and exit burns Linear burn Lichtenberg figure (arborescent burn) Contact burn
Contusive Blast Injury	Exploded, torn and shredded clothing Body contusion (skin, brain, lung, bowel, etc.)
Trauma	Blow bruise laceration Fractures
Special senses	Ear and hearing injury - Tympanic membrane rupture - Tinnitus and vertigo - Deafness Eye injury - Blindness - Retinitis - Cataract - Uveal inflammation

According to Sutherland et al. [39], even though lightning injuries may resemble symptoms similar to those of HV power line injuries, they are not the same. This is further differentiated in detail by Andrews and Cooper [34].

Sutherland et al. [39] mentioned that when considering power frequency electrical injuries, human sensitivity to electric current is dependent on both the current magnitude and duration, which is similar to lightning injuries. Even though the mechanisms of injury may be similar, they are fundamentally different due to the characteristics of the current waveform. Lightning is characterised as an aperiodic

and transient impulse whereas HV electrical injuries are results of power frequency periodic sinusoids. Hence, the most important factor in discerning HV electrical injuries is the duration of exposure to the current [5].

In HV injuries, currents up to a few amperes lasting more than a few seconds may result in internal injuries as well as surface burns [40]. However, lightning injuries are normally result from stroke currents lasting a few microseconds, only the stroke currents which lasts several milliseconds (long strokes) are associated with major injuries [5]. Long strokes are able to explode trees, start fires and produce injuries similar to HV injuries [5]. The short and long term sequelae of lightning injuries tend to be of a neurological nature rather than external burns [4]. The comparison between lightning injuries and HV injuries is shown in Table 2.2.

Table 2.2: Comparison between HV injuries and lightning injuries. Adapted from [4] and [5].

	HV	**Lightning**
Voltage	$>$ 1000 V Alternating Current (AC)	30 MV Transient
Current Waveform	50/60 Hz AC	Impulsive discharge with multiple strokes
Duration of contact	Prolonged, Short if thrown	Impulsive, continuing current may occur
Pathway	Deep, internal	Flash-over
Mode of death	Ventricular fibrillation	Asystole 1° and 2°, respiratory paralysis
Burns	Severe, deep and extensive	Superficial, Minor
Lichtenburg figure	Can be present	Common
Muscle damage	Can be present	Rare
Renal consequences	Myoglobinuria and renal failure	Rare
Fasciotomy	Common and extensive	Rare

2.3.1 HV Electrical Injuries

Despite the differences, there are many similarities between the injury mechanisms of HV injuries and lightning injuries. Experiments conducted under power frequency electrical currents should not be disregarded and careful considerations are required when using HV electrical injuries data in the analysis of lightning injuries.

Two standards are used to describe the current pathway through the human body in HV injuries: IEC-60479 [40] and IEEE Std. 80 [41]. Grounding of structures are commonly designed for power frequencies since the human body is more susceptible to 50/60 Hz current than high frequency currents [41].

Bracken et al. [42] examined the current pathways through the body for electrical utility workers and developed statistical distributions of the electrical impedance of the human body. When describing the pathway impedance of the human body, there are two impedances which are considered: the impedance of the skin at the contact point and the impedance of the internal body [43]. The impedance of the internal body is lower than the impedance of the skin and can be considered as only resistive at 60 Hz [44]. The impedance of the skin at the contact point is dependant on voltage, frequency, contact area and the skin moisture and can be both resistive and capacitive. The total impedance of the body is the vectorial combination of the impedance of the internal body and the impedance of the skin [42].

IEEE Std. 80 approximates that the body has a resistance of 1 kΩ for hand-to-feet and hand-to-hand pathways depending on environmental conditions [41]. Lee and Sakis Meliopoulos [45] compared the IEC-60479 with IEEE Std. 80 and found that the IEC-60479 gives a more concise electrical shock model.

IEC-60479 [40] states that after the skin has broken down, the total body impedance approximates to that of the internal impedance and only depends to a small extent on the surface area and the dampness of the contact area. If the contact voltage on the skin rises above 200 V, the skin typically breaks down and the total impedance of the body tends towards the impedance of the internal body [44].

According to IEC-60479 [40], ventricular fibrillation threshold depends on physiological parameters (such as condition of cardiac function, structure of the body) and electrical parameters (current pathway, duration and magnitude). Besides ventricular fibrillation, mechanisms affecting respiration are fatal as well. Death may occur when current traverses the spinal cord or the respiratory control centre in the brain. Contact with high magnitude and short duration currents can damage cells through a non thermal effect called electroporation. Electroporation is caused from the breakdown of the cell membrane as a result of high transmembrane electric fields. Cell necrosis may occur and tissues may be irreversibly damaged.

Data from extensive work done by Dalziel and Lee [46] [47] on electric shock hazards is still used today. Two fatal injuries from HV contact are: *respiratory paralysis* and *ventricular fibrillation*. Human susceptibility to electric current depends on the current magnitude which is determined by factors such as body weight and shock duration. Currents flowing through nerve centres in the brain may inhibit respiratory functions which do not recover for a long time even when the current source is removed.

Dalziel [48] believed that the danger of impulse currents is essentially the result of the energy contained in the discharge. Factors such as the wave front of the current impulse and the duration of the impulse are of less importance. Although HV injuries result in the immense destruction of tissues at contact locations, the most crucial property that results in fatality is the current that flows through the body.

2.4 Human Body Model

2.4.1 Circuit Model of the Human Body

The human body is often modelled using electric circuit analogy [39, 44, 49, 50]. Modelling the human body using electrical circuit theory simplifies the human body and allows analysis from a purely electrical perspective. The total body impedance is a combination of the impedances of various parts of the body. Hence, the equivalent circuit model of the human body is the representation of the electrical current pathway through the body.

Human Circuit Model at Power Frequencies

Some studies only consider currents flowing through the human body at power frequencies (50/60 Hz) [39, 42, 51]. This may not be adequate in the analysis of lightning injuries as the FSS has multiple frequency components associated with it.

The IEC-60479 [40] describes the effects of AC on the human body in the range of $15 \sim 100$ Hz and considers the body impedance to be dependant on multiple factors: current path, touch voltage, current flow duration, frequency, amount of moisture on the skin, contact surface area, contact pressure and temperature. The electrical impedance of the human body within this frequency range is also detailed. The initial resistance of the human body R_0 can be considered as $1000\,\Omega$ for 95% of the human population.

Sutherland et al. [39] considers the simple human body model with two types of impedances: *skin* and *internal*. The skin has both resistance and capacitance due to its layered structure. The skin impedance Z_s is considered as a network of resistances and capacitances [40]. Hence, Z_s decreases as current or frequency increases. The current and voltage relationship is nonlinear as the impedance of the human body varies depending on the touch voltage. The internal impedance is resistive and comparable to saline at human body concentration. This value essentially depends on the current path [40]. From this model, the skin capacitance causes the impedance to decrease with increasing frequency.

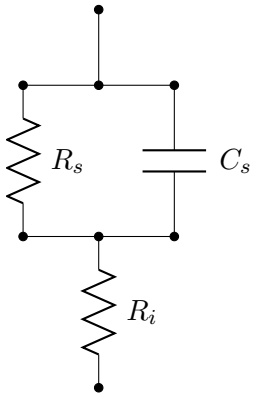

Figure 2.5: Simplified model of the human body

Gordon et al. [44] state that at lower frequencies such as power frequencies, the impedance of the body is primarily resistive and it is thus adequate to model the body as a single resistor or a network of resistors. The impedance is a function of frequency and voltage and a circuit model shown in Figure 2.5 is proposed [44], where R_s represents the resistance of the skin and C_s represents the capacitance of the skin while R_i represents the internal impedance of the body. This model illustrates that as frequency increases, the total body impedance approaches that of the internal impedance.

Kanai et al. [49] proposed a more sophisticated model which determines the average body impedance as a function of frequency in the Very Low Frequency (VLF) to Medium Frequency (MF) range (10 kHz $\sim$ 3 MHz). The proposed equivalent circuit model for individual tissues in the 10 kHz $\sim$ 10 MHz range is shown in Figure 2.6. R_e represents the resistance of the extracellular fluids measured at VLF such as 10 kHz; C_m and R_m respectively represents membrane capacitance and intracellular fluid resistance of muscle tissues and describes the β-dispersion[2] in the frequency range 10 $\sim$ 500 kHz; C_b and R_b represents the membrane capacitance and intracellular fluid resistance of red blood cells respectively and describes the β-dispersion in the frequency range 500 kHz $\sim$ 10 Mz; C_t represents the tissue capacitance and is significant in the total impedance for frequencies above 10 MHz. It must be noted that all the values of R and C are nonlinear and depend on frequency and current density ($^{\mathrm{mA}}/_{\mathrm{cm}^2}$).

An intricate aspect in circuit modelling of the human body is considering the dynamic nature of the human body impedance. According to Gordon et al. [44], studies under household voltages at power frequencies have shown that the human body exhibits a high impedance initially as a result of the presence of skin; this impedance rapidly decreases as the skin begins to breakdown. The total impedance of the human body continues to decrease in the next tens of seconds, this may be due to

[2]The ability of a biological cell to filter out low frequency currents and allow high frequency currents to pass through.

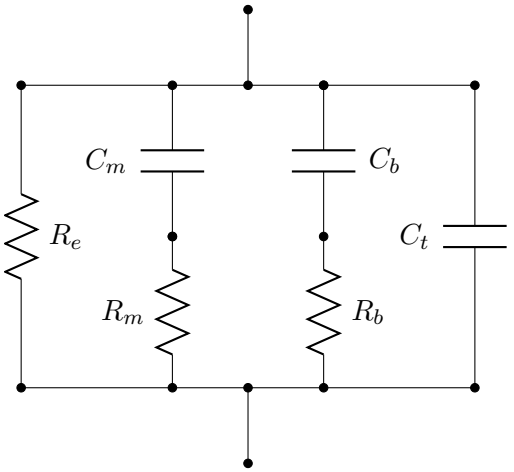

Figure 2.6: Simplified model of the human body under high frequency currents

the thermal runaway[3] process in which internal tissues are broken down by Joule heating. Finally, an increase in impedance can be seen which may be attributed to the dehydration of the tissue at the point of contact with the electrode. Present models of the human body usually comprise of resistive and capacitive properties, however, inductive properties are seldom considered in the model.

Human Circuit Model Considering Lightning

Andrews [2] theorises that the duration of the lightning current which flows internally through the human body is short as external flash-over occurs before internal damage can occur. The majority of the lightning current flows through ionic fluids such as blood and cerebrospinal fluid. Muscle is the tissue with the next lowest impedance. The circuit model proposed by Andrews [2] is shown in Figure 2.7.

Several lightning injury studies are based on the circuit model proposed in Figure 2.7. Misbah et al. [53] used the model to investigate several mechanisms of lightning injuries by calculating the current travelling in each component. Gazzana et al. [54] used the model to simulate lightning transients on grounding systems.

Even though studies exist which uses electrical components to model the human body, these values are based on speculation and minimal measurements. They do not explain the intricate relations of human tissues and the way in which the lightning current flows through the human tissues.

[3] A process in which resistance is lowered due to the increase in internal temperature. This is a result of positive feedback whereby an increase in current flow increases power dissipation which further increases the temperature which further increases the power dissipation [52].

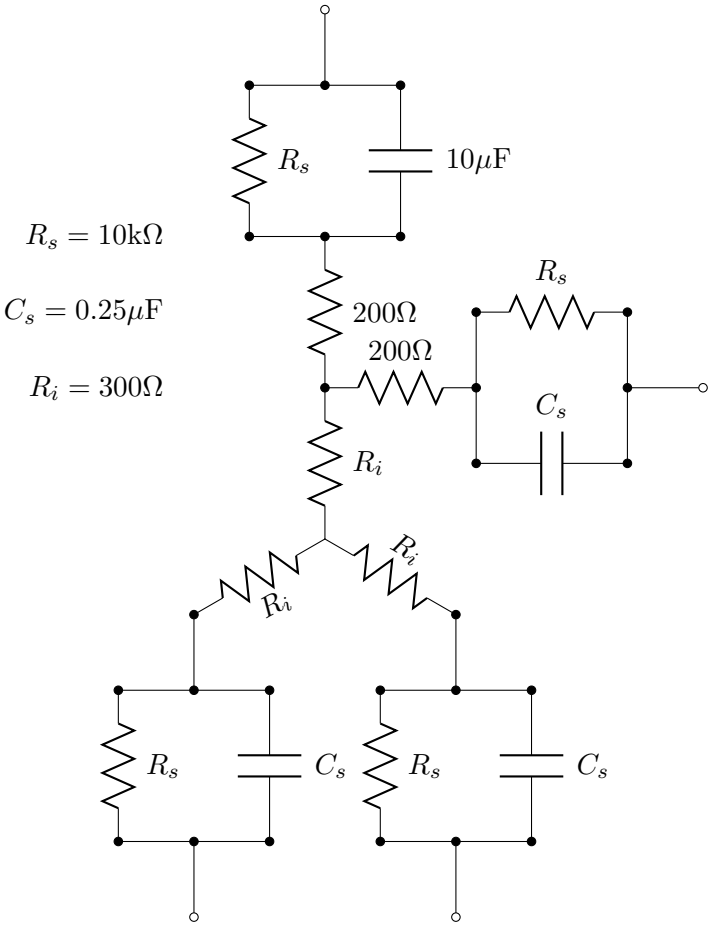

Figure 2.7: Equivalent Circuit Model of the Human Body proposed by Andrews [2]

2.4.2 Electrical properties of Human Tissues

Gordon et al. [44] studied the electrical properties of biological tissues using living hogs by using a 60 Hz AC current of 100 mA. The results show that the nerves and arteries have the highest conductivity whereas muscles, fat and bone have considerably lower conductivity. It is noted from all tested tissues that the phase angles between measured voltages and currents are no more than five degrees which suggests that the overall capacitive effects of the tissues are of minor significance. However, these tests were carried out under a frequency of 60 Hz and are thus insufficient in explaining high frequency effects on human tissues.

The dielectric properties of human tissues are extensively examined and utilised in the study of electromagnetic effects on the human body [55]. In order to understand and investigate the physical phenomena of electromagnetic fields on biological tissues, the dielectric properties of the relevant tissues need to be known. Electromagnetic propagation through any medium is calculated using the dielectric prop-

erties of the medium as defined by Maxwell's Equations [55]. This is significant in quantifying characteristics such as current densities, current pathways and specific absorption rates (SAR) in tissues and organs.

It should be noted that most cylindrically shaped tissues have a higher resistivity in the transverse direction compared to the longitudinal direction [38]. This shows that human tissues are anisotropic[4].

Electrical Properties of Human Cells

The human body in most situations cannot be modelled simply by a single lumped-element impedance since the electromagnetic properties of the human body are non-linear, time-varying, temperature dependant and inhomogeneous [44]. Therefore, it may be significant to examine human body tissues at a cellular level including analysis of cellular interactions and cellular contents.

Human cells are considered to be capacitive due to the dielectric nature of the cell membranes [56]. When a low frequency current flows through a cell, the capacitive reactance of the cell membrane is high. This causes the bulk of the current to flow in the extracellular fluids. When the current is at a high frequency, the impedance of the cell membrane is much less and the current thus flows through the intracellular fluid in addition to the fluid surrounding the cell [38].

According to Talaat [57], as current flows through the tissue, depending on the duration, it results in Joule heating which subsequently alters the resistivity of the tissue. The impedance of the tissue is also affected by the exposure to high electric fields which results in the breakdown of cellular membranes. The breakdown of cellular membranes involves two mechanisms: dielectric breakdown and electroporation.

2.4.3 Voxel Model of the Human Body

The advances in computing power has allowed accurate numerical simulations to be a viable option in analysing and visualising realistic and complex structures. MRI can be used to obtain physical structures of human organs in which accurate and realistic models can be constructed [58]. However, despite the image processing techniques which can be used to differentiate tissue types, medical staff are still required to identify anatomical structures on the scan and rectify the identification process [58].

[4]The material property differs at different locations of the tissue.

Numerical Dosimetry

Numerical dosimetry is the calculation of the energy absorbed by human and animal models from electromagnetic radiation through solving Maxwell's Equations by numerical means such as Finite Element Analysis (FEA) [59]. Earlier works include planar [60], spherical [61] and cylindrical human models [59]. With the advancement in medical imaging, numerical dosimetry has been extended to the use of accurate human models obtained from MRI and X-ray computed tomography [58, 62–64].

The energy absorbed by the human tissues are measured in terms of Specific Absorption Rate (SAR) as shown in Equation (2.3), where σ and ρ are the conductivity and density of the tissue respectively [65].

$$\text{SAR} = \sigma E^2/\rho \tag{2.3}$$

According to Gandhi and Chen [66], two popular numerical methods are used in numerical dosimetry at power-frequencies: Finite Difference Time Domain (FDTD) and Impedance Method (IM). FDTD solves the coupled differential form of Maxwell's Equations for every point in the model in the time domain, assuming ϵ_r and σ_e remains constant. IM presents the model as a network of impedances which are calculated from the complex conductivities $\sigma + jw\epsilon$.

Cylindrical Human Model

When using the FEA approach, cylindrical models are commonly selected to model the human body as it is the simplest to mathematically calculate using numerical methods [59].

Ruan et al. [67] analysed the electrical properties of human tissues and organs by using a cylindrical model of the human body. Werner and Webb [68] used a six-cylinder model of the human body in the study of human thermoregulation. Muramatsu et al. [69] calculated the impedance of the human arm in human body communication by developing a multilayered cylindrical model of the human arm. Ho et al. [70] presented a triple-layered dielectric cylindrical model of the human limb composed of fat, muscle and bone. The human limb model is exposed to a direct contact aperture source and microwave heating effects are examined.

Human Body Voxel Model Considering Lightning Strikes

Gao et al. [71] used a voxel model of the human body to simulate the effects of the lightning step voltage on the human body. The results show that the largest current density appears in the leg muscles and bladder. Current density is much weaker in bones and bone marrow.

Poljak et al. [72] modelled the vertically standing human body as a cylinder with uniform cross section and conductivity. The current density induced in the human body due to electric field coupling of a lightning rod struck by lightning is investigated.

Summary

The DEF model can be integrated by analytical means while the more accurate Heidler function cannot. There are five classical mechanisms of lightning injuries, all of which are characterised by the current magnitude, duration and pathway. The clinical symptoms of lightning injuries can be classified into three main categories: neurological, cardiovascular and external burns. A comparison of HV injuries and lightning injuries yield similar injury mechanisms, however, the fundamental difference is the current duration. The human body is usually modelled using electric circuit theory, but when frequency components are considered, using electric circuit components may not be applicable. Present computing power allows the use of FEA and numerical dosimetry which solves Maxwell's Equations in a simulated environment. This type of simulation has been widely adopted and applied to human body modelling in various fields.

Chapter 3

Methodology

Overview

This chapter describes the rationale and research objectives of this work. An overview of the design and approaches taken to simulate the effects of the FSS frequency components on the current pathway through human tissues is given.

3.1 Problem Statement

Previous studies on lightning injuries using circuit models of the human body are based on time domain analysis and assume human tissue properties to be uniform. The FSS of the lightning flash is a current impulse with multiple frequency components associated with it. Impedances of human tissues are frequency dependant and should not be treated as constants in the analysis of the FSS current through the human body. Simply modelling the human body as a resistor may not be adequate in evaluating phenomena resulting from these frequency components.

The five classic mechanisms of lightning injuries are results from current pathway, current magnitude and current duration. The current pathway through the body is determined by the impedances of various tissues. Current magnitude and current duration are dependant on the FSS itself. Human tissue impedances derived from dielectric properties are frequency dependent and time domain analysis (such as FDTD) is not viable. Frequency domain analysis is required as multiple frequencies need to be examined.

This work provides an initial step in the analysis of the effects of the frequency components of the FSS on the human body using FEA. A human body model is required which accounts for these frequency components. This model needs to provide a more thorough representation of the human body than simple electrical components. To understand the FSS current pathway through the human body, the FSS current pathway through human tissues must be first investigated. A human body model can then be constructed from the cascade of various human tissue models.

3.2 Research Objectives

The scope of this work consists of three main aspects:

- Investigate the frequency components of the FSS.
- Develop human tissue models which take into account the frequency components of the FSS.
- Investigate the effects that the frequency components of the FSS have on the current pathway through human tissues.

A model of the FSS is needed to investigate and define the frequency components of the FSS. The frequency components must be accurately extracted from the model.

Human tissue models are required to describe the effects of the frequency components of the FSS on the current pathway through human tissues. The dielectric properties of human tissues are frequency dependant [55], therefore the electrical properties of human tissues vary depending on the frequency components of the FSS.

Cylindrical models are commonly used in human modelling (Section 2.4.3) and selected as the basis of the human tissue models. The FSS model is directly attached to the human tissue models which present the models as three-dimensional near-field problems. FEA is used as the solution to the human tissue models by solving Maxwell's Equations for the electromagnetic fields and related effects.

Aspects that need to be considered include tissue impedances, current densities and power dissipation. Tissue impedances and current densities determine the current pathway through human tissues, while power dissipation accounts for heating effects. This work considers the current pathway of the FSS through human tissues and is applicable in the analysis of all five classical lightning injury mechanisms.

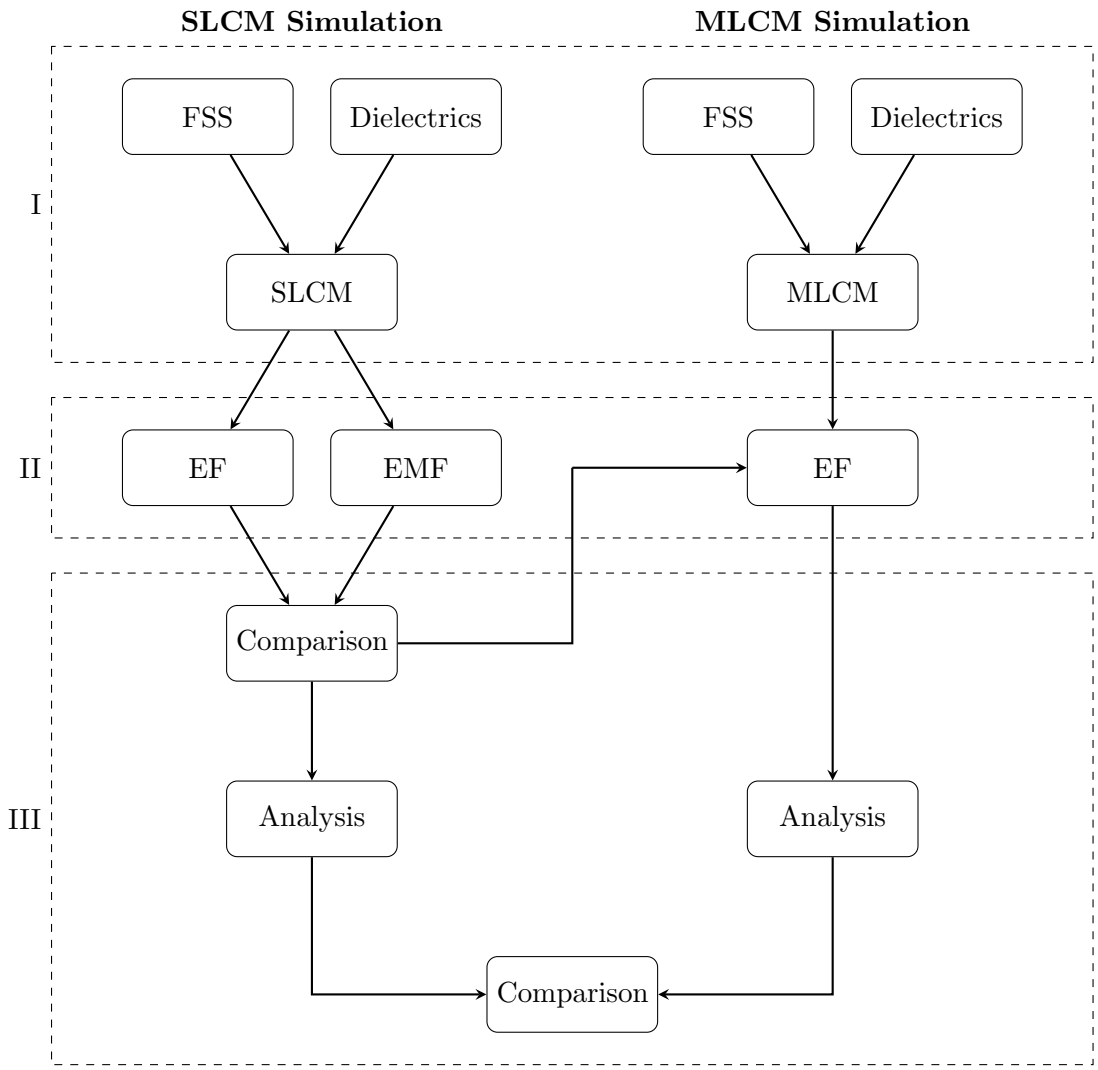

Figure 3.1: Overview of model simulation

3.3 Simulation Overview

This work investigates the effects of the FSS frequency components on the current pathway through the human body. This is carried out by simulations of human tissue cylindrical models using FEA. Two types of cylindrical models are simulated: Single Layer Cylindrical Model (SLCM) and Multi-layered Cylindrical Model (MLCM). An overview of the simulation of the models is depicted in Figure 3.1.

Each model type consists of three phases as shown in Figure 3.1. Phase I **defines and constructs** the human tissue models and applies the dielectric properties and the FSS model to the tissue models. Phase II **investigates** two simulation approaches for the simulation environment: EF and EMF. EF considers only electric fields while EMF considers both electric and magnetic fields as will be discussed in

more detail. Both simulation approaches are undertaken for the SLCM. Based on the results of the SLCM, the more applicable simulation approach is then implemented on the MLCM model. Phase III **analyses and compares** the results obtained from the EF and EMF simulation approaches as well as the SLCM and MLCM simulations. The results are correlated with lightning injury mechanisms.

3.4 Phase I: Models

Two types of models are used to represent human tissues: SLCM and MLCM. SLCM is the modelling of tissues individually without the presence of other tissues. This determines the impedances of individual tissues on a per unit volume basis such that the current pathway can be predicted. MLCM is the modelling of tissues in the presence of adjacent tissues. This determines the effects of tissue interfaces on the current pathway. In this work, the human leg is selected as an application of the MLCM.

FSS The FSS is modelled and the frequency components extracted. These frequency components are individually used as sinusoidal current sources to determine the tissue impedances at respective frequencies.

Dielectrics In order to solve for impedances using FEA, the dielectric properties of the tissues are required. This allows the models to be defined from the electrical perspective. These properties are obtained from Andreuccetti et al. [73] which are further conditioned and analysed.

SLCM 54 human tissues are modelled individually without the presence of other tissues. The FSS model is passed through each SLCM to determine the impedances of the tissue models. The obtained tissue impedances are compared in order to analyse the current pathway through the human body.

To compare the impedances between various tissues, the dimensions of the cylindrical models need to remain constant such that the comparison can be carried out on a per unit volume basis. Each SLCM has a diameter of 10.5 cm and a height of 10.5 cm as shown in Figure 3.2.

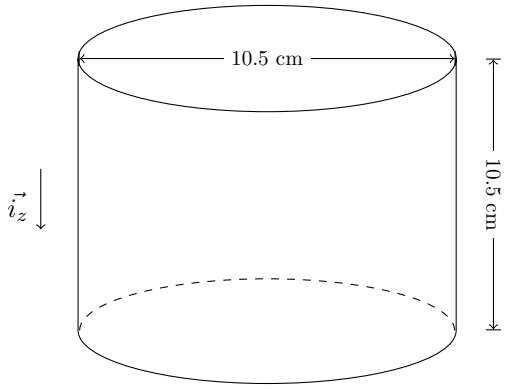

Figure 3.2: Schematic of the SLCM

MLCM The human right leg is modelled as the MLCM. The MLCM is a cylindrical model consisting of multiple tissue layers constructed to examine the effects of tissue interfaces on the current pathway. The human leg is chosen since current must travel through the leg as it is the direct connection between ground and the upright human body.

The tissue layers of the MLCM include bone marrow, cortical bone, muscle, blood and fat. The volume of these tissues are estimated from the human right leg model obtained from BodyParts3D [74] and the Visible Human Project ® [75]. The height of the cylinder is selected to be the same as the height of the human right leg model: 89 cm and the thickness of each tissue layer is calculated from the respective tissue volume. Figure 3.3 shows the schematic of the MLCM.

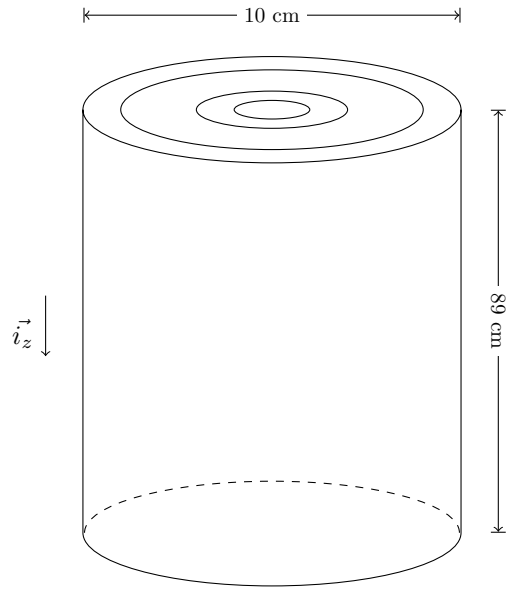

Figure 3.3: Schematic of the MLCM

3.5 Phase II: Physics

Currents at various frequencies which represent the FSS are injected into the cylindrical models to calculate the impedances. The impedances are obtained by means of FEA with the use of Maxwell's Equations. Once the impedances are calculated, the current pathway at various frequencies can be determined as current takes the path of least impedance. Two simulation approaches are taken to calculate Maxwell's Equations: EF and EMF.

EF is the simulation approach which assumes that magnetic fields and related effects are negligible in human tissues and only solves for the electric fields. EMF is the simulation approach which considers both the electric and magnetic fields and any induced effects.

The top ends of the SLCM and MLCM are connected to sinusoidal current sources and the bottom ends are connected to ground terminals. The sinusoidal current source is simulated to only supply current in the $\vec{i_z}$ direction (vertically downwards) as shown in Figures 3.2 and 3.3.

The results from the two simulation approaches are compared to determine which approach is feasible in the analysis of the current pathway through human tissues. From the impedances and current densities, the resistive power dissipation is calculated.

3.6 Phase III: Results and Analyses

The EF and EMF simulation results of the SLCM are compared. These results include current densities, tissue impedances and power dissipation. From the comparison and error analysis, the most accurate and least time consuming simulation approach is then applied to the MLCM.

The SLCM simulation results are adapted to the dimensions of the MLCM such that the SLCM results can be used to predict the MLCM results. Tissue impedances obtained from the SLCM and MLCM are compared with documented lightning injuries and the correlations discussed.

Summary

The effects of the FSS frequency components on the current pathway through human tissues are investigated. Human tissue properties are frequency dependant and the FSS has several frequency components associated with it. Time domain analysis is not applicable in this work due to its limitations and frequency domain analysis is required.

Two human tissue models are simulated using FEA: SLCM and MLCM. To solve for Maxwell's Equations in FEA, two simulation approaches are proposed: EF and EMF. The two simulation approaches are conducted on the SLCM and compared, the more applicable simulation approach is carried out on the MLCM.

The simulation results consist of current densities, tissue impedances and resistive power dissipation. The tissue impedances from the SLCM are used to predict the current pathway of the FSS through the human body. The tissue impedances between the SLCM and MLCM are compared and correlations investigated to examine whether the results from the SLCM can be used to predict the MLCM results.

Chapter 4

Simulation Design

Overview

This chapter describes the design of the simulation environment, which is separated into a series of phases and adopts a modular approach. This research consists of three phases, with the first two phases detailed in this chapter and the third phase detailed in Chapter 5.

Phase I is the *Models* phase which describes the three models used in this work: FSS model, SLCM and MLCM. Section 4.1 details the model chosen for the FSS and the frequency components obtained from it. Section 4.2 details the human tissue dielectric properties which are crucial in defining the material electrical properties of the SLCM and MLCM. Section 4.3 and 4.4 describe the structures and the designs of the SLCM and the MLCM respectively.

Phase II is the *Physics* phase which describes the FEA simulation approaches used in this work: EF and EMF. The simulation approaches are based on Maxwell's Equations and Section 4.5 details the differential equations required for the simulation environment of each simulation approach.

4.1 FSS Model

The DEF is used to model the FSS. This model is selected instead of the more accurate Heidler function as the frequency components of the DEF can be obtained by analytical means as detailed in Section 2.1.

Table 4.1: Parameters of the DEF for various FSS waveforms at 4 kA

Parameter	1.8/30 μs	8/20 μs	10/350 μs
I	4600	12000	4280
α	30060	50000	2171
β	889600	125000	180000

The DEF is decomposed into its basis functions through the use of the Fourier transform. These basis functions characterise the frequency components of the DEF. The magnitudes of the frequency components represent the sinusoidal peak current amplitudes at those specific frequencies. Sinusoidal waveforms at various frequencies can then be used as individual current sources for the analysis of the impedances of human tissues.

The DEF used is chosen to have the waveform: 4 kA, 1.8/30 μs as this FSS waveform is the most common waveform and has a 95% probability of occurrence in nature [1].

The DEF which satisfies 4 kA, 1.8/30 μs is shown in Equation 4.1. The parameters of various standard waveforms are given in Table 4.1. The DEF for the 4 kA, 1.8/30 μs waveform from Table 4.1 is obtained heuristically and plotted in Figure 4.1.

$$\begin{aligned} i(t) &= I(e^{-\alpha t} - e^{-\beta t}) \\ i(t) &= 4600(e^{-30060t} - e^{-889600t}) \end{aligned} \tag{4.1}$$

4.1.1 Frequency Components

The frequency components of the DEF can be obtained with the use of the Fourier Transform as shown in Equation (4.2). Expanding Equation (4.2) and separating the equation into its real and imaginary components yields Equation (4.3) where w is the angular frequency.

$$\begin{aligned} i(t) &= I(e^{-\alpha t} - e^{-\beta t}) \\ i(jw) &= I(\frac{1}{\alpha + jw} - \frac{1}{\beta + jw}) \end{aligned} \tag{4.2}$$

$$i(jw) = I(\frac{\alpha}{\alpha^2 + w^2} - \frac{\beta}{\beta^2 + w^2} + j(\frac{-w}{\alpha^2 + w^2} + \frac{w}{\beta^2 + w^2})) \tag{4.3}$$

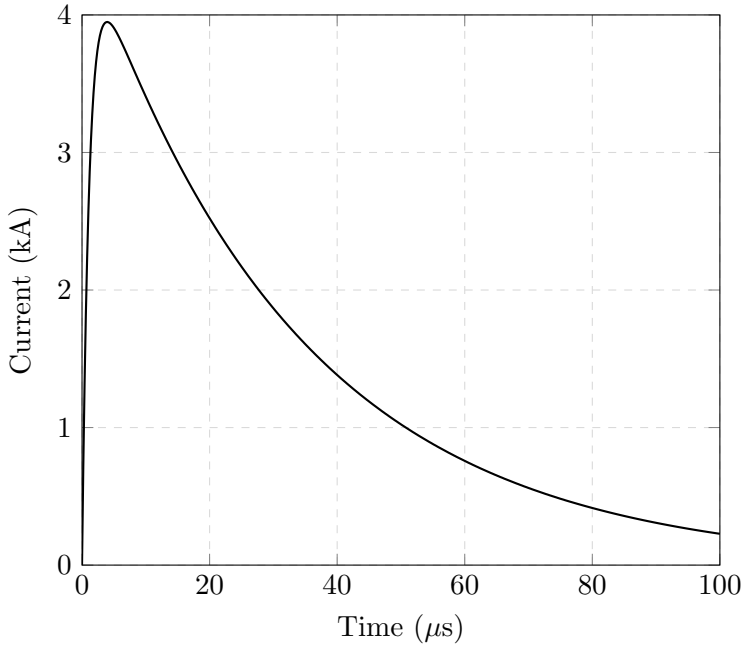

Figure 4.1: DEF 4 kA, 1.8/30 μs

The magnitude and phase of the current waveform at each frequency can thus be calculated using Equation (4.4) and plotted in Fig 4.2 as a bode plot.

$$\begin{aligned} |i(jw)| &= I\sqrt{\mathrm{Re}(i(j\omega))^2 + \mathrm{Im}(i(j\omega))^2} \\ &= I\sqrt{\frac{(\alpha-\beta)^2}{(\alpha^2+w^2)(\beta^2+w^2)}} \\ \theta_{i(jw)} &= tan^{-1}(\frac{Im(i(jw))}{Re(i(jw))}) \end{aligned} \tag{4.4}$$

From Figure 4.2, the -3 dB point is at 2.7 kHz which indicates that frequency components below this frequency constitute half of the total energy of the DEF. The DEF model has a frequency range below 100 kHz before attenuating approximately to -104 dB. This shows that most of the energy of the FSS current is distributed across frequency components below 100 kHz. This concurs with the findings of Wei et al. [17] that the DEF model has a frequency distribution in the range less than 100 kHz. This bandwidth is considered to be in the VLF range.

Chatterjee et al. [50] found that the threshold for human perception of current in the frequency range of 10 Hz $\sim$ 100 kHz varies nearly linearly and then saturates to a constant value for higher frequencies. From Figure 4 and 6 in [50], this constant value is approximately 50 mA. An attenuation of -104 dB for a maximum magnitude of

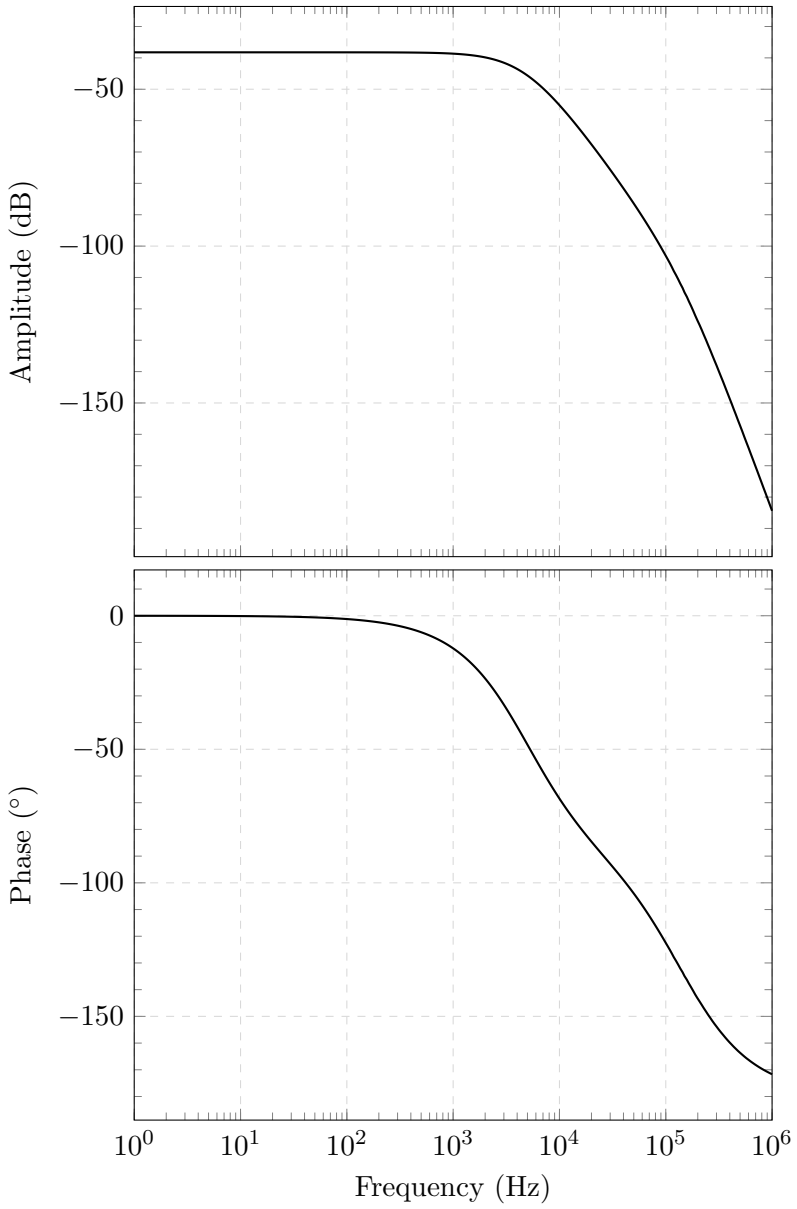

Figure 4.2: Bode plot of the DEF

4 kA yields a current of 5 mA calculated using Equation (4.5). A current of 5 mA at 100 kHz is well below the human current perception threshold, therefore only the frequency range 10 Hz $\sim$ 100 kHz is investigated in this work.

$$\text{Gain[dB]} = 10\log(I^2) \tag{4.5}$$

4.1.2 Normalised FSS

The DEF describes a model of the FSS which is derived from measurements of lightning strokes in nature. The FSS current may not have the same magnitude or waveform as the measurements when attached to the human body. Rakov and Uman [13] assume that the human body resistance is 700 Ω, which attenuates the short stroke current to a mere 4 A in the case of a direct strike due to the occurrence of the external flash over. For the purpose of this research, the validity of modelling the human body to be purely resistive is investigated as frequency components are involved. If the human body is not purely resistive, existing reactance may have a filtering effect on the waveform of the lightning short stroke. Therefore, not all the frequency components of the FSS traverse the human body.

Since the frequency components which pass through the human body are unknown and may have been attenuated, the DEF waveform is used in its entirety to account for the full frequency range. The proposed human tissue models account for the attenuation of current at different frequencies by calculating the impedances at these frequencies.

The magnitude of the FSS current traversing the human body is unknown and can only be estimated [5]. For simplicity, the DEF is normalised to have a peak current of 1 A while maintaining its waveform. This way, the calculated currents traversing the tissues are proportional to the actual current travelling through the body. This is valid assuming that tissue breakdown does not occur and tissue impedance is independent of current magnitude.

The frequency components of the normalised DEF are selected to be in the range up to 100 kHz. A scaling factor η is then added to Equation (4.4) to normalise the DEF model as shown in Equation (4.6). Equation (4.1) is normalised using $\eta = 3947.9$ to yield a final normalised FSS model shown in Equation (4.7). This value is obtained heuristically. The normalised DEF of Equation (4.7) is plotted in Figure 4.3.

$$|i(jw)| = \frac{I}{\eta}\sqrt{\frac{(\alpha-\beta)^2}{(\alpha^2+w^2)(\beta^2+w^2)}} \tag{4.6}$$

$$|i(jw)| = \frac{4600}{3947.9}\sqrt{\frac{(30060-889600)^2}{(30060^2+w^2)(889600^2+w^2)}} \tag{4.7}$$

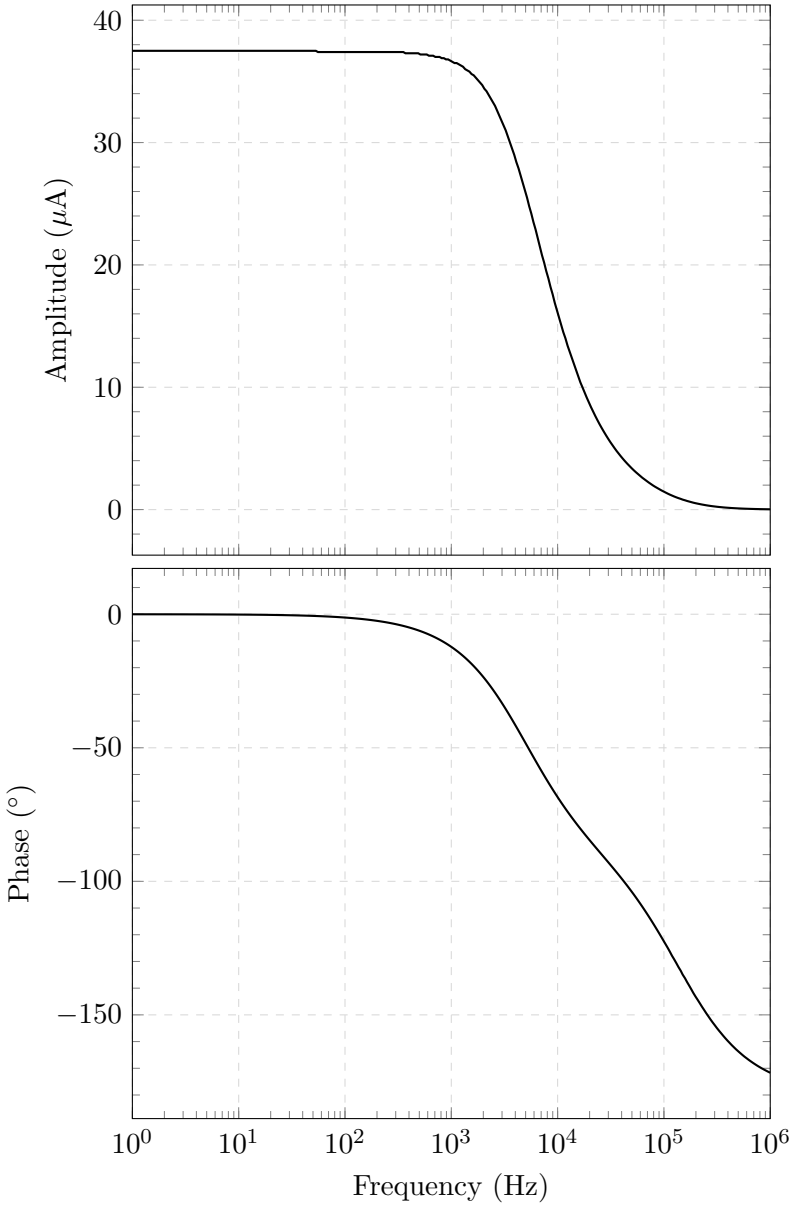

Figure 4.3: Normalised DEF model

4.1.3 Currents

The frequency components obtained from the DEF model are used individually. This is carried out by treating each frequency component as an individual current source. The sinusoidal currents which are passed through the SLCM and the MLCM are in the range of 10 Hz $\sim$ 100 kHz.

The magnitudes of current at various frequencies are obtained from the normalised DEF in Equation (4.7) and shown in Figure 4.3.

The current at various frequencies is injected into the top terminal of the SLCM. A ground plate is defined at the bottom of the SLCM. Equation (4.8) is used as the current boundary feed for the current source.

$$|i(jw)| = \int_{\partial\Omega} \vec{J} \cdot \vec{n} \tag{4.8}$$

The direction of current flow ($\vec{n}$) is in the direction of $\vec{i_z}$ as shown in Figure 4.4 as arrows pointing vertically downwards.

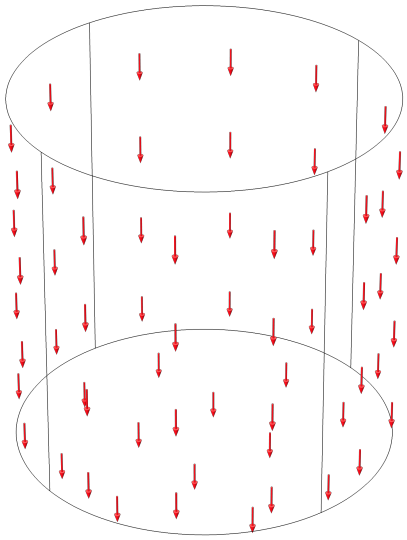

Figure 4.4: Direction of current flow in cylindrical model

4.2 Dielectric Properties

In order to understand and investigate the physical phenomena of electromagnetic fields on biological tissues, the dielectric properties of the relevant tissues need to be known. Electromagnetic propagation through any medium is calculated using the dielectric properties of the medium as defined by Maxwell's Equations [76]. This is significant in quantifying characteristics such as current densities, tissue impedances and power losses in tissues and organs.

The dielectric properties of human tissues are obtained from Andreuccetti et al. [73] who developed an application which calculates the dielectric properties of 54 human tissues in the frequency range from 10 Hz $\sim$ 100 GHz. The data used in this application are based on the parametric models and measured values by Gabriel et al. [55, 77–80]. This data is then processed such that it is usable by COMSOL.

These dielectric properties are frequency dependant and include: effective conductivity (σ_e), relative permittivity (ϵ_r) and loss tangent (δ). The DEF model consists of frequencies up to 100 kHz, therefore, only tissue dielectric properties within this range are examined.

It is possible to electrically define a material in COMSOL by using only the ϵ_r, σ_e and μ_r. Human tissues are assumed to have $\mu_r = 1$. Air is modelled to have $\epsilon_r = 0$ and act as a perfect insulator. This prevents any leakage current from the human tissue models into the surrounding air such that the tissue impedance can be accurately calculated.

4.3 SLCM

In order to predict the current pathway of the FSS through the human body, the path of least impedance must be determined. This is carried out by constructing simulated models that are sufficient to describe the impedances of various tissues.

The SLCM represents a basic single human tissue in the form of a homogeneous and isotropic cylinder. 54 SLCM of human tissues are simulated based on the dielectric properties mentioned in Section 4.2. These are used to define the material properties of the SLCM as required to solve Maxwell's Equations in COMSOL.

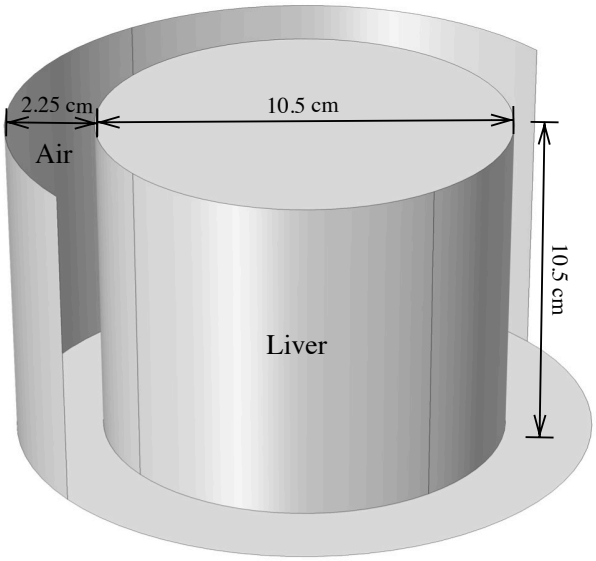

Figure 4.5: Single Layer Cylindrical Model constructed in COMSOL

4.3.1 Structure

It is difficult to estimate the dimensions of specific tissues in the human body, especially when it comes to tissues such as nerves and blood vessels. The tissue dimensions are required in the calculation of the tissue impedance, which in turn is used to evaluate the current pathway by means of impedance comparison. Since the dimensions of tissues in the human body are difficult to determine, tissues are modelled according to a reference volume with known dimensions. This way, the calculated tissue impedances can be compared on a per unit volume basis.

Liver is selected as the reference tissue as it is the largest internal organ in the human body [81]. By modelling all tissues with the same dimensions as liver, the impedance obtained for any specific tissue is the worst case impedance of that tissue at any given point in the human body. This approach may not be valid in a realistic human body, however, this allows for the volumetric impedance comparison of various tissues. From this, the current pathway through the tissues can be predicted.

The mean length of liver is 10.5 cm [81], hence a cylindrical model is used to model the liver with a diameter of 10.5 cm and a height of 10.5 cm. All SLCMs are modelled in this way.

The SLCM is enclosed in air to account for the electromagnetic fields around the cylindrical model. The model assumes that all current flows through the SLCM and no current flows in the surrounding air. The surrounding air has a thickness of 2.25 cm around the SLCM, this value is selected as it is the minimum value required for the accurate calculation of the electric and magnetic fields. The structure constructed in COMSOL is shown in Figure 4.5.

Two terminal plates are attached to the top and bottom faces of the SLCM. The top terminal is modelled as the sinusoidal current source which represent the FSS current entry point. The bottom terminal is modelled as ground, where $V = 0$. The two terminals are defined as perfect conducting boundaries that are directly attached to the model without air gaps.

Boundary Conditions

Boundary conditions are specified as needed by Maxwell's Equations. These are specified at interfaces between materials and geometric boundaries. The details of the boundary conditions defined by COMSOL can be found in the COMSOL manual [76].

The magnetic insulation $\vec{n} \times \vec{A} = 0$ is defined at the outer boundaries of the air gap that encapsulates the cylindrical model as shown in Figure 4.6, where $\vec{n}$ is the normal vector to the surface and $\vec{A}$ is the magnetic vector potential. This allows the consideration of the the magnetic fields in the surrounding air.

The electric insulation $\vec{n} \cdot \vec{J} = 0$ is defined at the outer boundaries of the SLCM, where $\vec{J}$ is the current density. This restricts current flow in the surrounding air and only allows the current to flow in the SLCM.

Mesh size

Points and edges are defined on the SLCM for numerical calculations of Maxwell's Equations. Free tetrahedral meshes are used to mesh the SLCM as shown in Figure 4.7.

The meshes are defined with a maximum element size of 1.5 cm and a minimum element size of 0.27 cm. These element sizes are defined in COMSOL based on the wavelength of the current source, requirements of the physics module and the resolution of the solver. These values are imposed by COMSOL such that the simulation time is minimised without compromising the accuracy of the results.

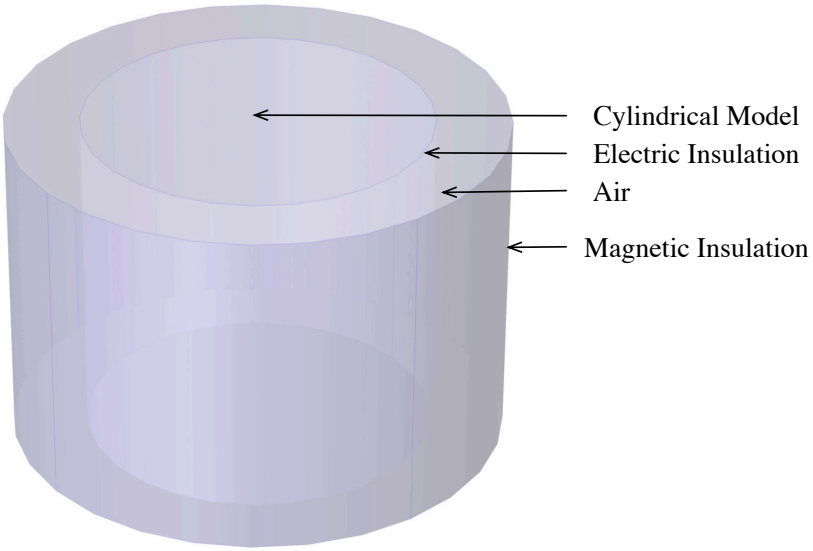

Figure 4.6: Boundaries of the SLCM

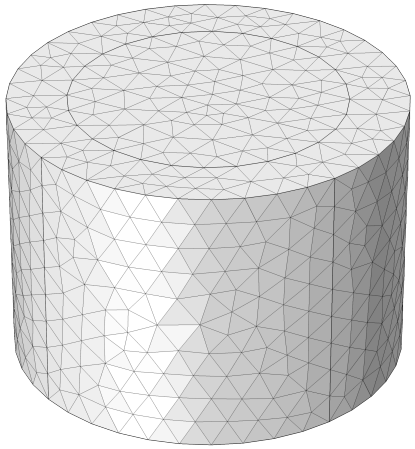

Figure 4.7: SLCM with Tetrahedral Meshes

4.3.2 Simulation

The simulation is carried out in the frequency domain in the range of 10 Hz ∽ 100 kHz. In order to reduce processing time, not all frequencies are simulated. The SLCM is simulated with a resolution of 10 Hz up to 2 kHz and a resolution of 1 kHz thereafter. Higher resolution is chosen for lower frequencies as most of the energy of the DEF is concentrated at these frequencies as detailed in Section 4.1.1. This resolution allows for an accurate analysis on power losses.

Only discrete values can be used in numerical calculations and a continuous frequency spectrum can only be approximated. This introduces errors when evaluations of continuous integrals are needed. These errors need to be considered during the analysis of the results.

54 SLCM simulations are carried out, one for each of the tissue types for which data is available. Each SLCM simulation consists of passing sinusoidal currents at respective frequencies and magnitudes through the SLCM. The top and bottom terminals of the SLCM are respectively connected to a current source terminal and a ground terminal. From each sinusoidal current, a corresponding current density, impedance and power loss is calculated.

4.4 MLCM

The human leg is selected to be the part of the body that is modelled since the leg is the necessary path to ground regardless of the current pathway through the body. The human leg is simplified and modelled to be cylindrically shaped instead of its original geometry as the geometry is extremely complex. This assumption is based on the circular shape of the leg shown in Figure 4.8a and the tubular shape in Figure 4.8b and 4.8c. Additionally, the human leg can also be modelled being composed of tissue layers arranged concentrically about the axis as seen in Figure 4.8a.

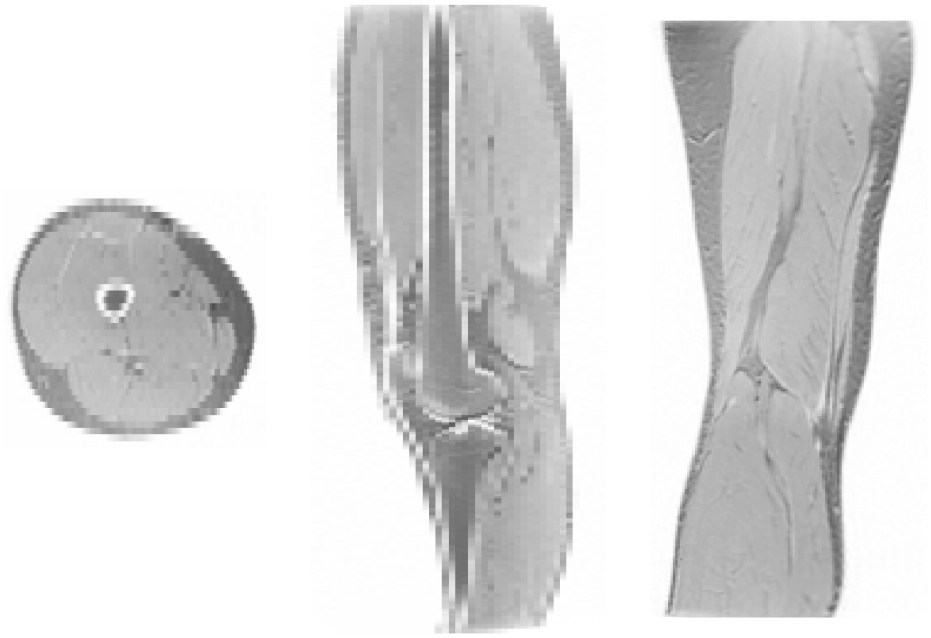

(a) Axial view (b) Sagittal view (c) Coronal view

Figure 4.8: MRI scan of the male human right leg [3]

Table 4.2: Layer thickness of the MLCM

Tissue	Total Volume ($\times 10^6$ mm^3)	Cross-sectional Surface Area (mm^2)	Thickness (mm)
Bone Marrow	0.31	352.38	10.59
Bone	0.7	785.46	8.44
Muscle	3.67	4120.72	21.88
Blood	0.22	245.70	0.94
Fat	2.17	2438.20	8.40

A MLCM is used to model the human leg with five tissue layers: bone marrow, cortical bone, muscle, blood and fat. For simplicity, tissues in the model are distributed uniformly in the form of layers. Tissues are assumed to be isotropic and homogeneous, same as the SLCM. The MLCM is designed under the premise that the FSS current has already entered the human body, hence skin is not modelled as one of the MLCM tissues. This essentially simulates the internal impedance of the human leg.

4.4.1 Structure

The structure of the human leg used in the simulation are obtained and approximated from two sources: Visible Human Project ® [75] and BodyParts3D [74]. Since neither two sources have the complete set of tissues for the human right leg, complementary segments of images from both sources are combined.

The volumes of the bone marrow, muscles and fat are extracted using image segmentation techniques on MRI scans of the male right leg supplied by the Visible Human Project ® [75] using *ITK-snap* [3]. The geometry of the bones and the blood vessels of the leg are acquired directly from BodyParts3D [74] and the volumes are calculated from the volumetric meshes using *MeshLab* [82]. The length of the leg used in the simulation is 89 cm. The tissues are layered along the z-axis as shown in the longitudinal section of the MLCM of Figure 4.9. The thickness of each tissue layer is then calculated from the respective volumes. Table 4.2 shows the tissue thickness used for each layer on the cylindrical model and the diameter of the MLCM is 10.5 cm. The details on the extraction of the tissue volumes can be found in Appendix C.

The MLCM is immersed in air with a thickness of 2 mm, such that the current can only travel in the MLCM. This thickness is selected as the minimum solvable value and electric field effects around the MLCM can be accounted.

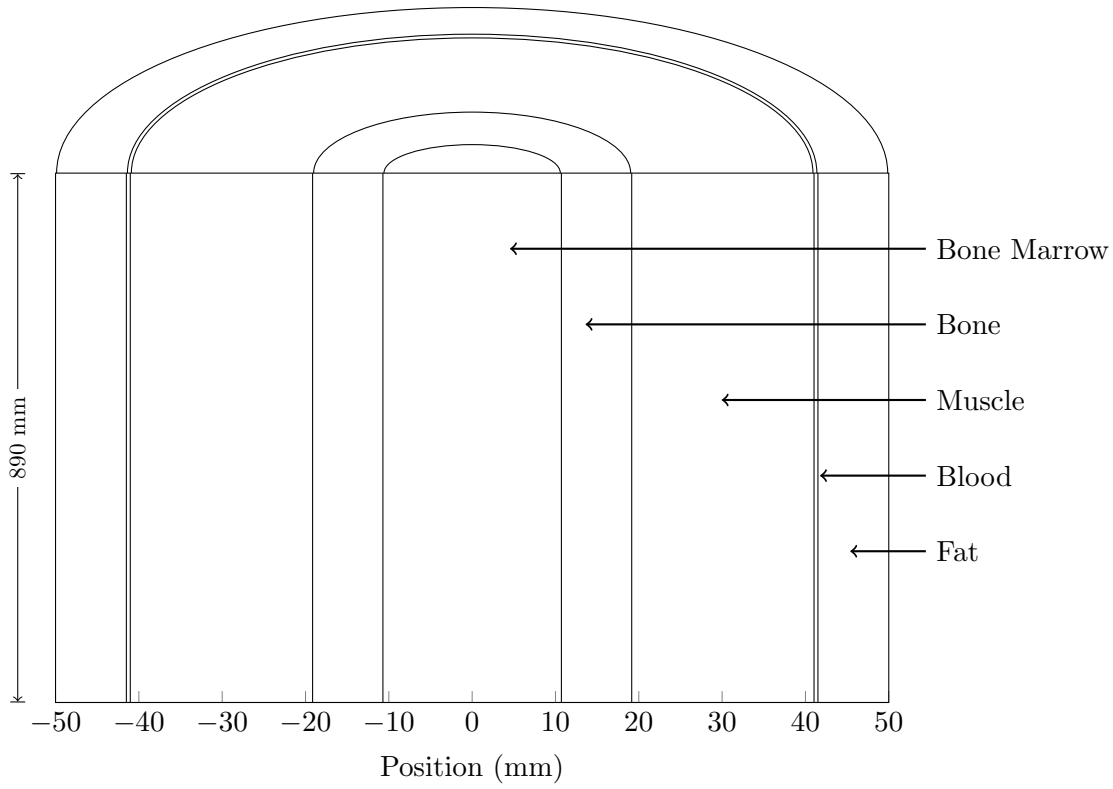

Figure 4.9: Longitudinal section of the MLCM with dimensions

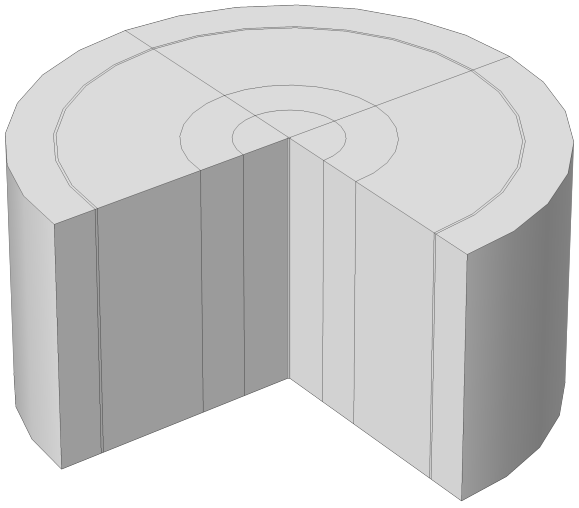

Figure 4.10: MLCM constructed in COMSOL

Figure 4.10 shows the multi-layered cylindrical model constructed in COMSOL using values from Table 4.2. No air gaps exist between the tissue layers and the tissues are in direct contact with one another.

Mesh size

The mesh size used for the SLCM cannot be used for the MLCM. This is due to the thickness of the blood layer in MLCM being thinner than the minimum mesh size used in the SLCM. The MLCM has a maximum element size of 49.5 mm and a minimum element size of 3.6 mm. The air surrounding the MLCM does not need to have a high resolution and has a maximum element size of 135 mm and a minimum element size of 25.2 mm. These element sizes are selected to optimise calculation and processing time by COMSOL.

Boundary Conditions

The material properties of the tissues are defined using the same method as the SLCM in Section 4.2, however, multiple tissues now exist on the same model. The boundaries at the material interfaces are defined by COMSOL [76].

Electric insulation $\vec{n} \cdot \vec{J} = 0$ is defined at the outer boundaries of the outer most layer of the MLCM (fat). Magnetic insulation $\vec{n} \times \vec{A} = 0$ is defined at the outer boundaries of the surrounding air, same as in the SLCM.

4.4.2 Simulation

The simulation time required by the MLCM is much longer than the simulation of the various SLCMs due to the structure size and the meshing element sizes of the MLCM. To reduce processing time, a logarithmic scale of the frequency spectrum is used for the MLCM instead of the frequency increments used for the SLCM as detailed in Section 4.3.2. Due to the limitations of computing power, 100 frequencies, spaced out logarithmically, are simulated for the MLCM.

The current magnitudes at various frequencies are calculated from Equation (4.7) and applied to the MLCM. The top and bottom terminals of the MLCM are connected to the current source terminal and the ground terminal respectively.

The overall MLCM impedance and power loss are investigated along with the impedances, current densities and power losses of individual tissues. From these results the current pathway through the MLCM can be predicted.

4.5 Numerical Methods

The impedances of various human tissues are determined using FEA. This is carried out by modelling the human tissues in a simulated environment in which currents at various frequencies are passed through the tissue models and the impedances at these frequencies are calculated with the use of Maxwell's Equations.

From Section 2.4.1, most standards and studies model the human body using only resistors and capacitances and disregard any magnetically induced effects. In order to verify this, simulations are conducted using two different approaches: EMF and EF. The EMF approach solves both the electric and magnetic fields and considers all magnetically induced effects. The EF approach considers only the electric fields and assumes that the magnetic effects are negligible.

To determine whether antenna and/or transmission line effects (such as reflections, delays and losses) play a role in the model, the electrical length N of the model needs to be determined [76]. Equation (4.9) shows the calculation of the electrical length, where c_0 is the speed of electromagnetic waves ($3 \times 10^8\,\mathrm{m.s^{-1}}$). The electrical length of an object is the ratio between the largest dimension of the object L_c and the wavelength λ of the operating frequency f_o in free space [83]. According to Clark [84], transmission line theory must be applied if $N > 50$. Calculating Equation (4.9) using $f_o = 100\,\mathrm{kHz}$ and the average human height $L_c = 1.8\,\mathrm{m}$ yields $N = 6 \times 10^{-4}$ which is much less than 50. This shows that antenna and transmission line effects can be disregarded for the human body. Since these effects can be disregarded for the human body, it can be disregarded for human tissues (which have smaller dimensions than the human body). The human tissues can therefore be modelled using quasi-static approximation[1].

$$\begin{aligned} \lambda &= \frac{c_0}{f_o} \\ N &= \frac{L_c}{\lambda} \end{aligned} \tag{4.9}$$

Internal damage due to tissue breakdown is rare in lightning injuries (Section 2.2). Since the data for various human tissue breakdown voltages is unavailable and the FSS current magnitude which traverses the human body is unknown, tissue breakdown can be disregarded in the simulations.

[1] Conduction currents are the only sources that need to be considered when evaluating the magnetic fields [85].

Under normal conditions, the electrical breakdown of air occurs when the electric field strength reaches 26.6 kV/cm [7]. The SLCM has a length of 10.5 cm, hence the surrounding air has an electrical breakdown voltage of $V = 26.6 \times 10.5 = 279.3\,\text{kV}$. The normalised DEF has a peak current at 1 A and therefore an impedance of $Z = \frac{V}{I} = 279.3\,\text{k}\Omega$ is needed for breakdown of air to occur across the terminals of the SLCM. The MLCM has a length of 89 cm and an impedance of $Z = 2367\,\text{k}\Omega$ is required for air breakdown to occur. Air breakdown is only considered in SLCM and MLCM when the impedances exceed these values.

The *ACDC* physics in COMSOL is used for the simulation [76]. The governing Maxwell's Equations for the EMF and EF approaches used in the *ACDC* physics is described in the following section.

4.5.1 EMF Approach

The COMSOL physics module selected for the EMF approach is the *ACDC, magnetic fields* module. This module solves for both the electric and magnetic fields and considers induced currents if present [76]. The governing differential equations assuming quasi-static approximation for this module are shown in Equation (4.10) [76].

$$\begin{aligned} \vec{E} &= j\omega\vec{A} \\ \vec{J_{tot}} &= \nabla \times \vec{H} = \vec{J_e} - (j\omega\sigma - \omega^2\epsilon_0\epsilon_r)\vec{A} \end{aligned} \tag{4.10}$$

where:

$\vec{E}$	is the electric field
w	is the angular frequency
$\vec{A}$	is the magnetic vector potential
$\vec{J_{tot}}$	is the total current density in the cylindrical model
$\vec{H}$	is the magnetic field
J_e	is the bound charge current density resulted from the current source terminal

The $(j\omega\sigma - \omega^2\epsilon_0\epsilon_r)\vec{A}$ term in Equation (4.10) accounts for the conduction electric current density and the displacement current density [85]. The derivation of these equations and the use of quasi-static approximation in the models is detailed in Section A.2.

4.5.2 EF Approach

The COMSOL physics module used for this approach is the *ACDC, electric currents* module. This module assumes the magnetic fields and magnetically induced currents are negligible [76]. The governing differential equations solved by this module are shown in Equation (4.11), where V is the scalar voltage potential, $\sigma\vec{E}$ is the conduction electric current density and $j\omega\vec{D}$ is the displacement current density. The magnetic filed H and the magnetic vector potential $\vec{A}$ are not considered. The detailed derivation of these equations can be found in Section A.3.

$$\begin{aligned} \vec{E} &= -\nabla V \\ \vec{J_{tot}} &= \sigma\vec{E} + j\omega\vec{D} + \vec{J_e} \\ \nabla \cdot \vec{J_{tot}} &= 0 \end{aligned} \tag{4.11}$$

4.5.3 Power Dissipation

Only the total resistive power dissipation which results in heat loss is considered as detailed in Section A.4. The total resistive power dissipation of tissues at each frequency is calculated using Equation 4.12, where P_{ef} is the total resistive power dissipation calculated by integrating the total dissipated power density ($\sigma|\vec{E}|^2$) over the volume of the tissue (v). The power dissipation of both the EF and EMF simulation approaches are calculated.

$$\begin{aligned} P_{ef} &= \int_v \vec{J} \cdot \vec{E} dv \\ &= \int_v \sigma\vec{E} \cdot \vec{E} dv \\ &= \int_v \sigma|\vec{E}|^2 dv \end{aligned} \tag{4.12}$$

Summary

The use of DEF to model the FSS waveform of 4 kA, 1.8/30 μs is detailed. The DEF is normalised to 1 A peak and the frequency components of the waveform is extracted to be in the range of 10 Hz $\sim$ 100 kHz. Currents at these frequencies are passed through the SLCM and the MLCM such that the corresponding impedances, current densities and power losses of the tissues can be determined. The structures of the SLCM and MLCM are designed and implemented in COMSOL. 54 SLCMs are constructed with reference to the dimensions of liver with a diameter of 10.5 cm and a height of 10.5 cm. The human leg is modelled using the MLCM with a diameter of 10.5 cm and a height of 89 cm. The MLCM consists of five tissue layers: bone marrow, cortical bone, muscle, blood and fat. Two simulation approaches, EMF and EF, are considered and the differential equations required for the simulations are discussed. The EF simulation approach only considers the electric fields and neglects magnetic field effects while the EMF simulation approach considers both the electric and magnetic field effects.

Chapter 5

Results and Analysis

Overview

This chapter discusses Phase III of the work. This includes results of the SLCM and MLCM simulations detailed in Chapter 4. Both the EF and EMF approaches are used for the SLCM. The results include current densities, complex impedances and resistive power losses of 54 human tissues. The complex impedances obtained from the EF and EMF approaches are analysed and compared. The more applicable approach (EF) is then used in the simulation of the MLCM.

Section 5.1 discusses the results of the 54 SLCMs obtained from the EF and EMF simulation approaches. Current densities, complex impedances and resistive power losses of all tissues obtained from the two simulation approaches are compared.

Section 5.2 discusses the results of the MLCM obtained from the EF simulation approach. Current densities, complex impedances and resistive power losses of the five tissues on the MLCM are detailed.

Section 5.3 compares the results from the SLCM and MLCM with the symptoms of lightning injuries and the results are correlated.

5.1 SLCM Results

The results and analysis for the SLCM is discussed in this section. Two approaches are taken to simulate this model: EF and EMF. Results from both approaches are compared to determine the effects of magnetic fields on the SLCM.

5.1.1 Results of the EF approach

Results obtained from the EF approach include current density, complex impedance and resistive power loss.

Current Density

The tissues used in the SLCM are assumed to be homogeneous, uniform and isotropic, hence the current density is uniform throughout the entire cylindrical model.

The current density J at the current source terminal of the SLCM satisfies Equation (5.1), where $|i(jw)|$ is the current injected at the current source terminal of the SLCM and A is the cross sectional surface area of the SLCM. Since the same currents are injected into all 54 SLCMs, the current densities for all SLCMs are identical. The measured currents are identical to Figure 4.3 for all 54 SLCMs and not listed in this work.

$$J = \frac{|i(jw)|}{A} \tag{5.1}$$

Impedance

The impedance (Z_{ef}) obtained from the EF approach in the frequency range 10 Hz $\sim$ 100 kHz is calculated using Equation (5.2), where R_{ef} and X_{ef} is the resistance and the reactance of the SLCM respectively.

$$\begin{aligned} Z_{ef} &= R_{ef} + \mathrm{j}X_{ef} \\ |Z_{ef}| &= \sqrt{{R_{ef}}^2 + {X_{ef}}^2} \end{aligned} \tag{5.2}$$

To clearly present the results, tissues are classified into five categories based on the standard deviations of Z_{ef} between various frequencies and shown in Figures B.1 - B.5 in Appendix B. Since current flows in a path of least impedance, tissues with the lowest Z_{ef} are carefully examined.

Figure B.1 shows tissues that have $|Z_{ef}|$ with standard deviations less than 2 Ω and presented in Table B.1. Table 5.1 shows the average Z_{ef} for several tissues from Table B.1 which exhibit R_{ef} in the mΩ region.

The tissues presented in Table 5.1 have the lowest $|Z_{ef}|$ out of all 54 tissues. These tissues can be considered to be purely resistive as $R_{ef} \gg X_{ef}$. It should be noted that these tissues are aqueous biological tissues except for Gall Bladder.

Table 5.1: Tissues R_{ef} in the mΩ region

Tissue	Average Z_{ef} (Ω)
Cerebrospinal Fluid	$6.06 - 0.47 \times 10^{-3}\,\mathrm{j}$
Vitreous Humour	$8.08 - 0.75 \times 10^{-3}\,\mathrm{j}$
Gall Bladder Bile	$8.66 - 1.05 \times 10^{-3}\,\mathrm{j}$
Gall Bladder	$13.47 - 2.54 \times 10^{-3}\,\mathrm{j}$

According to Pethig and Kell [56], aqueous tissues contain mobile ions that are able to move freely which result in constant conductivity and permittivity. Andrews [2] suggests that most of the lightning current flow is via aqueous tissues such as cerebrospinal fluid and blood. This concurs with the consistent Z_{ef} for the aqueous tissues presented in Table 5.1. The R_{ef} of blood is not in the mΩ region, therefore not presented in Table 5.1. However, blood has the fifth lowest impedance as seen from Figure B.1.

Gall bladder exhibits the same properties as aqueous tissues which may be attributed to the bile contained within the gall bladder.

From the Z_{ef} results, given the same volume for all 54 tissues, tissues shown in Table 5.1 are the top four tissues that the FSS current is most likely to traverse due to the extremely low $|Z_{ef}|$.

An equivalent circuit model can be developed for each SLCM from the Z_{ef} as shown in Figure 5.1, where C_{ef} is the capacitance of the SLCM and can be calculated using Equation (5.3). This circuit model is frequency dependent and R_{ef} and C_{ef} differs depending on the frequency of the current source.

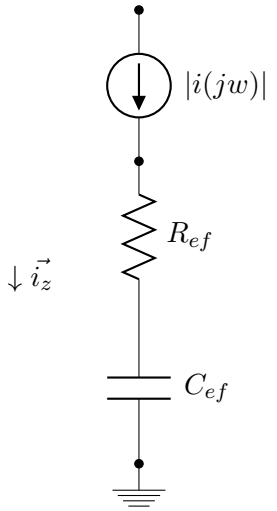

Figure 5.1: Equivalent Circuit Model of the SLCM

$$C_{ef} = \frac{1}{j\omega X_{ef}} \tag{5.3}$$

Power Dissipation

Only the total resistive power dissipation (P_{ef}) is considered as this term relates to heat dissipation and resistive losses [86]. The calculated P_{ef} of the SLCM is indirectly proportional to Z_{ef} as shown in Figures B.6 $\sim$ B.10. The proportionality arises from the conductivity (σ) of the SLCM as seen in Equation (5.4), where Z_{ef} is dependant on the tissue resistivity ($1/\sigma$).

$$\begin{aligned} P_{ef} &= \int_v \vec{J} \cdot \vec{E} dv \\ &= \int_v \frac{|\vec{J}|^2}{\sigma} \end{aligned} \tag{5.4}$$

5.1.2 Results of the EMF approach

In order to examine the magnetic effects on the SLCM, the magnetic fields are considered along with the electric fields. The computation of the EMF simulation takes significantly longer compared to the EF simulation. It takes on average eight times more simulation time for the same SLCM.

Impedance

The impedance (Z_{emf}) obtained from the EMF approach in the frequency range 10 Hz $\sim$ 100 kHz is shown in Equation (5.5), where R_{emf} and X_{emf} are the resistance and reactance obtained from the EMF approach respectively.

$$\begin{aligned} Z_{emf} &= R_{emf} + \mathrm{j}X_{emf} \\ |Z_{emf}| &= \sqrt{{R_{emf}}^2 + {X_{emf}}^2} \end{aligned} \tag{5.5}$$

Table 5.2: Tissues with $error_X > 0.1$

Tissue	$error_X$
Cerebrospinal Fluid	1.3
Vitreous Humour	1.6
Gall Bladder Bile	2.08
Gall Bladder	8.67

An error analysis is conducted to compare Z_{ef} and Z_{emf} as detailed in Section B.3. The error between the EF and EMF results are calculated as shown in Equation (5.6), where $error_Z$, $error_R$ and $error_X$ is the absolute error of the impedance magnitudes, resistances and reactances respectively.

$$\begin{aligned} error_Z &= |(|Z_{emf}| - |Z_{ef}|)/|Z_{emf}|| \\ error_R &= |(R_{emf} - Ref)/R_{emf}| \\ error_X &= |(X_{emf} - X_{ef}/X_{emf})| \end{aligned} \tag{5.6}$$

From Table B.3.1, most tissues exhibit $error_R \approx 10^{-5}$ and $error_X \approx 10^{-3}$. Since $R_{emf} \gg X_{emf}$ and $R_{ef} \gg X_{ef}$, the overall $error_Z$ for all tissues depend largely on R_{emf} and R_{ef} and results in $error_Z \approx 10^{-5}$.

Table 5.2 shows all tissues with $error_X > 0.1$. The $|Z_{emf}|$ for these tissues are plotted against $|Z_{ef}|$ in Figures 5.2 $\sim$ 5.3. The average Z_{emf} of these tissues are shown in Table 5.3.

Table 5.3: Average Z_{emf} of tissues with $error_X > 0.1$

Tissue	Average Z_{emf} (Ω)
Cerebrospinal Fluid	$6.06 + 1.6 \times 10^{-3}\,\mathrm{j}$
Vitreous Humour	$8.08 + 1.3 \times 10^{-3}\,\mathrm{j}$
Gall Bladder Bile	$8.66 + 1 \times 10^{-3}\,\mathrm{j}$
Gall Bladder	$13.47 - 0.5 \times 10^{-3}\,\mathrm{j}$

Table 5.1 shows tissues which have capacitive reactances ($X_{ef} < 0$) whereas Table 5.3 presents the same tissues (except Gall Bladder) but with inductive reactances ($X_{emf} > 0$). This indicates that these aqueous tissues are susceptible to magnetic field effects within the FSS frequency range. This may be attributed to the aqueous nature of these tissues.

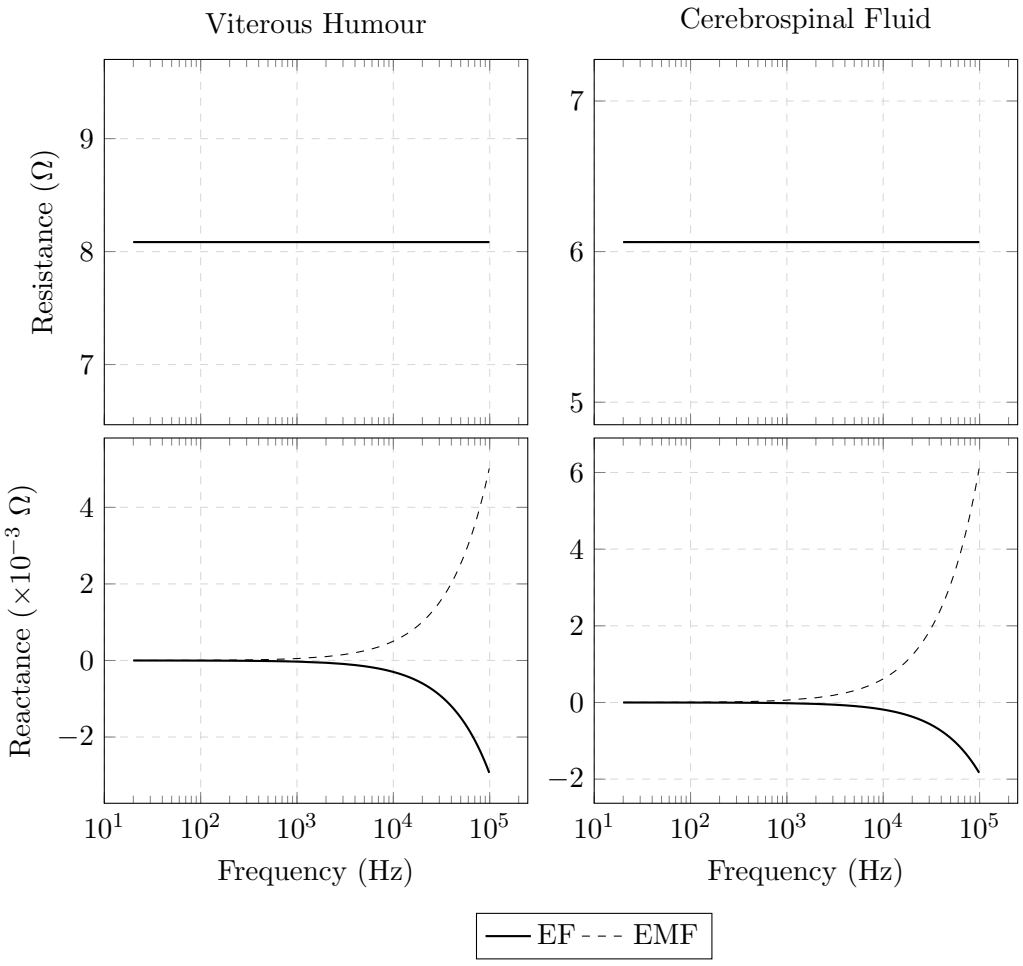

Figure 5.2: EMF and EF tissue impedance comparison for Vitreous Humour and Cerebrospinal Fluid

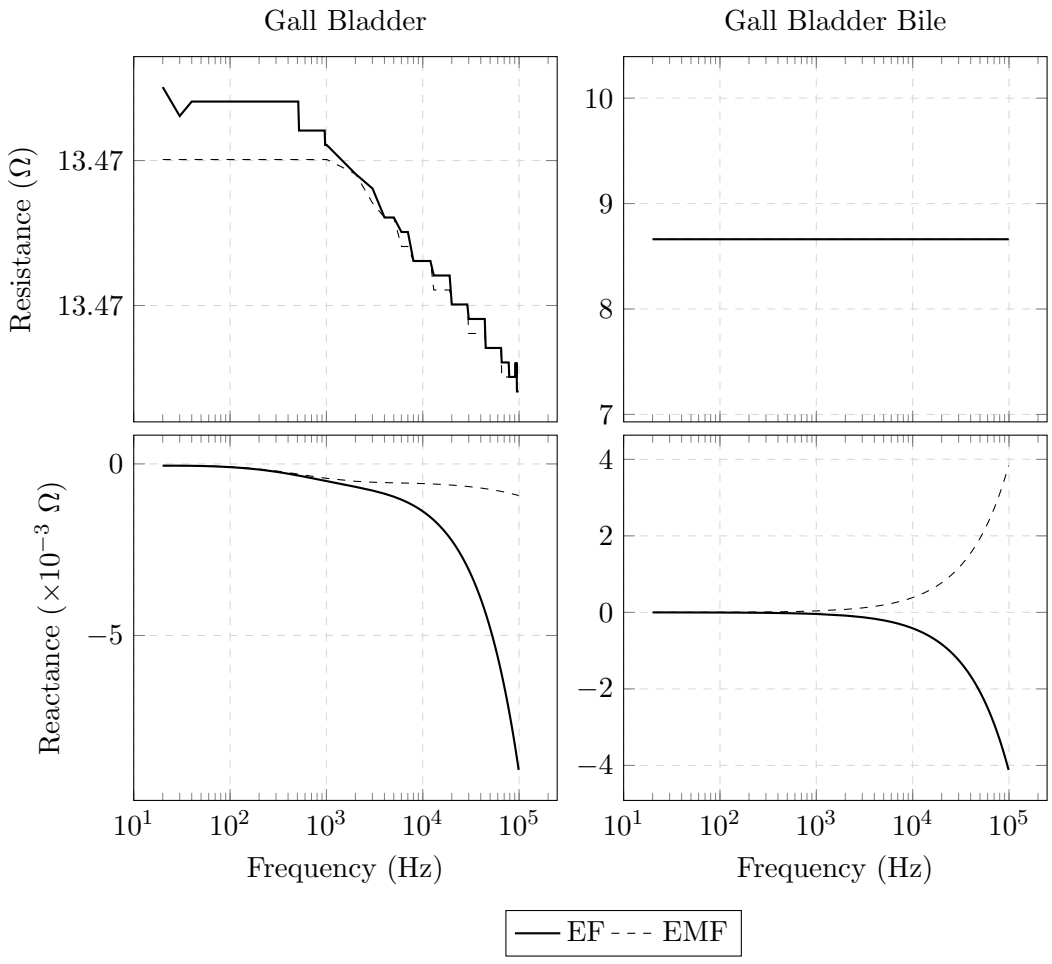

Figure 5.3: EMF and EF tissue impedance comparison for Gall Bladder and Gall Bladder Bile

It should be noted that X_{ef} and X_{emf} are in the $m\,\Omega$s and have insignificant contributions to the overall Z_{ef} and Z_{emf}. From Figures 5.2 $\sim$ 5.3, X_{ef} and X_{emf} only begin to deviate for frequencies above 1 kHz. Most of the energy of the DEF is concentrated at frequencies below 2.7 kHz, therefore the deviations do not contribute significantly to the overall impedance calculation and power losses.

From Table B.3.1, all 54 tissues have $error_X < 10^{-4}$ except tissues in Table 5.2. This shows that the differences between the EF and EMF approaches are negligible. Since the simulation time required by the EMF approach is eight times more than the EF, the EMF approach can be disregarded.

5.2 MLCM Results

The MLCM is simulated using the EF approach since the EMF approach can be disregarded as detailed in Section 5.1.2. The MLCM consists of five tissue layers: bone marrow, cortical bone, muscle, blood and fat. The current density and the power dissipation of each tissue on the MLCM is discussed. The individual tissue impedances are not analysed as the current pathway can be predicted from the tissue current densities. However, the overall impedance of the MLCM is calculated and compared with exiting studies.

5.2.1 Current Density

Compared to the current densities of the SLCM (which are the same for all tissues), the current densities of the MLCM tissues are vastly different due to the different tissue surface areas. The current densities of the MLCM tissues over the DEF frequency range are only dependent on the magnitude of the current source, hence only the 60 Hz frequency component is discussed in this section.

From Equation (4.6), the 60 Hz frequency component of the normalised FSS model has a magnitude of 37 μA. A current source of 37 μA at 60 Hz is connected to the top terminal of the MLCM. The current densities measured along the layers of the MLCM is shown in Figure 5.4. The current density is the highest in blood ($1.71\ \times 10^{-2}\,\mathrm{A/m^2}$) and lower in muscle ($0.76 \times 10^{-2}\,\mathrm{A/m^2}$). The current densities of the other tissues are less than $0.1 \times 10^{-2}\,\mathrm{A/m^2}$.

Using the surface area of each tissue from Table 4.2 with the current density shown in Figure 5.4, the current travelling through each tissue is calculated and shown in Table 5.4. The summation of the tissue currents yields the same current at the current source, indicating that there are no leakage currents and the power losses are minimal.

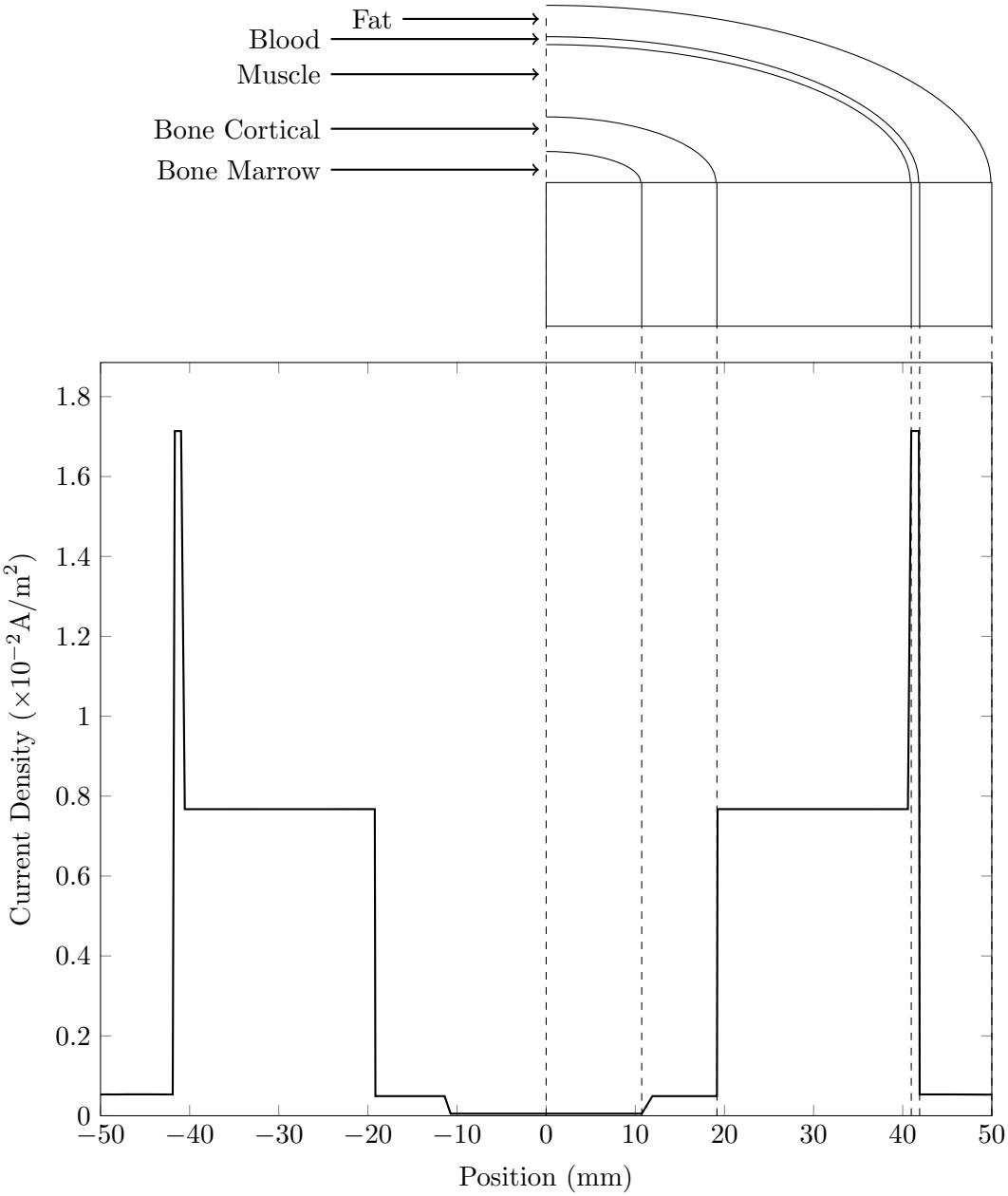

Figure 5.4: Current density of the MLCM measured along the tissue layers at 60 Hz. Values are normalised according to surface area.

Table 5.4: Current traversing the MLCM tissues at 60 Hz

Tissue	Current (μA)
Fat	1.30
Blood	4.21
Muscle	31.63
Cortical Bone	0.39
Bone Marrow	0.019

From Table 5.4, it can be seen that 85% of the current travels through muscle, 11% through blood, 3.5% through fat and the rest through cortical bone and marrow. This current distribution is dependent on the tissue volumes and the tissue impedances. Muscle contributes to 51% of the total volume of the MLCM and has a relatively low impedance compared to other tissues as seen in Figure B.2. Blood, having the lowest impedance out of all MLCM tissues as seen in Figure B.1, only contributes to 3% of the total volume of the MLCM.

The calculated current densities between 10 Hz $\sim$ 100 kHz for the MLCM are all proportional to Figure 5.4, yielding the same results and not presented in this work.

5.2.2 Power Dissipation

The total power dissipated by each tissue (P_{di}) on the MLCM is calculated from the volume integration of the total power dissipation density of the tissue (Q_{di}) and plotted in Figure 5.5. The P_{di} of each tissue is proportional to the current travelling through the tissues in Table 5.4.

The total power dissipated by the MLCM (P_d) is calculated from the summation of the P_{di} for all tissues and represented in Figure 5.6. From the figure, P_d is negligible at frequencies above 10 kHz; this is due to the attenuation of the FSS current at high frequencies.

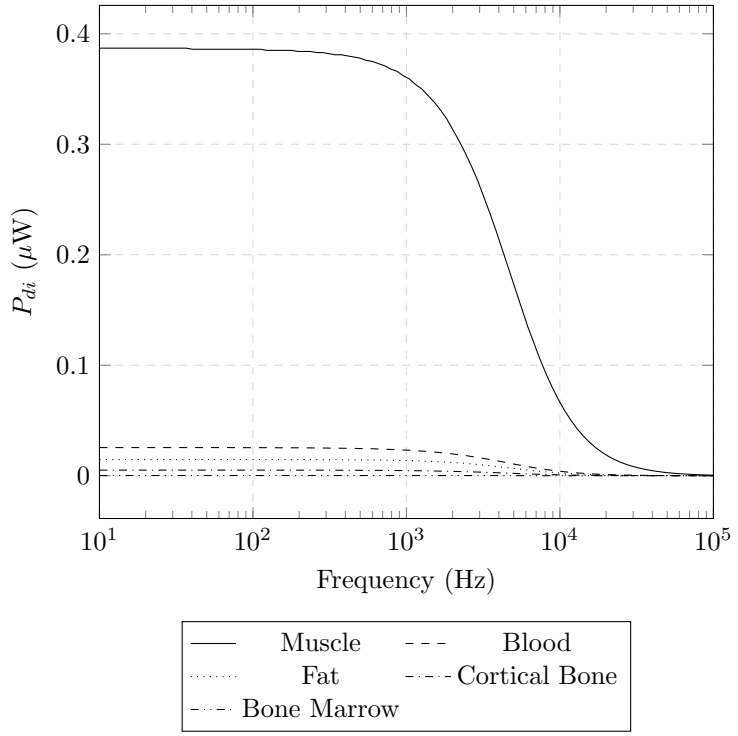

Figure 5.5: P_{di} of tissues on the MLCM

5.2.3 Impedance

The overall impedance Z_{MLCM} of the MLCM is shown by Equation (5.7), where R_{MLCM} is the total resistance of the MLCM and X_{MLCM} is the total reactance of the MLCM.

$$\begin{aligned} Z_{MLCM} &= R_{MLCM} + \mathrm{j}X_{MLCM} \\ |Z_{MLCM}| &= \sqrt{{R_{MLCM}}^2 + {X_{MLCM}}^2} \end{aligned} \tag{5.7}$$

Figure 5.7 shows the simulated impedance of the MLCM in the frequency range $10\,\mathrm{Hz} \sim 100\,\mathrm{kHz}$. From Figure 5.7, $|Z_{MLCM}|$ decreases with increasing frequency and is mainly dependant on R_{MLCM} whereas X_{MLCM} does not significantly contribute to the overall $|Z_{MLCM}|$.

From Figure 5.7, X_{MLCM} exhibits a minimum at 1.2 kHz and a maximum at 8.1 kHz with a distorted wave shape between the two values. This may be due to the cascade of different reactances of various tissues resulting in a filtering effect due to different frequency responses. The tissue interfaces may have capacitive effects due to the different material properties and alter the current magnitude at various frequencies.

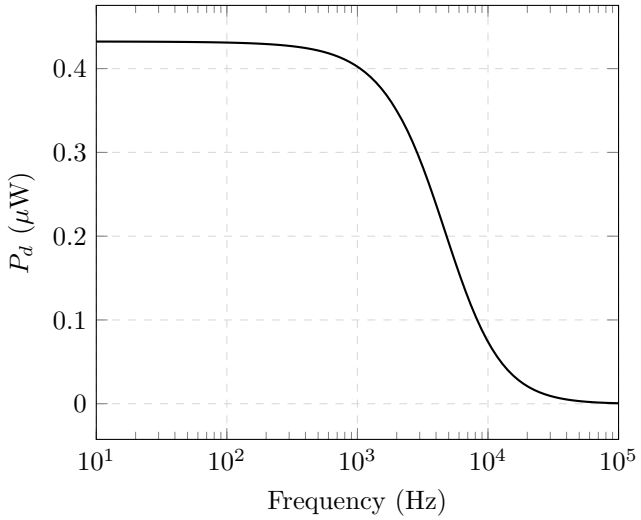

Figure 5.6: P_d of the MLCM

Equivalent Circuit Model

An equivalent circuit model of the MLCM can be constructed from the simulation results as shown in Figure 5.8. Equation (5.8) shows that the total impedance of a single tissue (Z_i) on the MLCM is calculated as a summation of all the tissue impedances at various mesh points of the tissue. $X_{i,k}$ can be calculated using Equation (5.9). Different currents flowing in the MLCM tissues result in voltages induced at the tissue interfaces, these can be modelled as capacitances ($C_{i\sim i+1}$) as shown in Equation (5.10).

$$Z_i = \sum_{k=1}^{n} R_{i,k} + j \sum_{k=1}^{n} X_{i,k} \tag{5.8}$$

$$X_{i,k} = \frac{1}{jwC_{i,k}} \tag{5.9}$$

$$C_{i\sim i+1} = \sum_{k=1}^{n} C_{i\sim i+1,k} \tag{5.10}$$

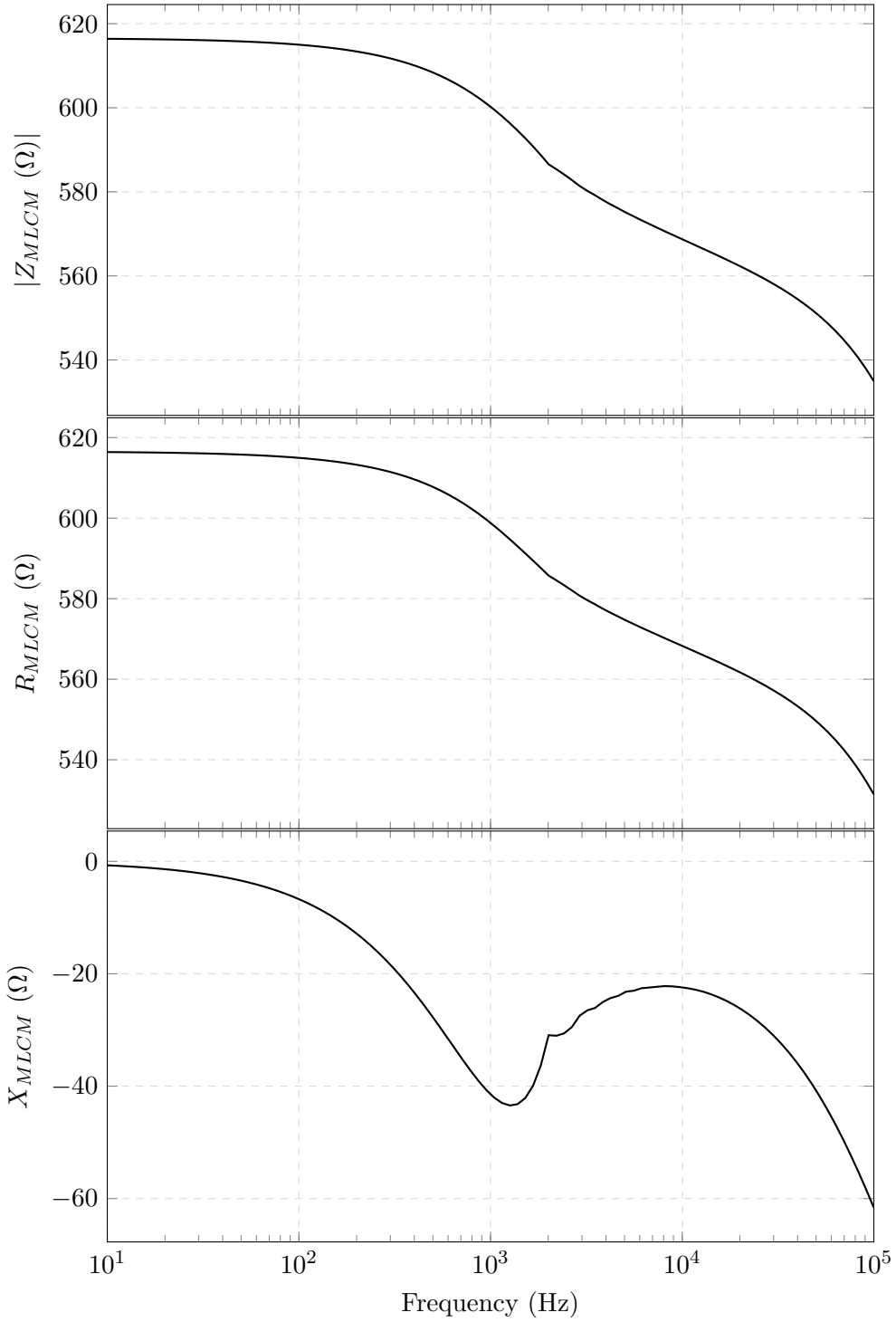

Figure 5.7: Impedance of the MLCM

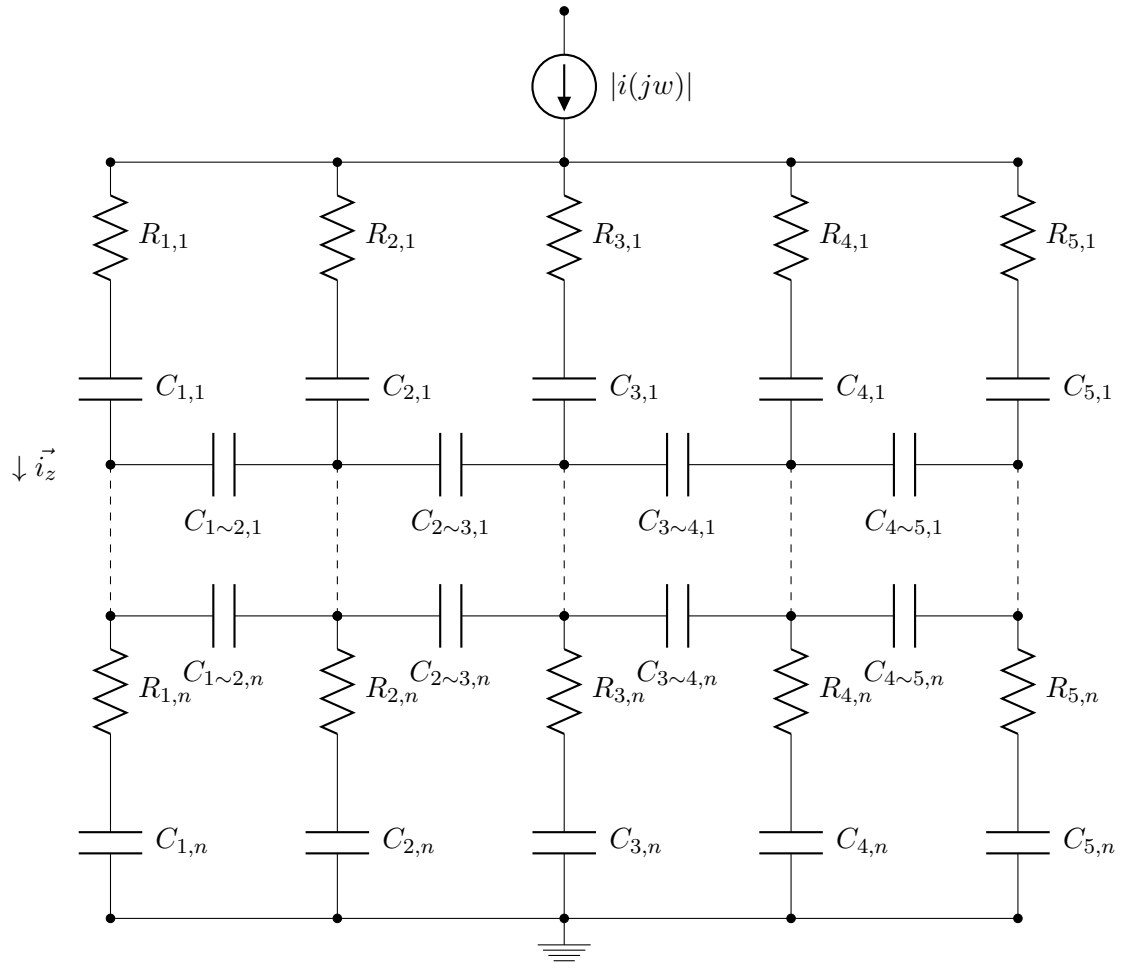

Figure 5.8: Equivalent Circuit model of the MLCM

The MLCM equivalent circuit model shown in Figure 5.8 can be collapsed and simplified into an equivalent circuit model similar to Figure 5.1. A frequency dependant equivalent circuit model of the MLCM shown in Figure 5.9 can be constructed. C_{MLCM} is the overall capacitance of the MLCM calculated using Equation (5.11) where w is the angular frequency.

$$\begin{aligned} X_{MLCM} &= \frac{1}{jw\ C_{MLCM}} \\ C_{MLCM} &= \frac{1}{jw\ X_{MLCM}} \end{aligned} \tag{5.11}$$

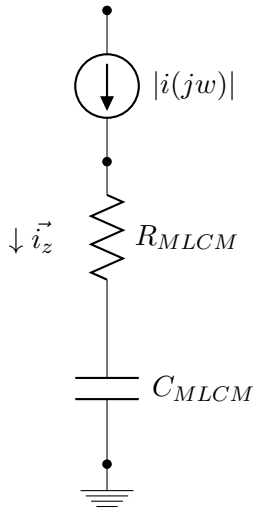

Figure 5.9: Equivalent Circuit Model of the MLCM

5.3 SLCM and MLCM Results Comparison

5.3.1 Impedance

The MLCM tissues impedances cannot be directly compared with the same tissues from the SLCM since the tissue surface areas are different. Z_{ef} of each tissue is normalised by scaling the tissue surface area of each SLCM to the surface area of the corresponding tissue in the MLCM. This normalisation is shown in Equation (5.12),

where SA_{SLCM} is the surface area of the SLCM; SF_i is the scaling factor of the tissue; SA_{MLCM_i} is the surface area of the corresponding tissue on the MLCM; $Norm(Z_{ef})_i$ and $Norm(X_{ef})_i$ is the normalised Z_{ef} and X_{ef} of the tissue respectively.

$$\begin{aligned} SA_{SLCM} &= \pi \times (52.5\,\text{mm})^2 \\ SF_i &= \frac{SA_{SLCM}}{SA_{MLCMi}} \\ Norm(Z_{ef})_i &= SF_i \times Z_{ef_i} \\ Norm(X_{ef})_i &= SF_i \times X_{ef_i} \end{aligned} \tag{5.12}$$

The calculated SF for each tissue of the MLCM is shown in Table 5.5. The $Norm(Z_{ef})$ of the SLCM for the corresponding tissues on the MLCM are shown in Figure 5.10.

Table 5.5: The calculated SF for MLCM tissues

Tissue	SF
Bone Marrow	24.57
Cortical Bone	11.02
Muscle	2.10
Blood	70.48
Fat	3.55

The values of $Norm(Z_{ef})$ in Figure 5.10 are arbitrary and is only used for impedance comparison. From the $Norm(Z_{ef})$ of tissues, it can be seen that the current mostly travels in muscle, blood and fat and less in cortical bone and bone marrow. This concurs with the results obtained from the MLCM as shown in Table 5.4.

From Figure 5.11, it can be seen that the $Norm(X_{ef})$ graphs of cortical bone and fat intersect at approximately 2 kHz. This may be the main attribute to the waveform minimum of the X_{MLCM} as seen in Figure 5.7. Hence, the $Norm(X_{ef})$ of the MLCM tissues can be cascaded to yield X_{MLCM}.

From the above, the current pathway can be predicted from the SLCM without simulating the MLCM. This is valid only if the tissues are cylindrically modelled and the surface areas and volumes of all tissues are known. However, the current densities, tissue impedances and power dissipated cannot be predicted in this way. The SLCM results only serve as an indication as to the tissues that the current is most likely to traverse.

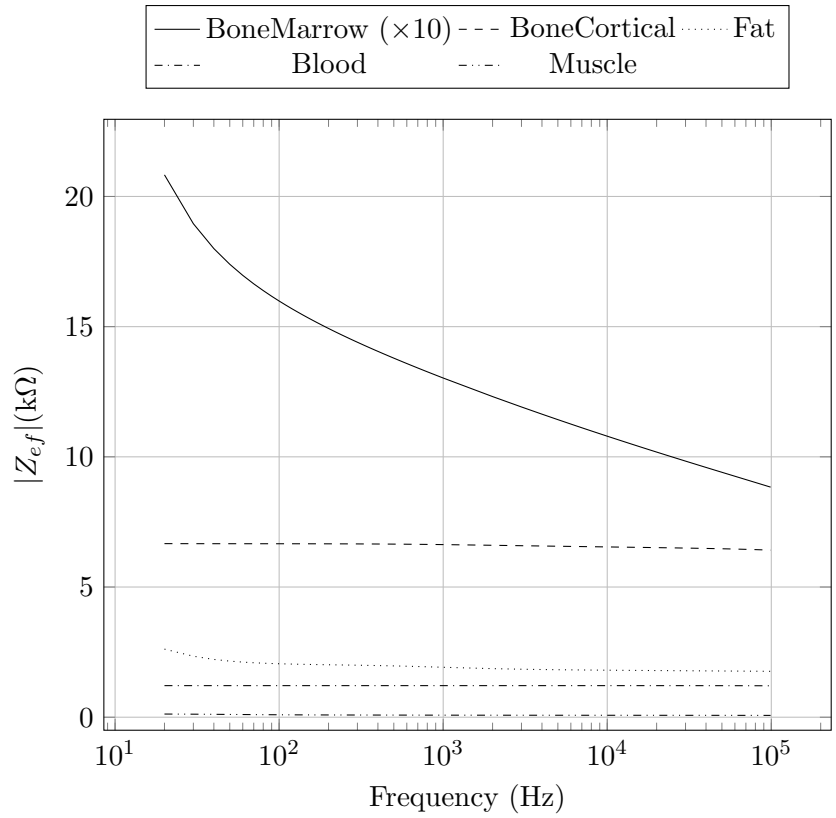

Figure 5.10: $Norm(Z_{ef})$ of SLCM tissues on the MLCM

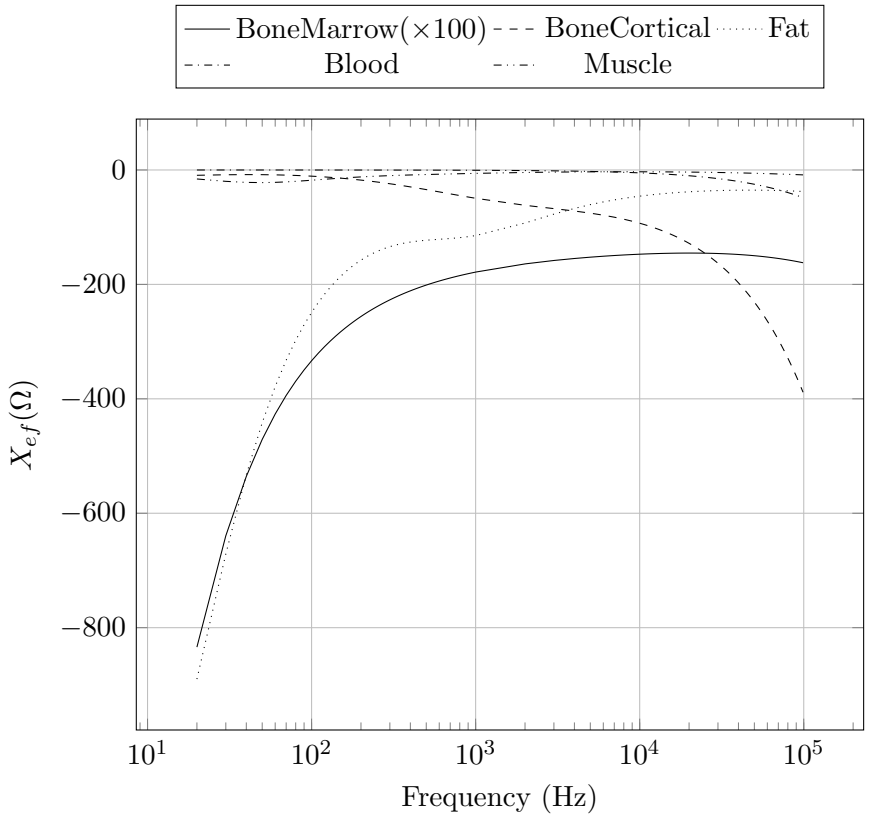

Figure 5.11: $Norm(X_{ef})$ of SLCM tissues on the MLCM

5.4 Lightning Injury correlation

5.4.1 SLCM

Section 2.2.4 classified major clinical symptoms of lightning injuries into three categories: neurological, cardiovascular and external burns. Tissues that are related to these sites of injuries are analysed. Appendix D correlates the tissue impedances of 19 tissues to lightning injuries.

Table 5.1 shows that aqueous tissues have the lowest impedances out of the 54 SLCMs and can be approximated to be purely resistive. From this, it can be deduced that most of the FSS current travels through the aqueous tissues compared to other tissues.

Neurological

Nerves are the main constituents of the nervous system [87]. Control and regulation of different parts of the body are achieved by sending electrical signals through the nerve fibres [87]. Neurological damage may occur if the FSS current disrupts the transmission of electrical signals in the nerves.

The nerve and spinal cord of the SLCM are classified in the same category as fat, which has a high impedance as seen in Figure B.4. From this, the FSS current is unlikely to traverse through the nerve and spinal cord. However, it must be noted that myelinated nerve fibres are wrapped around and protected by Schwann cells which contain a lipid substance *sphingomyelin* which is an excellent electrical insulator [87]. The measured ϵ_r and σ_e by Gabriel et al. [78] for nerve and spinal cord may be the result of this lipid layer, therefore the impedance is categorised the same as fat. From the SLCM simulation, the likelihood that the FSS current traverses the nerve and spinal cord is inconclusive. This is in accordance with Andrews [2], suggesting that the nerve tissue has a high impedance due to the lipid layer.

Accroding to Hall [87], even though electrical conduction is not possible through the Schwann cells, it can occur at the nodes of Ranvier[1]. Hence, as the FSS current traverses the extracellular fluid surrounding the nerves, the current may enter the nerve fibre through these nodes and neurological damage can occur.

[1] Uninsulated area between Schwann cells where ions can flow between the extracellular fluid and the intracellular fluid of the nerve fibres [87].

Cerebrospinal fluid has the lowest impedance out of all 54 SLCM as shown in Table 5.1. According to Hall [87], the cerebrospinal fluid is produced by the brain and circulates within the brain and the spinal cord. It is possible that the FSS current traverses the cerebrospinal fluid and thus through the nerves and spinal cord contained within the cerebrospinal fluid. This may contribute to the neurological symptoms that are observed in lightning injuries as listed in Table 2.1.

Cardiovascular

The heart tissue of the SLCM has a wide impedance range $55\,\Omega \sim 185\,\Omega$ as seen in Figure B.3 and has a relatively high impedance compared to other tissues. From this, the current is unlikely to travel through the heart and cause cardiovascular damage.

Ventricular fibrillation, asystole and cardio-respiratory progression are the most likely causes of cardiovascular fatalities as shown in Table 2.1. However, these are results of functional disturbances (uncoordinated heart rhythm) rather than structural changes (damages to the heart muscle itself) as detailed in Section 2.2.3. These may be caused by the disruption of signal transmission between the brain and the heart or the interruption of intracardiac conduction pathways. Therefore, the impedance results of the heart SLCM is not applicable in the analysis of cardiovascular injuries.

The disruption of the signal transmission between the brain and the heart may be result from neurological damage as explained in Section 5.4.1. According to Hall [87], the disruption of the intracardiac conduction pathways result in the block of heart signals. Various types of heart signal blocks that are fatal have been mentioned, all of which may be the results of the FSS current traversing the structures around the heart [87].

External Burns

During attachment to the human body, the first tissue that the FSS current encounters is skin. Dry and wet skin of the SLCM have the highest impedances as seen in Figure B.5. Due to this, the resistive power dissipation (P_{ef}) of these tissues are also the highest as seen in Figure B.10. P_{ef} quantifies heat dissipation and is used to explain the external burns of skin in lightning injuries. It should be noted that the impedance of the dry skin SLCM is high at frequencies below 1 kHz and decreases exponentially for higher frequencies as seen in Figure B.5. Half of the energy of the DEF is concentrated at frequencies below 2 kHz; this along with the high impedance of skin results in high heat dissipation and may be the cause of external burns due to skin breakdown.

5.4.2 MLCM

Lightning step voltage simulation on a voxel model of the human body conducted by Gao et al. [71] found that the highest current densities occur in the leg muscles and blood while weaker current densities are observed in bone and bone marrow. From Section 5.2.1, 85% of the FSS current flows through muscle and 11% flows through blood with the rest flowing through fat, bone cortical and bone marrow. Therefore, the results from the MLCM concur with the findings of Gao et al. [71].

Summary

The EF and EMF simulation approaches are carried out on 54 SLCMs and the results compared. Since the average absolute maximum errors between the two simulation approaches for all SLCMs are under 10^{-4}, and the simulation time for the EMF approach is on average eight times longer than the EF approach, the EF approach is preferred over the EMF approach.

From the SLCM simulations, the FSS currents are most likely to traverse aqueous tissues since these tissues have the lowest impedances. Only four tissues are found to be susceptible to magnetic field effects: cerebrospinal fluid, vitreous humour, gall bladder bile and gall bladder. However, the magnetic field effects have a minimal impact to the overall impedance and can be disregarded. Resistive power dissipations of the SLCMs are calculated and found to be proportional to the tissue impedances and current.

The EF simulation approach is applied to the MLCM. The current densities of the MLCM tissues are simulated and the current traversing through each tissue is calculated. 85% of the FSS current travels through muscle with 11% travelling through blood, 3.5% through fat and the rest through cortical bone and bone marrow.

Frequency dependent equivalent circuit models have been developed for the SLCM and the MLCM consisting of a resistor and a capacitor. The impedance results from the SLCM can be used to deduce the current pathway of the MLCM by scaling the impedance results from the SLCM. However, the exact values of current densities, tissue impedances and resistive power dissipation cannot be determined in this way.

The results of the simulations are used in the analysis of lightning injuries. Neurological injuries may be a result of the FSS current traversing the cerebrospinal fluid and entering the nervous tissue in this way. Cardiovascular injuries are functional disturbances and the results presented in this work are inconclusive in explaining the injury mechanism. External burns may be the result of the high heat dissipation of skin due to high skin impedance, resulting in breakdown of the tissue.

Chapter 6

Review and Future Work

Overview

This chapter reviews and critically analyses the findings of this work. Individual models used in this work including the FSS, SLCM and MLCM along with the physics modules are discussed. Recommendations of future work and the application of this work are given.

6.1 FSS

The FSS is modelled using the DEF as the frequency components can be obtained by analytical means. However, other models such as the Heidler function give a more realistic FSS waveform in the time domain. The frequency components of the Heidler function can be obtained by methods of numerical approximation and used in this work [88]. Further, the FSS waveforms obtained from lightning measurements in nature can be considered instead of mathematical models for realistic simulations. The frequency components of these measured FSS waveforms can be numerically approximated by using the fast fourier transform.

The FSS is only the initial part of the total lightning flash. Subsequent short strokes as well as long strokes should be investigated to examine the overall effects of the lightning flash. Viewing the FSS as a pre-stressing mechanism to the human tissues before tissue breakdown should also be considered.

6.2 SLCM

Human tissues are heterogeneous and anisotropic. This is too complex to incorporate into a simplified model of human tissues. Therefore, SLCM represents various human tissues as homogeneous and isotropic materials to simplify the FEA approach.

The SLCM is modelled with reference to the dimensions of human liver. This approach allows the tissue impedances of the SLCM to be compared on a per unit volume basis. However, tissue impedance is not calculated on volume alone as the current density is mainly reliant on the surface area.

Tissues such as the viterous humour, gall bladder, blood vessel and skin do not exist in the human body with volumes and dimensions that are comparable with liver. The actual dimensions and volumes of these tissues are not well known, hence the SLCM are constructed for these tissues. However, the analysis of these tissue geometries should not be disregarded.

Since a cylinder has a constant cross-sectional surface area, SLCM does not consider complex tissue surfaces. Therefore, the tissue impedances obtained from the SLCM are approximations and only used for impedance comparison between the tissues and do not represent the actual tissue impedances.

The actual impedance of the tissue can be modelled by only replacing the cylinder of the SLCM with the actual geometry of the tissue or organ. The proposed SLCM methodology remains the same. Since the simulation of the SLCM with the actual tissue geometry is difficult using FEA, the computing power required for the numerical simulations can only be realised with a computing cluster using parallel computing.

6.3 MLCM

The cylindrical structure of the MLCM is based on the structure of the SLCM. Even though the human leg is approximately cylindrically shaped, using a cylindrical model as the human leg may not be an accurate representation. A more detailed model of the human leg can be constructed using the complex geometric models as detailed in Section C. However, due to computing and image segmentation limits, a simplified cylindrical model (MLCM) is implemented and the results obtained are considered to be rough approximations.

The cross-sectional surface area of the tissue is significant in determining the impedance and the current pathway. However, the surface areas of real human tissues are not constant and complicates analysis, therefore the volume approach of the MLCM is used instead with reasons similar to the SLCM.

The EMF approach is not carried out on the MLCM as the cylindrical geometry is simple and the results from the EF approach are sufficient. For accurate results, the EMF approach should be used for all models rather than the EF. This considers magnetically induced effects but requires more numerical calculations. This requires high end computing power such as the use of a computing cluster.

The MLCM can be applied to various parts of the human body. More tissue layers such as nerves and lymph can be added to the MLCM to better represent the corresponding part of the human body.

An accurately segmented full human body model can be used instead of the MLCM. However, an accurately segmented full human body model requires an experienced medical staff to conduct the time consuming process of manually inspecting the MRI/CAT scans of the entire human body. The same simulation procedures conducted on the MLCM can be carried out on the fully segmented voxel model of the human body.

If high end computing power is available, human tissue models can be examined at a cellular level as described in Section 2.4.2. This accounts for the inhomogeneous and non-linear properties of real human tissues.

6.4 Physics

The EF approach is preferred over the EMF approach as the results from both approaches are similar with absolute maximum errors in the 10^{-4} region. The simulation time needed by the EMF approach is on average eight times more than the EF approach, hence it was judged that the return is not worth the computational effort. If the computing power were available, such as the use of a computing cluster, the EMF approach should replace the EF approach. Frequency components can be simulated with a finer resolution to accurately represent the continuous frequency spectrum.

Power dissipation is the only quantifiable measure if continuous sinusoidal waves are utilised to model the frequency components of the FSS. However, the FSS is a transient waveform and energy dissipation is a more applicable measurement. This is not implemented as this research focuses on the effects of the FSS frequency components on the current pathway, power loss is sufficient in explaining these effects.

Energy loss can be obtained by integrating the FSS waveform in the time domain to determine the total charge of the FSS. An energy spectral density analysis can then be performed in the frequency domain of the FSS and the frequencies with the most energy can be calculated.

The heating effects of the FSS can also be modelled by obtaining the thermal properties of human tissues along with the dielectric properties. The thermal properties include: specific heat ($J.g^{-1}.K^{-1}$), tissue density (m/v) and thermal conductivity ($W.m^{-1}.K^{-1}$) [70].

The tissue SAR can be determined to observe temperature changes as a result of the FSS current. From this, damages to the tissue due to heating effects can be examined.

6.5 Application

This work lays a theoretical foundation for future experimental work. Even though the results concur with established research, experiments pertaining to this work should be conducted. An impulse generator with standard waveform can be connected to the top and bottom metal plates of a perspex cylinder filled with a substance of known dielectric properties. This can be simulated using the SLCM and the results compared with the actual measurements.

The results of this work are applicable in the analysis of HV injuries. Since continuous sinusoidal currents at various frequencies are simulated individually, the results at power frequencies can be isolated and analysed.

Chapter 7

Conclusion

The FSS frequency components are analysed and extracted using the DEF model. The frequency components are in the range 10 Hz $\sim$ 100 kHz. Each frequency component is modelled individually as a continuous sinusoidal current source and passed through human tissue models. Two simplified human tissue models are developed: SLCM and MLCM. The models are simulated in COMSOL using FEA.

54 human tissues are modelled using the SLCM, each defined using the respective dielectric properties. All SLCMs are constructed to have the same dimensions as liver. Two simulation approaches, EF and EMF, are conducted on the SLCM. Three aspects are considered in the result analysis: current densities, power dissipation and tissue impedances. The tissue impedances obtained from the EF approach have maximum absolute errors in the 10^{-5} region compared to the EMF approach. The results from the SLCM show that for the same tissue volume, the FSS current prefers the route of aqueous tissues compared to other tissues. Power dissipation is used to quantify heat dissipation and is directly related to the tissue impedance. Since the simulation time required by the EMF approach is on average eight times more than the EF approach, the EF approach is used in the simulation of the MLCM.

A human right leg is modelled using the MLCM. Five tissue layers are modelled: bone marrow, cortical bone, muscle, blood and fat. The results from the EF approach show that 85% of the FSS current flows through muscle with 11% travelling through blood, 3.5% flowing through fat and the remainder through cortical bone and bone marrow.

The results from the SLCM are used to predict the current pathway in the MLCM through impedance comparison. The scaling of the SLCM impedances yields proportional impedances to the MLCM tissues allowing the current pathway to be predicted.

Three main categories of lightning injuries: neurological, cardiovascular and external burns are compared with results from the SLCM and MLCM simulations. Neurological injuries may occur from the FSS current travelling through the cerebrospinal fluid before entering the nerve fibres. Cardiovascular injuries may not be a result of damage to the heart tissue itself, but rather functional disturbances which disrupts the coordinated rhythms of the heart. External burns may be due to the high impedance of skin which results in high heat dissipation and causes external burns.

This work can be applied to the analysis of HV injuries by examining the results at power frequencies. Greater computing power is required for the simulation of an accurate voxel human body model rather than cylindrical models. Thermal properties of human tissues can be incorporated with dielectric properties to examine heating effects and determine physical tissue damage. All results are obtained via simulation and experimental results are required to validate the findings of this work.

REFERENCES

[1] "Protection Against Lightning-Part 1: General Principles," Jan. 2006.

[2] C. J. Andrews, "Electrical Aspects of Lightning Strikes to Humans," in *The Lightning Flash*, V. Cooray, Ed. London: IEEE Press, 2003, ch. 11, pp. 548–564.

[3] P. A. Yushkevich, J. Piven, and H. Cody Hazlett, "User-Guided (3D) Active Contour Segmentation of Anatomical Structures: Significantly Improved Efficiency and Reliability," *Neuroimage*, vol. 31, no. 3, pp. 1116—-1128, 2006.

[4] "Effects of Currents on Human Beings and Livestock-Part 4: Effects of lightning strokes on human beings and live stock," Apr. 2004.

[5] C. J. Andrews, M. A. Cooper, T. D. Jacobsen, E. P. Kenzelok, L. Shicker, and S. L. Weiner, "Lightning Injuries," *Disease-a-Month*, vol. 43, no. 12, pp. 871–891, 1997. [Online]. Available: http://www.sciencedirect.com/science/article/pii/S0011502997900249

[6] Y.-C. Lee, D. M. Rubin, and I. R. Jandrell, "Use of dielectric properties of human tissues in the analysis of lightning injuries," in *Lightning Protection (ICLP), 2014 International Conference o*, Oct. 2014, pp. 1223–1228.

[7] J. Kuffel, E. Kuffel, and W. S. Zaengl, *High Voltage Engineering Fundamentals*. Elsevier Science, 2000. [Online]. Available: http://books.google.co.za/books?id=u71WSDOkzxIC

[8] "Protection Against Lightning-Part 3: Physical damage to structures and life hazard," Jan. 2006.

[9] M. Darveniza, "Electrical Aspects of Lightning Injury and Damage," in *Lightning Injuries: Electrical, Medical, and Legal Aspects*. CRC Press, 1992, ch. 3, pp. 23–37.

[10] R. H. Golde, "Lightning Currents and Related Parameters," in *Lightning, Vol.1. Physics of Lightning*. Academic Press, 1977, ch. 9.

[11] V. Cooray, *The Lightning Flash*, ser. IEE Power Series. Institution of Engineering and Technology, 2003. [Online]. Available: https://books.google.co.za/books?id=2b3_IztUdmEC

[12] J. C. Willett, D. M. Le Vine, and V. P. Idone, "Lightning return stroke current waveforms aloft from measured field change, current, and channel geometry," *Journal of Geophysical Research*, vol. 113, no. D7, p. D07305, Apr. 2008. [Online]. Available: http://doi.wiley.com/10.1029/2006JD008116

[13] V. A. Rakov and M. A. Uman, *Lightning: Physics and Effects*. Cambridge University Press, 2007.

[14] V. Javor, "Modeling of Lightning Strokes Using Two-Peaked Channel-Base Currents," *International Journal of Antennas and Propagation*, vol. 2012, 2012.

[15] C. E. R. Bruce and R. H. Golde, "The lightning discharge," *Electrical Engineers - Part II: Power Engineering, Journal of the Institution of*, vol. 88, no. 6, pp. 487–505, 1941.

[16] F. Heidler and J. Cvetić, "A class of analytical functions to study the lightning effects associated with the current front," *European Transactions on Electrical Power*, vol. 12, no. 2, pp. 141–150, Mar. 2002. [Online]. Available: http://doi.wiley.com/10.1002/etep.4450120209

[17] H. Wei, X. Ba-lin, and G. You-gang, "Analysis of the lightning waveshape," in *2004 Asia-Pacific Radio Science Conference, 2004. Proceedings.* IEEE, 2004, pp. 627–630.

[18] V. Slavko and D. Lovric, "Exponential approximation of the Heidler function for the reproduction of lightning current waveshapes," *Electric Power Systems Research*, vol. 80, no. 10, pp. 1293–1298, 2010.

[19] V. Javor and P. D. Rancic, "A Channel-Base Current Function for Lightning Return-Stroke Modeling," *Electromagnetic Compatibility, IEEE Transactions on*, vol. 53, no. 1, pp. 245–249, Feb. 2011.

[20] Z. Feizhou and L. Shanghe, "A new function to represent the lightning return-stroke currents," *Electromagnetic Compatibility, IEEE Transactions on*, vol. 44, no. 4, pp. 595–597, Nov. 2002.

[21] G. I. Serhan, M. A. Uman, D. G. Childers, and Y. T. Lin, "The RF spectra of first and subsequent lightning return strokes in the 1- to 200-km range," *Radio Science*, vol. 15, no. 6, pp. 1089–1094, 1980. [Online]. Available: http://dx.doi.org/10.1029/RS015i006p01089

[22] C. D. Weidman and E. P. Krider, "The amplitude spectra of lightning radiation fields in the interval from 1 to 20 MHz," *Radio Science*, vol. 21, no. 6, pp. 964–970, 1986. [Online]. Available: http://dx.doi.org/10.1029/RS021i006p00964

[23] C. D. Weidman, E. P. Krider, and M. A. Uman, "Lightning amplitude spectra in the interval from 100 kHz to 20 MHz," *Geophysical Research Letters*, vol. 8, no. 8, pp. 931–934, 1981. [Online]. Available: http://dx.doi.org/10.1029/GL008i008p00931

[24] R. L. Holle, "Annual Rates of Lightning Fatalities By Country," in *20th International Lightning Detection Conference*, Tucson, Arizona, USA, Apr. 2008.

[25] R. L. Holle and R. E. López, "A comparison of current lightning death rates in the U.S. with other locations and times," in *Intl. Conf. on Lightning and Static Electricity, Royal Aeronautical Society*, ser. paper 103-34 KMS, Blackpool, England, 2003.

[26] R. L. Holle, "Recent studies of lightning safety and demographics," in *2012 International Conference on Lightning Protection (ICLP)*. Ieee, Sep. 2012, pp. 1–14. [Online]. Available: http://ieeexplore.ieee.org/lpdocs/epic03/wrapper.htm?arnumber=6344218

[27] R. Blumenthal, E. Trengrove, I. Jandrell, and G. Saayman, "Lightning medicine in South Africa," *South African Medical Journal*, vol. 102, no. 7, 2012. [Online]. Available: http://www.samj.org.za/index.php/samj/article/view/5219

[28] R. Blumenthal, "Lightning Fatalities on the South African Highveld: A Retrospective Descriptive Study for the Period 1997 to 2000," *The American Journal of Forensic Medicine and Pathology*, vol. 26, no. 1, pp. 66–69, Mar. 2005. [Online]. Available: http://content.wkhealth.com/linkback/openurl?sid=WKPTLP:landingpage&an=00000433-200503000-00011

[29] W. R. Lee, "Lightning Injuries and Death," in *Lightning, Vol 2. Lightning Protection*. London: Academic Press, 1977, ch. 16, pp. 521–543.

[30] R. Anderson, "Does a fifth mechanism exist to explain lightning injuries?" *IEEE Engineering in Medicine and Biology Magazine*, vol. 20, no. 1, pp. 105–113, Jan. 2001. [Online]. Available: http://ieeexplore.ieee.org/lpdocs/epic03/wrapper.htm?arnumber=897833

[31] M. A. Cooper, "A fifth mechanism of lightning injury." *Acad Emerg Med*, vol. 9, no. 2, pp. 172–174, Feb. 2002.

[32] R. Blumenthal, I. R. Jandrell, and N. J. West, "Does a sixth mechanism exist to explain lightning injuries?: investigating a possible new injury mechanism to determine the cause of injuries related to close lightning flashes." *The American journal of forensic medicine and pathology*, vol. 33, no. 3, pp. 222–6, Sep. 2012. [Online]. Available: http://www.ncbi.nlm.nih.gov/pubmed/21952103

[33] V. A. Rakov and M. A. Uman, "Deleterious effects of lightning and protective techniques," in *Lightning: Physics and Effects*. Cambridge University Press, 2007, ch. 18.

[34] C. J. Andrews and M. A. Cooper, "Clinical Presentation of the Lightning Victim," in *Lightning Injuries: Electrical, Medical, and Legal Aspects*. CRC Press, 1992, ch. 5, pp. 47–68.

[35] C. Pfortmueller, Y. Yikun, M. Haberkern, E. Wuest, H. Zimmermann, and A. K. Exadaktylos, "Injuries, sequelae, and treatment of lightning-induced injuries: 10 years of experience at a swiss trauma center." *Emergency medicine international*, vol. 2012, p. 167698, Jan. 2012. [Online]. Available: http://www.pubmedcentral.nih.gov/articlerender.fcgi?artid=3361158&tool=pmcentrez&rendertype=abstract

[36] P. B. Fontanarosa, "Electrical shock and lightning strike." *Ann Emerg Med*, vol. 22, no. 2 Pt 2, pp. 378–387, Feb. 1993.

[37] M. A. Cooper, "Emergent care of lightning and electrical injuries." *Seminars in neurology*, vol. 15, no. 3, pp. 268–78, Sep. 1995. [Online]. Available: http://www.ncbi.nlm.nih.gov/pubmed/8570929

[38] L. A. Geddes and R. A. Roeder, *Handbook of Electrical Hazards and Accidents*. Lawyers & Judges Publishing Company, 2006. [Online]. Available: http://books.google.co.za/books?id=Pb4lUnSsMa0C

[39] P. Sutherland, D. Dorr, and K. Gomatom, "Human current sensitivities and resistance values in the presence of electrically energized objects," in *IEEE Systems Technical Conference on Industrial and Commercial Power 2005.* Ieee, May 2005, pp. 159–167. [Online]. Available: http://ieeexplore.ieee.org/lpdocs/epic03/wrapper.htm?arnumber=1436370

[40] "Effects of Currents on Human Beings and Livestock-Part 1: General Aspects," Apr. 2005.

[41] "IEEE Guide for Safety in AC Substation Grounding," Jan. 2000.

[42] T. Bracken, G. Sias, C. Kim, R. Senior, and R. Patterson, "Survey of Electrical Utility Worker Body Impedance," *IEEE Transactions on Power Delivery*, vol. 23, no. 2, pp. 1251–1259, Apr. 2008. [Online]. Available: http://ieeexplore.ieee.org/lpdocs/epic03/wrapper.htm?arnumber=4472155

[43] J. Reilly, "Impedance and Current Distribution," in *Applied Bioelectricity*. Springer New York, 1998, ch. 2, pp. 12–72.

[44] L. Gordon, B. Appelt, and J. Mitchell, "The complex dielectric nature of the human body," in *1998 Annual Report Conference on Electrical Insulation and Dielectric Phenomena (Cat. No.98CH36257)*. Ieee, 1998, pp. 577–580. [Online]. Available: http://ieeexplore.ieee.org/lpdocs/epic03/wrapper.htm?arnumber=732963

[45] C.-H. Lee and A. P. Sakis Meliopoulos, "Comparison of touch and step voltages between IEEE Std 80 and IEC 479-1," *IEE Proceedings - Generation, Transmission and Distribution*, vol. 146, no. 6, p. 593, Nov. 1999. [Online]. Available: http://digital-library.theiet.org/content/journals/10.1049/ip-gtd_19990586

[46] C. F. Dalziel and W. R. Lee, "Reevaluation of Lethal Electric Currents," *IEEE Transactions on Industry and General Applications*, vol. IGA-4, no. 5, pp. 467–476, Sep. 1968. [Online]. Available: http://ieeexplore.ieee.org/lpdocs/epic03/wrapper.htm?arnumber=4180929

[47] C. F. Dalziel, "Electric shock hazard," *IEEE Spectrum*, vol. 9, no. 2, pp. 41–50, Feb. 1972. [Online]. Available: http://ieeexplore.ieee.org/lpdocs/epic03/wrapper.htm?arnumber=5218692

[48] C. Dalziel, "A Study of the Hazards of Impulse Currents," *Transactions of the American Institute of Electrical Engineers. Part III: Power Apparatus and Systems*, vol. 72, no. 2, pp. 1032–1043, Jan. 1953. [Online]. Available: http://ieeexplore.ieee.org/lpdocs/epic03/wrapper.htm?arnumber=4498738

[49] H. Kanai, I. Chatterjee, and O. Gandhi, "Human Body Impedance for Electromagnetic Hazard Analysis in the VLF to MF Band," *IEEE Transactions on Microwave Theory and Techniques*, vol. 32, no. 8, pp. 763–772, Aug. 1984. [Online]. Available: http://ieeexplore.ieee.org/lpdocs/epic03/wrapper.htm?arnumber=1132770

[50] I. Chatterjee, D. Wu, and O. P. Gandhi, "Human body impedance and threshold currents for perception and pain for contact hazard analysis in the VLF-MF band." *IEEE transactions on bio-medical engineering*, vol. 33, no. 5, pp. 486–94, May 1986. [Online]. Available: http://www.ncbi.nlm.nih.gov/pubmed/3710504

[51] M. Hammam and R. Baishiki, "A Range of Body Impedance Values for Low Voltage, Low Source Impedance Systems of 60 HZ," *IEEE Transactions on Power Apparatus and Systems*, vol. PAS-102, no. 5, pp. 1097–1105, May 1983. [Online]. Available: http://ieeexplore.ieee.org/lpdocs/epic03/wrapper.htm?arnumber=4112043

[52] Deshpande, *Electronic Devices & Circuits - Principles & Applications*. McGraw-Hill Education (India) Pvt Limited, 2008. [Online]. Available: https://books.google.co.za/books?id=EJUO5bf3YooC

[53] N. R. Misbah, M. Z. a. A. Kadir, and C. Gomes, "Modelling and analysis of different aspect of mechanisms in lightning injury," in *2011 Fourth International Conference on Modeling, Simulation and Applied Optimization*. Ieee, Apr. 2011, pp. 1–5. [Online]. Available: http://ieeexplore.ieee.org/lpdocs/epic03/wrapper.htm?arnumber=5775551

[54] D. S. Gazzana, A. S. Bretas, G. a. D. Dias, M. Tello, D. W. P. Thomas, and C. Christopoulos, "Contribution to the study of human safety against lightning considering the grounding system influence and the variations of the associated parameters," in *2012 International Conference on Lightning Protection (ICLP)*. Ieee, Sep. 2012, pp. 1–5. [Online]. Available: http://ieeexplore.ieee.org/lpdocs/epic03/wrapper.htm?arnumber=6344290

[55] C. Gabriel, S. Gabriel, and E. Corthout, "The dielectric properties of biological tissues: I. Literature survey." *Phys Med Biol*, vol. 41, no. 11, pp. 2231–2249, Nov. 1996.

[56] R. Pethig and D. B. Kell, "The passive electrical properties of biological systems: their significance in physiology, biophysics and biotechnology," *Physics in Medicine and Biology*, vol. 32, no. 8, p. 933, 1987.

[57] M. Talaat, "Charge simulation modeling for calculation of electrically induced human body currents," in *2010 Annual Report Conference on Electrical Insulation and Dielectic Phenomena*. Ieee, Oct. 2010, pp. 1–4. [Online]. Available: http://ieeexplore.ieee.org/lpdocs/epic03/wrapper.htm?arnumber=5723972

[58] S. Watanabe, N. Hirose, T. Nagaoka, N. Hatakenaka, Y. Tanaka, M. Takahashi, Y. Suzuki, M. Taki, J. Wang, O. Fujiwara, and Y. Yamanaka, "Development of Smart Voxel Models of Whole Human-bodies for Numerical Dosimetry," *International Symposium on Electromagnetic Compatibility*, vol. 2, pp. 797–800, 2004.

[59] C. H. Durney, "Electromagnetic dosimetry for models of humans and animals: A review of theoretical and numerical techniques," *Proceedings of the IEEE*, vol. 68, no. 1, pp. 33–40, Jan. 1980.

[60] C. C. Johnson, C. H. Durney, and H. Massoudi, "Electromagnetic Power Absorption in Anisotropic Tissue Media (Short Papers)," *Microwave Theory and Techniques, IEEE Transactions on*, vol. 23, no. 6, pp. 529–532, Jun. 1975.

[61] J. C. Lin, A. W. Guy, and C. C. Johnson, "Power Deposition in a Spherical Model of Man Exposed to I-20-MHz Electromagnetic Fields," *Microwave Theory and Techniques, IEEE Transactions on*, vol. 21, no. 12, pp. 791–797, Dec. 1973.

[62] F. Lacroux, A. Cortel Carrasco, A. Gati, M.-F. Wong, and J. Wiart, "SAR and averaged power density near a UMTS base-station antenna," in *Microwave Symposium Digest, 2006. IEEE MTT-S International*, Jun. 2006, pp. 1987–1990.

[63] T. Nagaoka, T. Togashi, K. Saito, M. Takahashi, K. Ito, T. Ueda, H. Osada, H. Ito, and S. Watanabe, "An anatomically realistic voxel model of the pregnant woman and numerical dosimetry for a whole-body exposure to RF electromagnetic fields," in *Engineering in Medicine and Biology Society, 2006. EMBS '06. 28th Annual International Conference of the IEEE*, Aug. 2006, pp. 5463–5467.

[64] H. Fahs, A. Hadjem, S. Lanteri, J. Wiart, and M.-F. Wong, "Calculation of the SAR Induced in Head Tissues Using a High-Order DGTD Method and Triangulated Geometrical Models," *Antennas and Propagation, IEEE Transactions on*, vol. 59, no. 12, pp. 4669–4678, Dec. 2011.

[65] A. Pradier, F. Lacroux, D. Lautru, M.-F. Wong, V. F. Hanna, and J. Wiart, "Influence of the homogenization of tissues on the electric field Calculation in Numerical Dosimetry for wireless Application," in *Wireless Technology, 2006. The 9th European Conference on*, Sep. 2006, pp. 127–130.

[66] O. P. Gandhi and J. Y. Chen, "Numerical dosimetry at power-line frequencies using anatomically based models." *Bioelectromagnetics*, vol. 13, no. Supplement 1, pp. 43–60, Jan. 1992. [Online]. Available: http://www.ncbi.nlm.nih.gov/pubmed/1285721

[67] F. Ruan, T. Dlugosz, D. Shi, and Y. Gao, "Cylinder model of human body impedance based on proximity effect," in *Microwave, Antenna, Propagation and EMC Technologies for Wireless Communications, 2009 3rd IEEE International Symposium on*, Oct. 2009, pp. 16–19.

[68] J. Werner and P. Webb, "A Six-cylinder Model of for General Use on Human Thermoregulation Personal Computers," *The Annals of physiological anthropology*, vol. 12, no. 3, pp. 123–134, 1993.

[69] D. Muramatsu, F. Koshiji, and K. Sasaki, "Multilayered cylindrical human arm model for impedance analysis in human body communication," in *Communications (APCC), 2012 18th Asia-Pacific Conference on*, Oct. 2012, pp. 478–479.

[70] H. S. Ho, A. W. Guy, R. A. Sigelmann, and J. F. Lehmann, "Microwave Heating of Simulated Human Limbs by Aperture Sources," *Microwave Theory and Techniques, IEEE Transactions on*, vol. 19, no. 2, pp. 224–231, Feb. 1971.

[71] J. Gao, I. Munteanu, W. F. O. Müller, and T. Weiland, "Generation of postured voxel-based human models for the study of step voltage excited by lightning current," *Advances in Radio Science*, vol. 9, pp. 99–105, Jul. 2011. [Online]. Available: http://www.adv-radio-sci.net/9/99/2011/

[72] D. Poljak, S. Sesnic, M. Birkic, and D. Kosor, "Towards the model for the assessment of the current density induced in the human body due to the electric field irradiated from the rod struck by lightning," in *2007 15th International Conference on Software, Telecommunications and Computer Networks*. Ieee, Sep. 2007, pp. 1–6. [Online]. Available: http://ieeexplore.ieee.org/lpdocs/epic03/wrapper.htm?arnumber=4446079

[73] D. Andreuccetti, R. Fossi, and C. Petrucci, "An Internet resource for the calculation of the dielectric properties of body tissues in the frequency range 10 Hz - 100 GHz," *Website at http://niremf.ifac.cnr.it/tissprop/*, vol. IFAC-CNR, 1997.

[74] N. Mitsuhashi, K. Fujieda, T. Tamura, S. Kawamoto, T. Takagi, and K. Okubo, "BodyParts3D: 3D structure database for anatomical concepts," pp. D782–5, Jan. 2009.

[75] M. J. Ackerman, "The Visible Human Project," *Proceedings of the IEEE*, vol. 86, no. 3, pp. 504–511, Mar. 1998.

[76] COMSOL, "ACDC Module User's Guide," Oct. 2014.

[77] S. Gabriel, R. W. Lau, and C. Gabriel, "The dielectric properties of biological tissues: II. Measurements in the frequency range 10 Hz to 20 GHz," *Phys Med Biol*, vol. 41, no. 11, pp. 2251–2269, 1996.

[78] S. Gabriel, R. Lau, and C. Gabriel, "The dielectric properties of biological tissues: III. Parametric models for the dielectric spectrum of tissues," *Phys Med Biol*, vol. 41, no. 11, pp. 2271–2293, 1996.

[79] K. S. Cole and R. H. Cole, "Dispersion and Absorption in Dielectrics I. Alternating Current Characteristics," *The Journal of Chemical Physics*, vol. 9, no. 4, 1941.

[80] C. Gabriel, "Compilation of the Dielectric Properties of Body Tissues at RF and Microwave Frequencies," Brooks Air Force Base, Occupational and environmental health directorate, Radiofrequency Radiation Division, Brooks Air Force Base, Texas (USA), Tech. Rep., 1996. [Online]. Available: http://books.google.co.za/books?id=4MvhMgEACAAJ

[81] D. C. Wolf, "Evaluation of the Size, Shape, and Consistency of the Liver," in *Clinical Methods: The History, Physical, and Laboratory Examinations*, 3rd ed., H. Walker, W. Hall, and J. Hurst, Eds., Boston, 1990, vol. 62, no. 6, ch. 94, pp. 478–481.

[82] Visual Computing Lab, "MeshLab," 2005.

[83] J. D. Kraus, *Antennas*, ser. Electrical Engineering Series. McGraw-Hill, 1988. [Online]. Available: https://books.google.co.za/books?id=XYxhQgAACAAJ

[84] A. R. Clark, *A Study Guide for Electromagnetics (and antennas) - with SuperNEC applications*, 1st ed. Johannesburg: Poynting Innovations (Pty) Ltd, 2004.

[85] E. M. Purcell and D. J. Morin, *Electricity and Magnetism*, ser. Electricity and Magnetism. Cambridge University Press, 2013. [Online]. Available: https://books.google.co.za/books?id=A2rS5vlSFq0C

[86] H. A. Haus and J. R. Melcher, "Electromagnetic Fields and Energy," 1989. [Online]. Available: http://ocw.mit.edu/resources/res-6-001-electromagnetic-fields-and-energy-spring-2008/chapter-11/11.pdf

[87] J. E. Hall, *Guyton and Hall Textbook of Medical Physiology*, ser. Guyton Physiology. Elsevier Health Sciences, 2010. [Online]. Available: https://books.google.co.za/books?id=Po0zyO0BFzwC

[88] D. Lovri and S. Vujevi, "On the estimation of Heidler function parameters for reproduction of various standardized and recorded lightning current waveshapes," *International Transactions on Electrical Energy Systems*, 2011.

[89] J. C. Slater and N. H. Frank, *Electromagnetism*, ser. Dover Books on Physics. Dover Publications, 2012. [Online]. Available: https://books.google.co.za/books?id=hsDDAgAAQBAJ

[90] S. Orfanidis, *Electromagnetic Waves and Antennas*. ECE Department, Rutgers University, 2008. [Online]. Available: http://www.ece.rutgers.edu/~orfanidi/ewa

[91] C. A. Balanis, *Advanced Engineering Electromagnetics*. John Wiley & Sons, Ltd, 1989.

[92] F. Martini and J. L. Nath, *Anatomy and Physiology*. Benjamin Cummings, 2010. [Online]. Available: https://books.google.co.za/books?id=dlz9ZwEACAAJ

Appendix A

Maxwell's Equations

A.1 Introduction

This appendix details the derivations of Maxwell's Equations for FEA simulation of the SLCM and MLCM. The EMF and EF approaches are discussed and the final differential equations used for each model type is presented.

A.2 Maxwell's Equations

Point form of Maxwell's equations [89]:

$$\nabla \cdot \vec{D} = \rho_v \tag{A.1}$$

$$\nabla \cdot \vec{B} = 0 \tag{A.2}$$

$$\nabla \times \vec{E} = -\frac{\partial \vec{B}}{\partial t} \tag{A.3}$$

$$\nabla \times \vec{H} = \frac{\partial \vec{D}}{\partial t} + \vec{J} \tag{A.4}$$

where:

$\vec{D}$	electric flux density
ρ_v	total charge
$\vec{B}$	magnetic flux density
$\vec{E}$	electric field
$\vec{H}$	magnetic field
$\vec{J}$	conduction electric current density

$\vec{J}$, $\vec{D}$ and $\vec{B}$ are each defined as [90]:

$$\vec{J} = \sigma\vec{E} \tag{A.5}$$

$$\vec{D} = \epsilon\vec{E} \tag{A.6}$$

$$\vec{B} = \mu\vec{H} \tag{A.7}$$

The FSS current traversing the tissue is the main focus in this research. Hence, Maxwell-Ampere's equation shown in Equation (A.4) is used. Frequency domain analysis is conducted on the SLCM and the MLCM, hence the time-harmonic form of Equation (A.4) is transformed and shown in Equation (A.8).

$$\nabla \times \vec{H} = \vec{J} + j\omega\vec{D} \tag{A.8}$$

A.2.1 Current calculation

The current flowing through a surface S with cross sectional surface area a is defined as shown in Equation (A.9) [85]. Given the current density and the dimensions of the model, current travelling through the model can be calculated.

$$|i(t)| = \int_S \vec{J} \cdot d\vec{a} \tag{A.9}$$

Charge conservation

In a closed system, the law of charge conservation needs to be obeyed [85]. The total charge in the system therefore needs to remain constant. The total charge inside an enclosed volume is $\int_{V_{ol}} \rho \; dV_{ol}$ and since Equation (A.9) is the instantaneous rate at which charge is leaving an area in the system, Equation (A.10) can be derived.

As the geometry of the human tissue model is much smaller than the wavelength of the current, it can be assumed that the propagation speed of electromagnetic fields is instant; this assumption is called the *quasi-static approximation* [85]. Using this approximation, (A.10) can be further collapsed to form the *equation of continuity* as shown in Equation (A.11) [85].

$$\int_S \vec{J} \cdot d\vec{A} = -\frac{d}{dt} \int_{V_{ol}} \rho \; dV_{ol} \tag{A.10}$$

$$\nabla \cdot \vec{J} = 0 \tag{A.11}$$

Current density calculation

The current that is flowing through a medium depends on the current density as shown in Equation (A.9). The total current density needs to satisfy Maxwell-Ampere's law as shown in Equation (A.8). From Equation (A.8), the current density $\vec{J}$ consists of two parts [85]. The first part is the *bound charge current density* J_e which results from an external excitation of a source to the medium. The second part is the *free charge current density* described in Equation (A.5) as the conduction electric current density. The displacement current $j\omega\vec{D}$ term takes into account any capacitances that may exist in the medium [90]. The total current density in the system is thus shown in Equation (A.12) as the sum of the aforementioned current densities.

$$\nabla \times \vec{H} = \vec{J_{total}} = \vec{J_e} + \sigma\vec{E} + j\omega\vec{D} \tag{A.12}$$

A.2.2 Voltage Calculation

For the ease of calculation of the electrodynamic fields, a magnetic vector potential $\vec{A}$ is defined such that [85]:

$$\vec{B} = \nabla \times \vec{A} \tag{A.13}$$

$$\vec{E} = -\nabla V - j\omega\vec{A} \tag{A.14}$$

Equation (A.12) can be rewritten as Equation (A.15). Equation (A.14) can then be substituted into Equation (A.15) to yield Equation (A.16).

$$\vec{J_{total}} = \vec{J_e} + \sigma\vec{E} + j\omega\epsilon\vec{E} \tag{A.15}$$

$$\vec{J_{total}} = \vec{J_e} + \sigma(-\nabla V - j\omega\vec{A}) + j\omega\epsilon(-\nabla V - j\omega\vec{A}) \tag{A.16}$$

Equation (A.16) is equivalent to Equation (A.8) and Equation (A.17) can be derived. This differential equation can thus be used to calculate the scalar voltage V by solving for both the electric and magnetic fields.

$$\nabla \times H = \vec{J_e} - \nabla V(j\omega\epsilon + \sigma) + \vec{A}(\omega^2\epsilon - j\omega\sigma) \tag{A.17}$$

A.3 Maxwell's Equations Considering only Electric Fields

The use of Maxwell's Equations in the calculation regarding only electric fields is mostly identical as Section A.2. The only difference is in the voltage calculation as detailed in Section A.3.1.

A.3.1 Voltage calculation

As the magnetic fields and any magnetically induced currents are assumed negligible in human tissues, it is not necessary to solve for $\vec{H}$ in Equation (A.8). The divergence of any curl is zero [89], hence the divergence of Equation (A.8) can be represented as Equation (A.18). Substituting Equation (A.8) into Equation (A.18) gives Equation (A.19).

$$\nabla \cdot \nabla \times \vec{H} = 0 \tag{A.18}$$

$$\nabla \cdot (j\omega \vec{D} + \vec{J}) = 0 \tag{A.19}$$

$\vec{J}$ and $\vec{D}$ of Equation (A.19) are replaced with Equations (A.5) and (A.6) such that $\vec{E}$ is the only vector. This yields Equation (A.20).

$$\nabla \cdot (\vec{E}(j\omega\epsilon + \sigma)) = 0 \tag{A.20}$$

From Faraday's law, the curl of the electrostatic field is zero and an electric potential can be defined as shown in Equation (A.21) [85]. This equation is the same as Equation (A.14) but with $\vec{A} = 0$.

$$\vec{E} = -\nabla V \tag{A.21}$$

Replacing $\vec{E}$ in Equation (A.20) with Equation (A.21) yields Equation (A.22). This differential equation is used to solve for the scalar voltage V in the frequency domain.

$$\nabla \cdot (-\nabla V(j\omega\epsilon + \sigma)) = 0 \tag{A.22}$$

A.4 Electromagnetic Energy Losses

$$P_s = P_e + P_d + jw(W_e + W_m) \tag{A.23}$$

$$P_e = \oint_s \int \vec{E} \times \vec{H} \cdot d\vec{S} \tag{A.24}$$

$$P_d = \int_v \vec{E} \cdot \vec{J} = \int_v \sigma_e |\vec{E}|^2 dv \tag{A.25}$$

$$W_m = \int_v \mu |\vec{H}|^2 dv \tag{A.26}$$

$$W_e = \int_v \epsilon |\vec{E}|^2 dv \tag{A.27}$$

The total power transferred and absorbed by the medium can be defined by Equations (A.23) $\sim$ (A.27) [91] where:

P_s	total supplied power	v	volume of the medium
P_e	transmitted power	S	surface of the medium
P_d	dissipated power	W_e	stored electric energy
W_m	stored magnetic energy		

This equation is valid if complex permeability is ignored and the human tissue relative permeability $\mu = 1$ is assumed. As the power loss in the form of heat is the primary concern, only the resistive dissipated power P_d is analysed.

A.5 Conclusion

The current density calculation for both the EF and EMF approaches are identical. The only difference between the EF and EMF is the voltage calculations. The EMF considers the magnetic vector potential in the calculation of voltage while this term is neglected in the EF approach. Only the resistive dissipated power is considered as this describes heat dissipation in the tissues.

Appendix B

Simulation Results of SLCM

B.1 Introduction

The simulation results of the Single Layer Cylindrical Model (SLCM) are detailed in this chapter. The impedances obtained from the Electric Field (EF) and the Electric and Magnetic Field (EMF) approaches of 54 SLCMs are listed and compared and the error analysis for the comparison is presented. These results are categorised and analysed in terms of impedances and resistive power dissipation.

B.2 Simulation Results from the EF approach

These results are obtained from the EF simulation approach, where magnetic fields are assumed to have negligible effects on the SLCM models.

B.2.1 Impedance

The tissue impedances obtained from the EF approach is represented in Equation (B.1), where Z_{ef} is the impedance magnitude determined from the resistance R_{ef} and reactance X_{ef}.

$$\begin{aligned} Z_{ef} &= R_{ef} + \mathrm{j}\ X_{ef} \\ |Z_{ef}| &= \sqrt{{R_{ef}}^2 + {X_{ef}}^2} \end{aligned} \tag{B.1}$$

Figures B.1 $\backsim$ B.5 show the $|Z_{ef}|$ of 54 tissues obtained from the EF simulations.

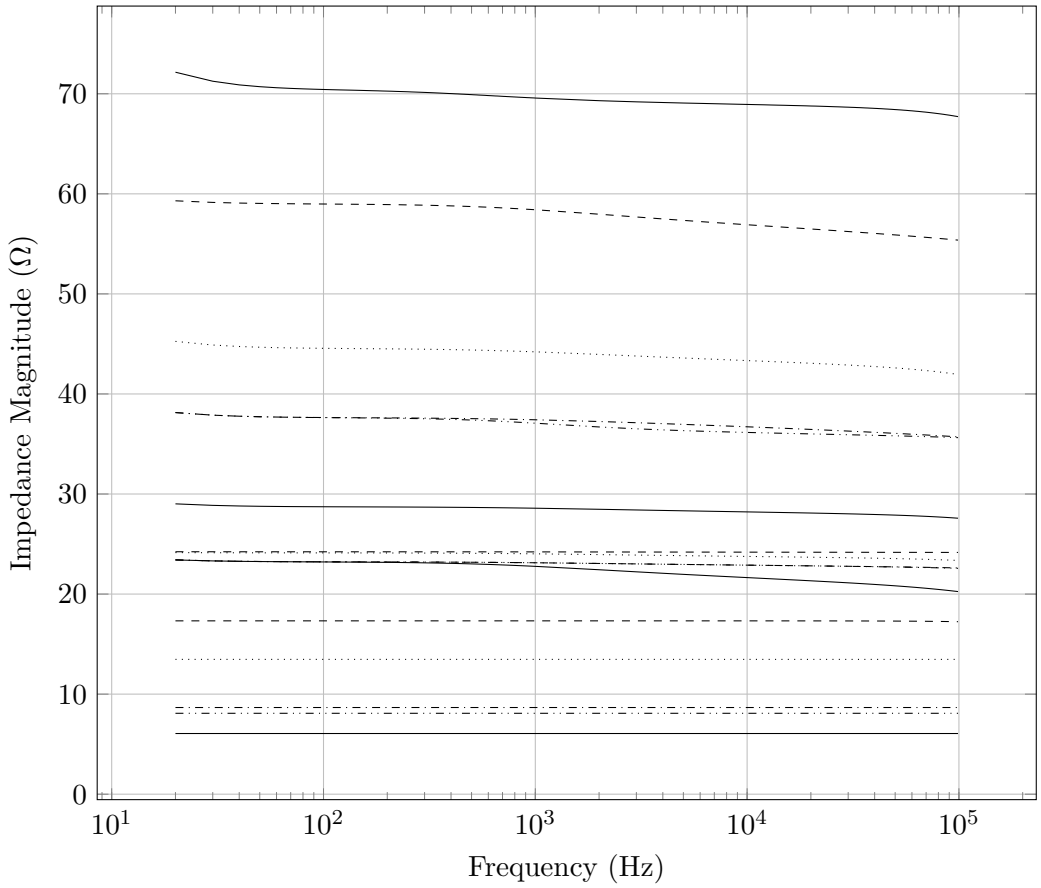

——	Cartilage
- - -	Bladder
.....	Tongue
-·-·-	Ovary
-·-·-	Lens
——	Prostate, Testis
- - -	Dura
.....	EyeSclera, Retina
-·-·-	Duodenum, Oesophagus, Stomach
-·-·-	Gland, Lymph, Pancreas, Thymus, Thyroid
——	SmallIntestine
- - -	Blood
.....	GallBladder
-·-·-	GallBladderBile
-·-·-	Vitreous Humour
——	CerebroSpinalFluid

Figure B.1: Tissues with starting $|Z_{ef}|$ less than $80\,\Omega$ and a standard deviation less than $2\,\Omega$. (Legend is arranged according to the graphs in descending order of impedance at 20 Hz)

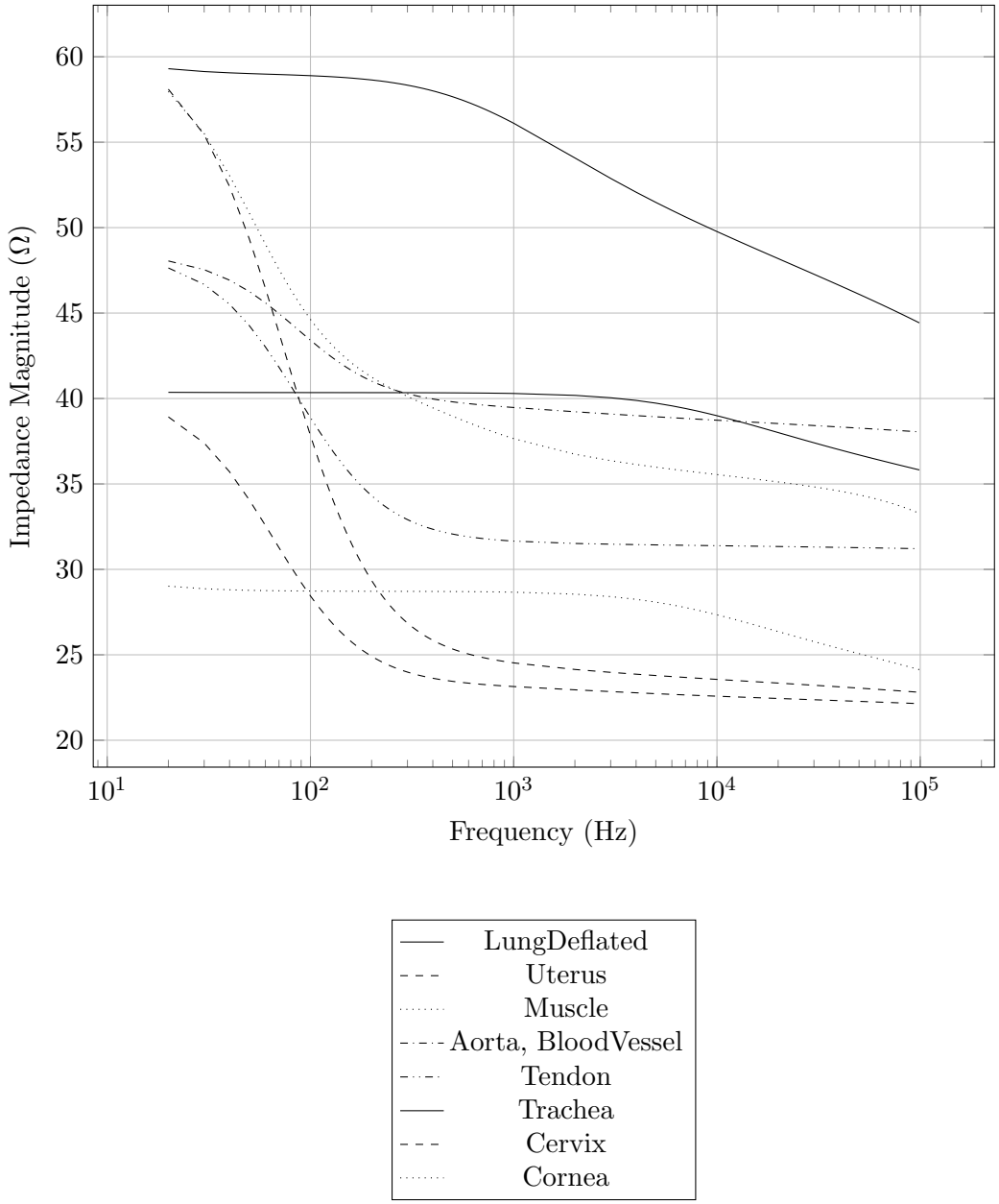

Figure B.2: Tissues with starting $|Z_{ef}|$ less than $80\,\Omega$ and a standard deviation more than $2\,\Omega$. (Legend is arranged according to the graphs in descending order of impedance at 20 Hz)

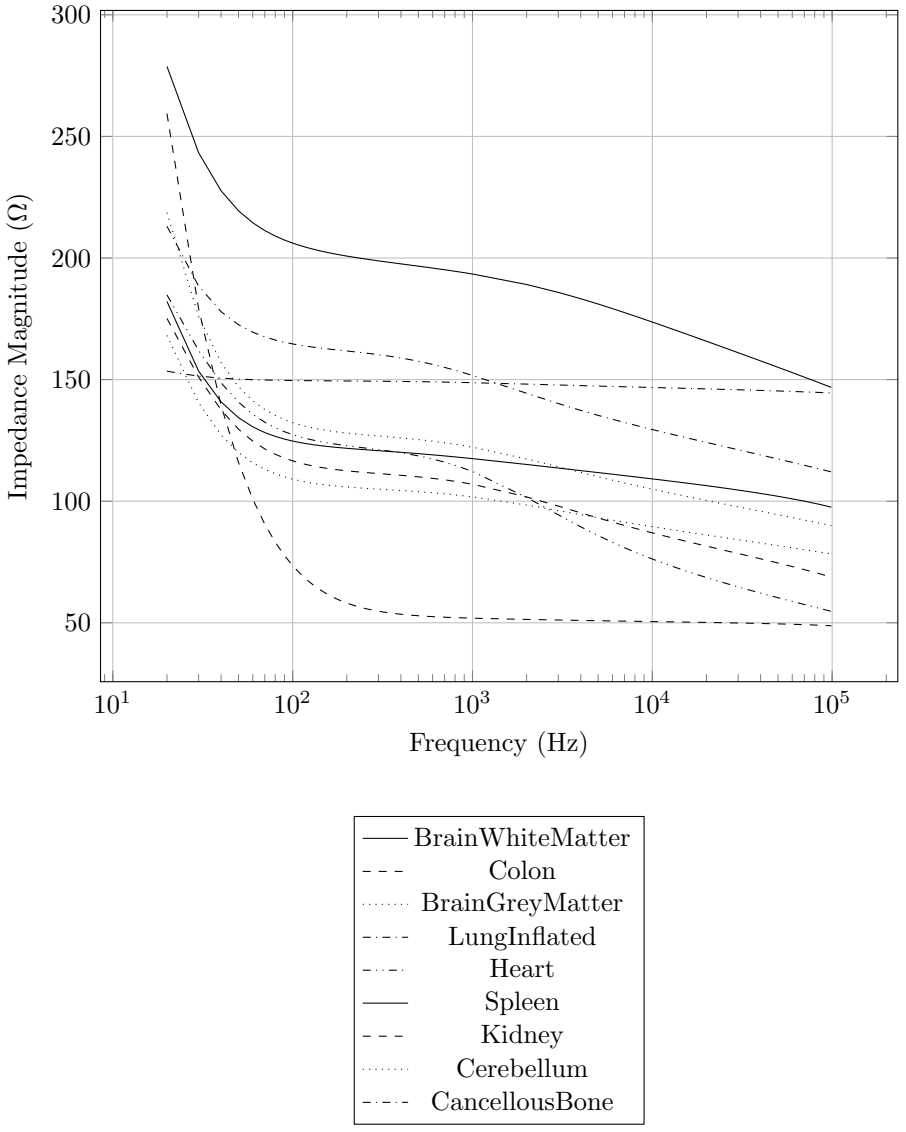

Figure B.3: Tissues with starting $|Z_{ef}|$ 150 $\backsim$ 300 Ω. (Legend is arranged according to the graphs in descending order of impedance at 20 Hz)

.

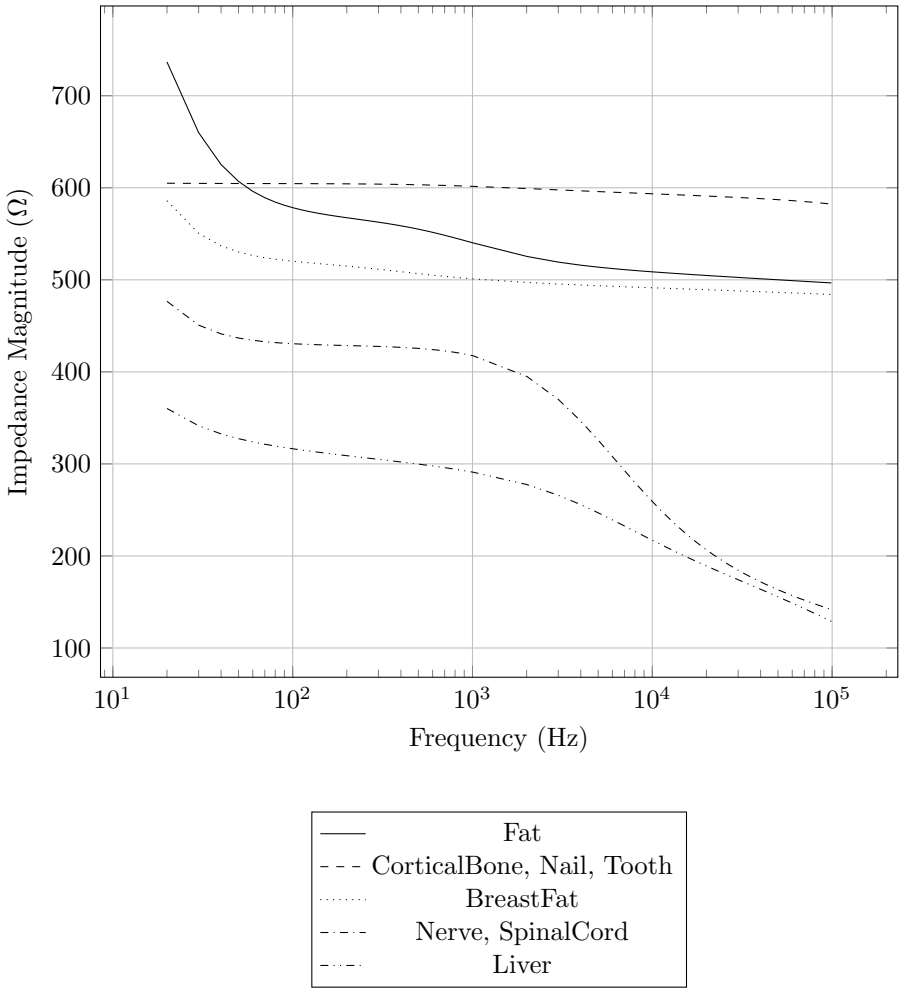

Figure B.4: Tissues with starting $|Z_{ef}|$ 300 $\backsim$ 800 Ω. (Legend is arranged according to the graphs in descending order of impedance at 20 Hz)

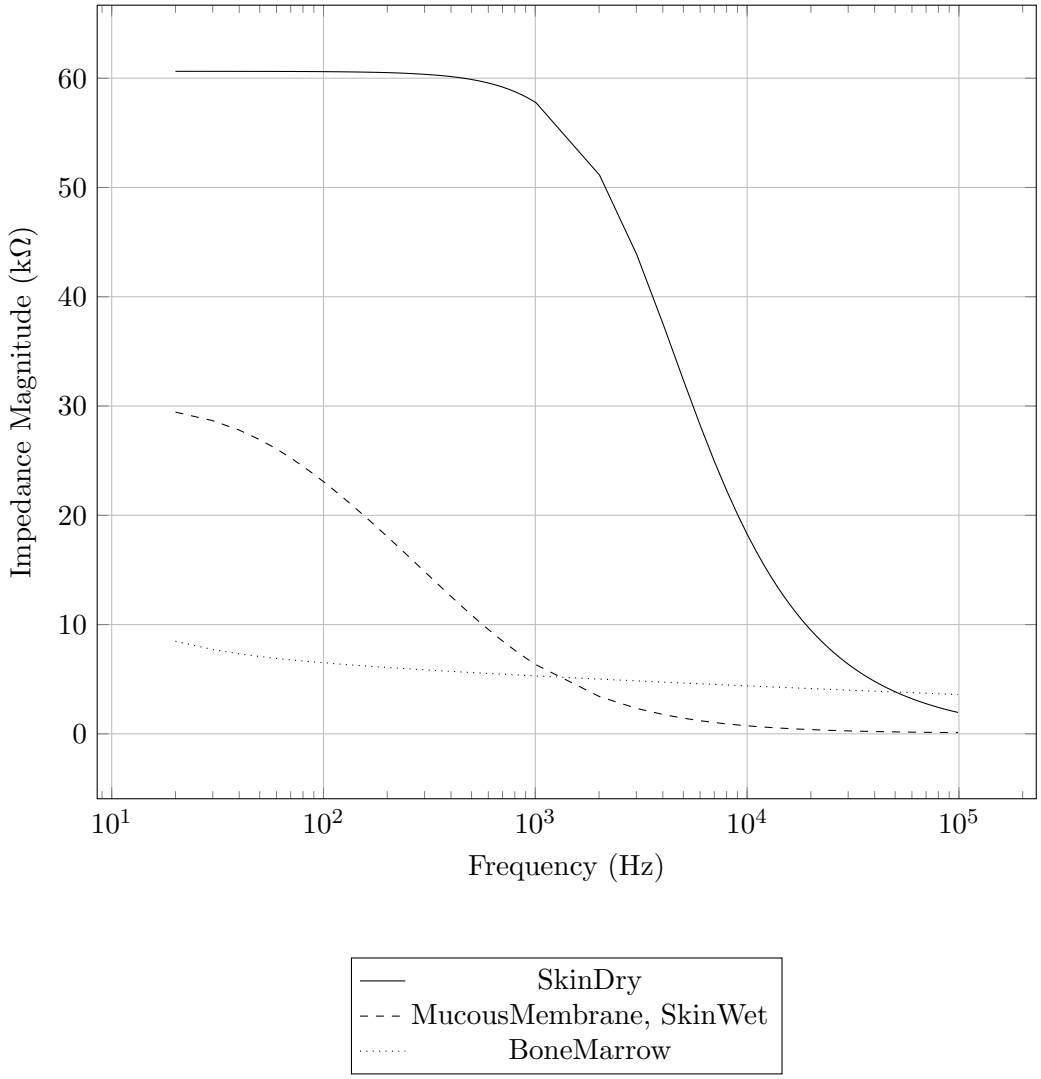

Figure B.5: Tissues with starting $|Z_{ef}|$ more than $800\,\Omega$. (Legend is arranged according to the graphs in descending order of impedance at 20 Hz)

Table B.1 ∽ B.5 show the standard deviations of the Z_{ef} of 54 tissues in the 20 Hz ∽ 100 kHz range. The tables are separated based on the categorisation of Figures B.1 ∼ B.5.

Table B.1: Mean Z_{ef} of tissues with $\sigma < 2$ and starting Z_{ef} less than 80 Ω

Tissue	Mean (Ω)	Real part *Std.Dev.* (Ω)	Imaginary part *Std.Dev.* (Ω)
Cartilage	69.16-1.91i	0.92	1.48
Bladder	57.38-0.97i	1.42	0.44
Tongue	43.5-1.36i	0.99	1.12
Ovary	36.85-0.59i	0.75	0.32
Lens	36.63-0.67i	0.79	0.22
Prostate; Testis	28.27-0.67i	0.43	0.6
Dura	24.2-0.03i	$2 \cdot 10^{-2}$	$3 \cdot 10^{-2}$
EyeSclera; Retina	23.81-0.39i	0.28	0.36
Duodenum; Oesophagus; Stomach	22.96-0.27i	0.24	0.18
Gland; Lymph; Pancreas; Thymus; Thyroid	22.95-0.3i	0.25	0.22
SmallIntestine	21.93-1.07i	1.15	0.75
Blood	17.31-0.18i	$3 \cdot 10^{-2}$	0.23
GallBladder	13.47-2.54e-3i	$7.62 \cdot 10^{-4}$	$2.82 \cdot 10^{-3}$
GallBladderBile	8.66-1.05e-3i	$2.48 \cdot 10^{-6}$	$1.33 \cdot 10^{-3}$
BodyFluid	8.08-0.75e-3i	$2.39 \cdot 10^{-6}$	$9.49 \cdot 10^{-4}$
CerebroSpinalFluid	6.06-0.47e-3i	$1.82 \cdot 10^{-6}$	$5.92 \cdot 10^{-4}$

Table B.2: Mean Z_{ef} of tissues with $\sigma > 2$ and Starting Z_{ef} less than 80 Ω

Tissue	Mean (Ω)	Real part *Std.Dev.* (Ω)	Imaginary part *Std.Dev.* (Ω)
LungDeflated	52.06-3.34i	5.77	1.08
Aorta; Bloodvessel	39.42-1.31i	1.67	1.03
Trachea	38.67-1.11i	1.85	0.95

Table B.2 – continued from previous page

Muscle	37.12-3.63i	3.75	1.75
Tendon	32.29-1.83i	2.51	2.19
Cornea	27.01-1.3i	1.89	1.09
Uterus	25.17-3.57i	4.73	4.17
Cervix	23.35-1.68i	2.22	1.94

Table B.3: Mean Z_{ef} of tissues with Starting Z_{ef} $150 \backsim 300\,\Omega$

Tissue	Mean (Ω)	Real part *Std.Dev.* (Ω)	Imaginary part *Std.Dev.* (Ω)
BrainWhiteMatter	177.46-18.84i	22.39	11.6
CancellousBone	147.36-2.23i	2	1.23
LungInflated	138.22-15.27i	20.6	7.03
Spleen	111.16-12.4i	10.2	9.13
BrainGreyMatter	110.69-14.47i	16.16	12.98
Cerebellum	93.63-10.38i	12.1	7.93
Kidney	93.09-14.11i	19.27	6.38
Heart	90.24-17.23i	29.89	5.7
Colon	51.35-11.97i	4.5	24.98

Table B.4: Mean Z_{ef} of tissues with Starting Z_{ef} $300 \backsim 800\,\Omega$

Tissue	Mean (Ω)	Real part *Std.Dev.* (Ω)	Imaginary part *Std.Dev.* (Ω)
CorticalBone; Nail; Tooth	595.28-11.83i	8.52	10.86
Fat	529.64-28.1i	31.51	28.18
BreastFat	497.99-15.31i	12.57	17.42
Nerve; SpinalCord	297.61-54.49i	131.29	22.77
Liver	227.86-44.29i	77.91	15.7

Table B.5: Mean Z_{ef} of tissues with Starting Z_{ef} more than $800\,\Omega$

Tissue	Mean (Ω)	Real part *Std.Dev.* (Ω)	Imaginary part *Std.Dev.* (Ω)
SkinDry	30714.73-7990.16i	28564.19	6014.29
BoneMarrow	4786.81-785.93i	989.91	324.85
MucousMembrane; SkinWet	4209.43-4640.7i	6269.09	4512.78

B.2.2 Resistive Power Dissipation

The resistive power dissipation P_{ef} are shown in Figures B.6 $\sim$ B.10. From the figures, the P_{ef} of various tissues correspond to the $|Z_{ef}|$ shown in Figures B.1 $\sim$ B.5. The results are as expected from P_d in Equation (A.23).

B.3 Simulation Results of the EMF approach

The results are obtained from the EMF simulation approach, where both the electric and magnetic fields effects are considered.

B.3.1 Impedance

The EMF simulation results are the same as the EF simulation results except for a few tissues due to the dielectric nature of human tissues. The maximum absolute error between the simulations are calculated for each tissue and shown in Table B.3.1. The absolute error is calculated using Equation (B.2). The maximum absolute error is calculated by finding the maximum value of the absolute errors.

$$\begin{aligned} error_Z &= |(Z_{mf} - Z_{ec})/Z_{mf}| \\ error_R &= |(R_{mf} - Rec)/R_{mf}| \\ errpr_X &= |(X_{mf} - X_{ec}/X_{mf})| \end{aligned} \tag{B.2}$$

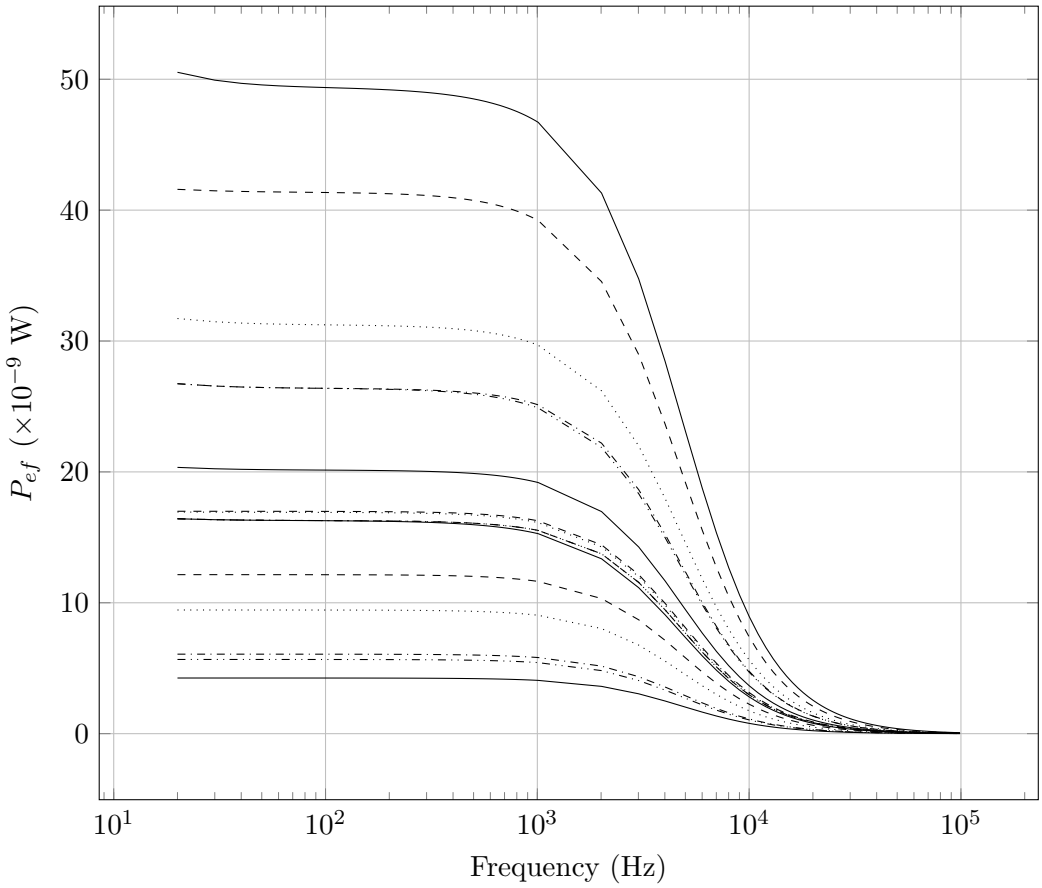

——	Cartilage
- - -	Bladder
·····	Tongue
-·-·-	Ovary
-·-·-	Lens
——	Prostate, Testis
- - -	Dura
·····	EyeSclera, Retina
-·-·-	Duodenum, Oesophagus, Stomach
-·-·-	Gland, Lymph, Pancreas, Thymus, Thyroid
——	SmallIntestine
- - -	Blood
·····	GallBladder
-·-·-	GallBladderBile
-·-·-	Vitreous Humour
——	CerebroSpinalFluid

Figure B.6: P_{ef} of tissues from Figure B.1. (Graphs are arranged according to the legend in descending order of power at 20 Hz)

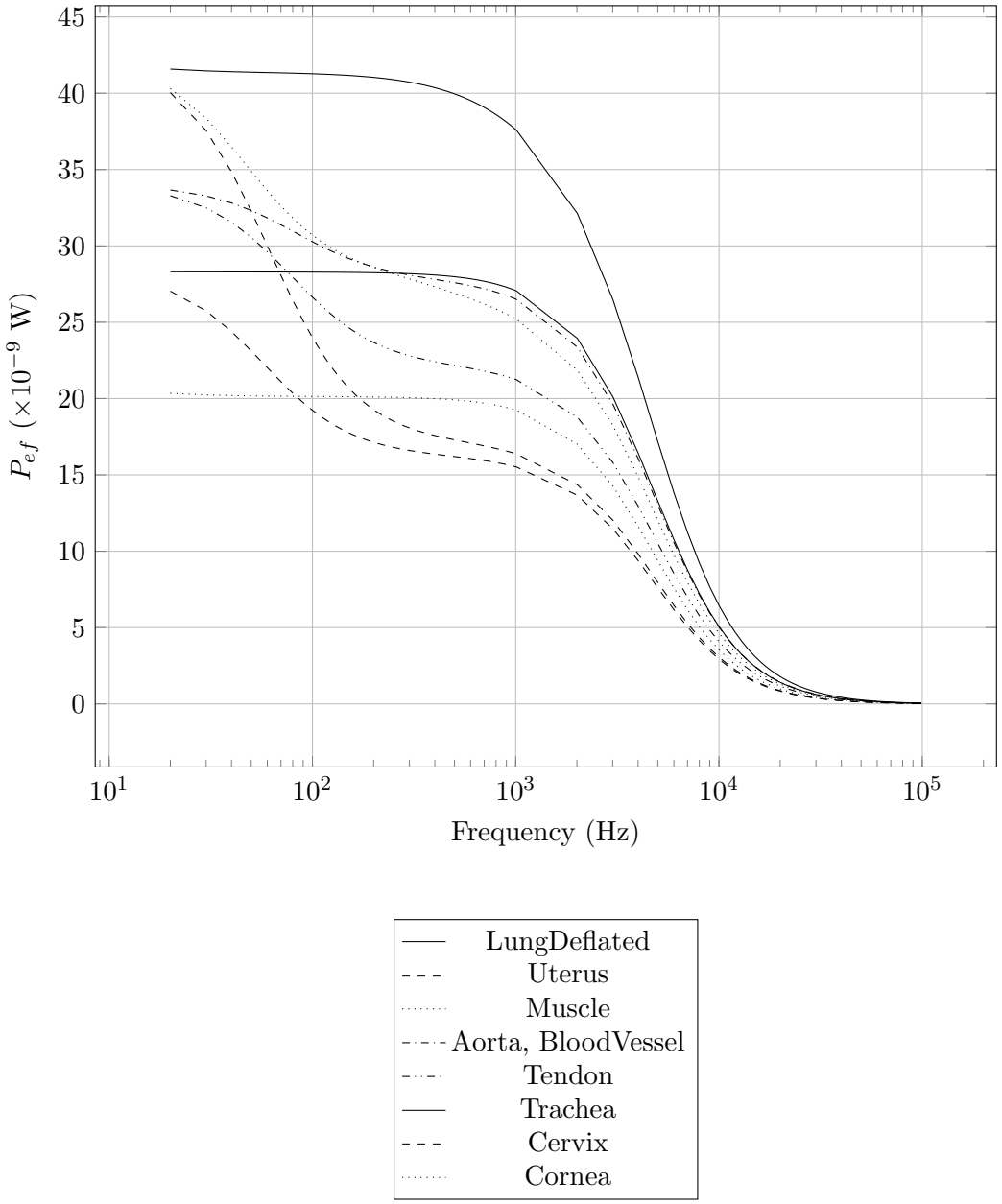

Figure B.7: P_{ef} of tissues from Figure B.2. (Graphs are arranged according to the legend in descending order of power at 20 Hz)

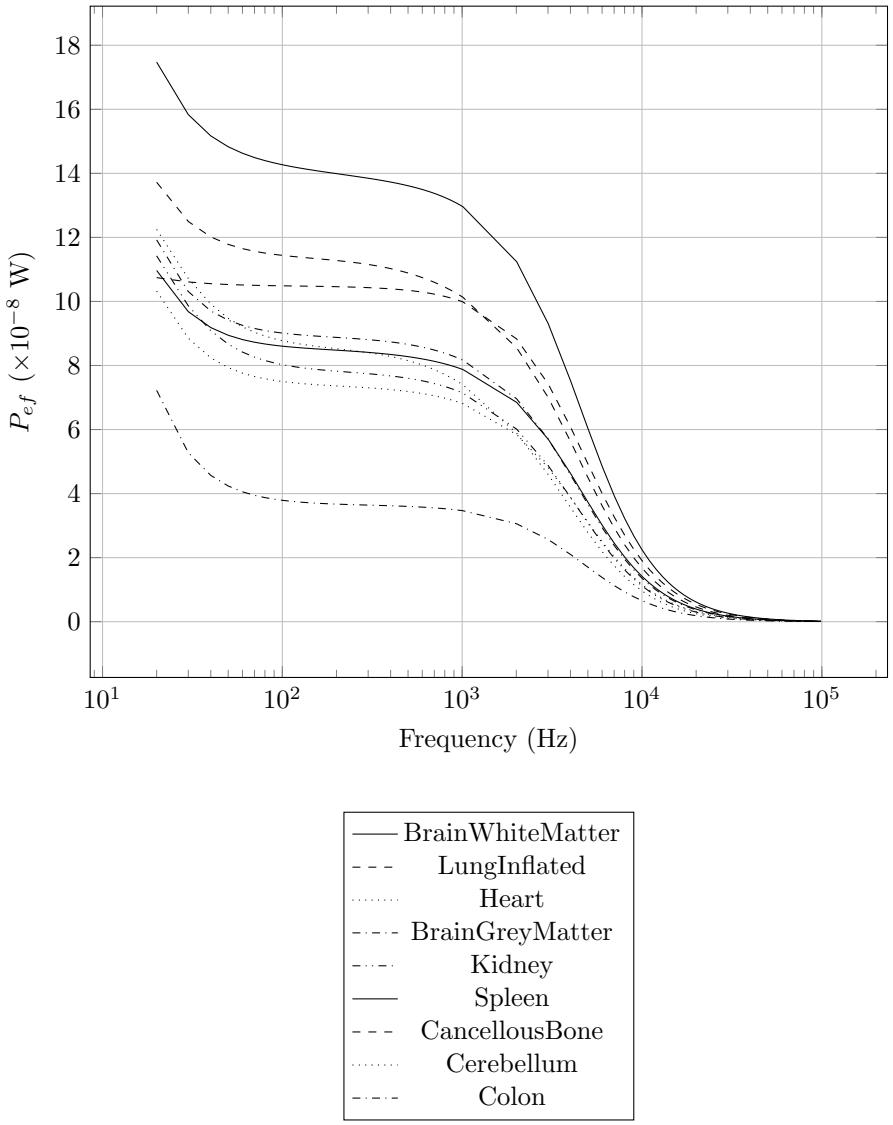

Figure B.8: P_{ef} of tissues from Figure B.3. (Graphs are arranged according to the legend in descending order of power at 20 Hz)

.

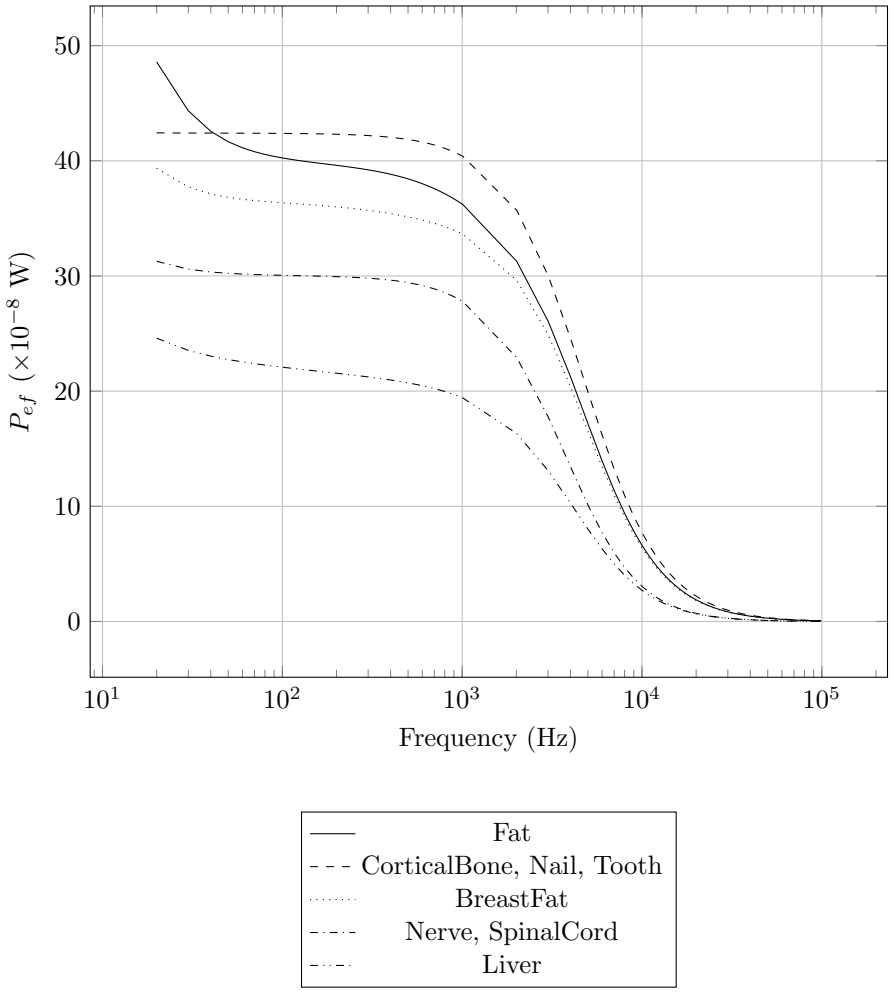

Figure B.9: P_{ef} of tissues from Figure B.4. (Graphs are arranged according to the legend in descending order of power at 20 Hz)

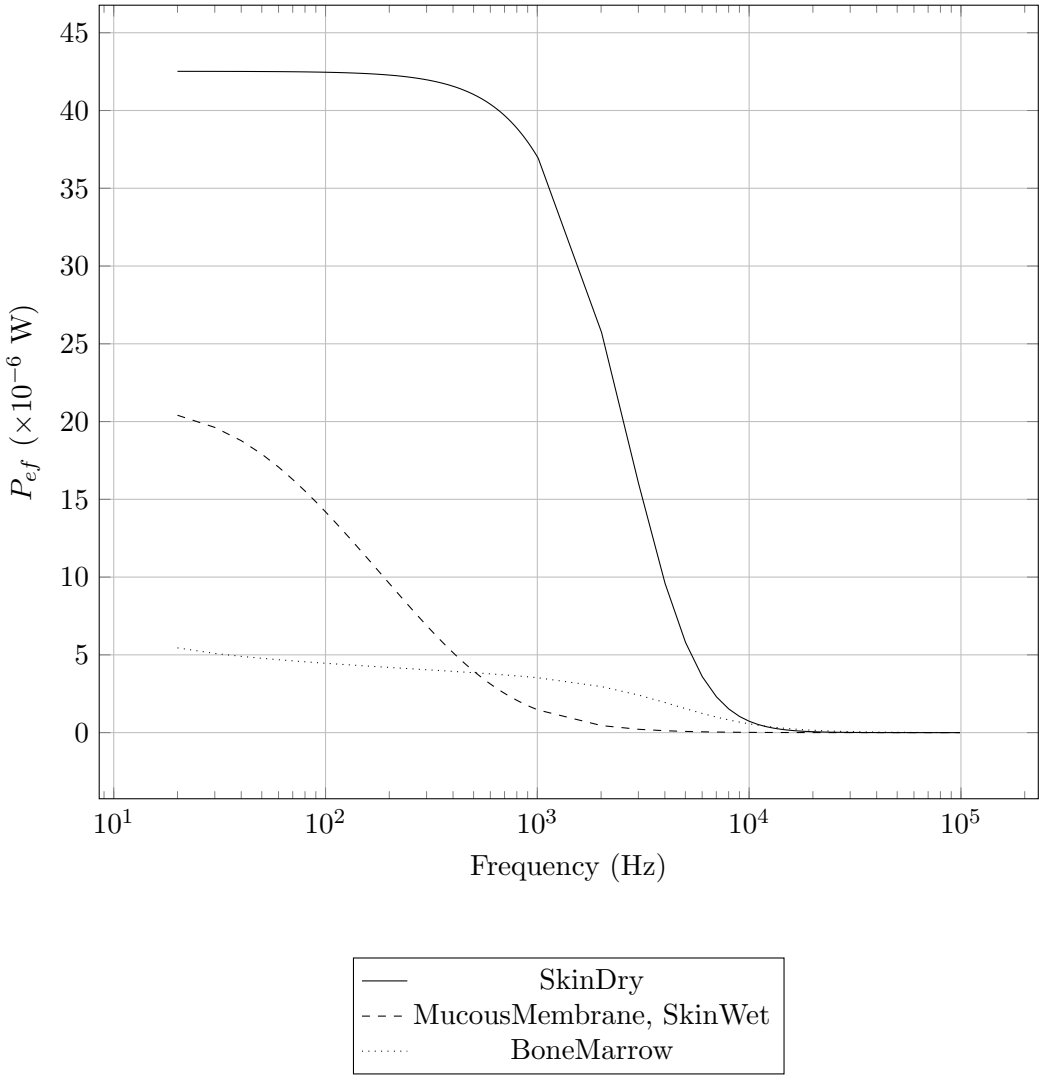

Figure B.10: P_{ef} of tissues from Figure B.5. (Graphs are arranged according to the legend in descending order of power at 20 Hz)

Table B.6: Comparison of $|Z_{ef}|$ between simulation results of EMF and EF approaches. The maximum absolute error is shown.

Tissue	Impedance Magnitude error ($\times 10^{-5}$)	Resistance error ($\times 10^{-5}$)	Reactance error ($\times 10^{-3}$)
Aorta	1.48	1.4	13.98
Bladder	1.08	1.06	5.33
Blood	2.14	0.44	16.89
BloodVessel	1.48	1.4	13.98
BodyFluid	0.46	0.47	1597.8
CancellousBone	3.46	3.39	3.62
CorticalBone	1.03	2.46	4.04
BoneMarrow	25.87	52.02	7.33
BrainGreyMatter	4.12	4.25	0.93
BrainWhiteMatter	2.7	2.74	0.78
BreastFat	1.21	1.21	13.36
Cartilage	1.14	0.94	1.82
Cerebellum	4.91	5	1.05
CerebroSpinalFluid	0.43	0.46	1302.1
Cervix	2.39	2.23	21.09
Colon	4.6	3.01	2.2
Cornea	4.13	1.9	2.91
Duodenum	2.31	2.37	12.35
Dura	2.05	2.04	103.53
EyeSclera	2.28	2.28	6.96
Fat	1.12	1.12	10.1
GallBladder	3.74	3.74	8673.6
GallBladderBile	0.47	0.47	2079.5
Gland	2.31	2.33	10.73
Heart	4.53	4.51	0.67
Kidney	4.85	4.78	0.58
Lens	1.53	1.55	7.1
Liver	1.84	4.31	0.21
LungDeflated	2.13	1.08	1.88
LungInflated	3.34	3.42	0.86
Lymph	2.31	2.33	10.73
MucousMembrane	4.69	6.91	$7.57 \cdot 10^{-2}$
Muscle	3.23	1.49	2.05
Nail	1.03	2.46	4.04

Table B.6 – continued from previous page

Nerve	1.36	3.54	0.3
Oesophagus	2.31	2.37	12.35
Ovary	1.49	1.46	7.51
Pancreas	2.31	2.33	10.73
Prostate	2.32	1.81	4.18
Retina	2.28	2.28	6.96
SkinDry	77.03	155.01	0.79
SkinWet	4.69	6.91	$7.57 \cdot 10^{-2}$
SmallIntestine	5.28	2.36	3.14
SpinalCord	1.36	3.54	0.3
Spleen	4.33	4.33	0.63
Stomach	2.31	2.37	12.35
Tendon	1.67	1.74	41.04
Testis	2.32	1.81	4.18
Thymus	2.31	2.33	10.73
Thyroid	2.31	2.33	10.73
Tongue	1.94	1.34	2.27
Tooth	1.03	2.46	4.04
Trachea	1.72	1.4	3.86
Uterus	2.16	2.23	10.12

From Table B.3.1, it can be seen that all tissues have $error_R \approx 10^{-5}$. The reactance plays a more significant role since $error_X \approx 10^{-3}$. $X_{mf} << R_{mf}$ for all tissues as seen in Tables B.1 $\sim$ B.5, hence $error_Z \approx 10^{-5}$ for all tissues. The tissues that have $error_X > 0.1$ are shown in Table B.7.

Table B.7: Tissues with $error_X > 0.1$

Tissue	$error_X$
Vitreous Humour	1.6
Cerebrospinal Fluid	1.3
Gall Bladder	8.67
Gall Bladder Bile	2.08

B.3.2 Resistive Power Dissipation

The resistive power dissipation of the EMF approach is the same as Figure B.6 $\sim$ B.10 since $error_Z < 10^{-4}$, therefore not presented in this work.

B.4 Conclusion

The SLCM tissue impedances obtained from both the EF and EMF simulation approaches are presented. Z_{ef} and Z_{emf} are compared and an error analysis is conducted. It is found that $error_Z < 10^{-4}$ for all tissues. Tissues with $error_X > 0.1$ and show inductive reactances are: vitreous humour, cerebrospinal fluid, gall bladder and gall bladder bile. X_{ef} and X_{emf} for other tissues display capacitive behaviour.

Appendix C

Image segmentation of the Male Right Leg

C.1 Introduction

This appendix serves as a reference to the image segmentation techniques implemented to model the human leg using Multi-layered Cylindrical Model (MLCM). The image segmentation is performed on data provided by the Visible Human Project ® (VHP) [75] and BodyParts3D (BP3D) [74]. This data includes MRI images and established voxel models of the human right leg. The tissues that are segmented include: bone marrow, bone, muscle, blood vessel and fat.

C.2 Segmentation of models obtained from BP3D

Three tissue voxel models of the human leg are obtained from BP3D [74]: blood vessels, bone, and muscle. BP3D does not supply the fat and bone marrow voxel models. Only the surface meshes of the voxel models are available from which the tissue geometries are obtained. The blood vessels voxel model include all main arteries of the leg as shown in Figure C.1a. The voxel model of the veins of the human leg is unavailable and not considered. The bone voxel model includes all the bones of the human leg as shown in Figure C.1b. Figure C.1c shows the muscle voxel model and includes all the muscles of the human leg. A mesh processing software, MeshLab [82], is utilised to simplify, repair and calculate the volumetric meshes of the voxel models. The calculated tissue volumes are presented in Table C.1.

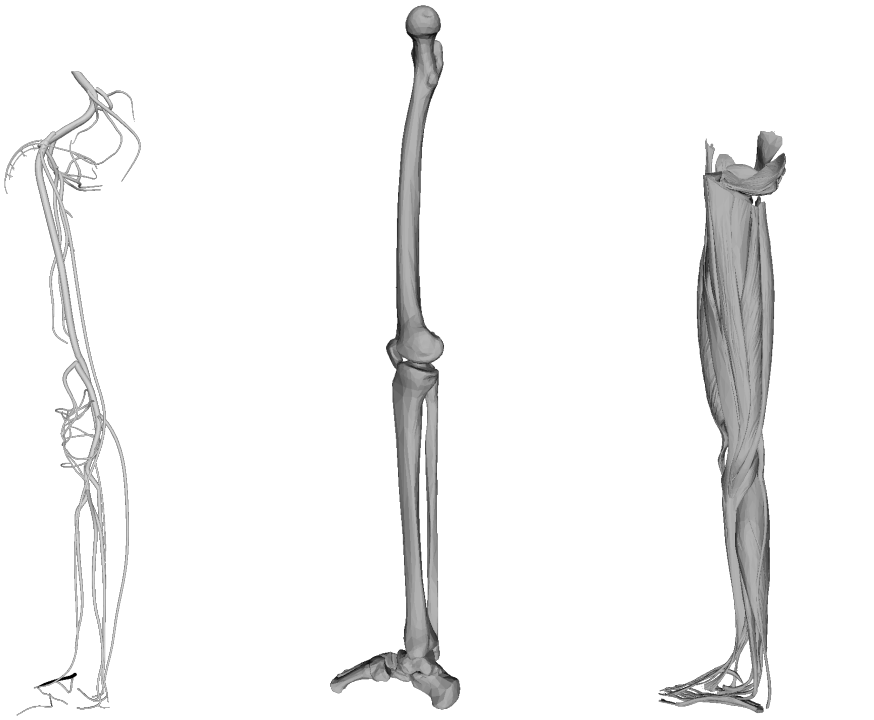

(a) Blood Vessels (b) Bones (c) Muscles

Figure C.1: Tissues of the human right leg from BP3D

Table C.1: Volumes of tissues obtained from BP3D

Tissue	**Volume** ($\times 10^6$ **mm**^{3})
Bone	1.01
Muscle	3.67
Blood Vessels	0.13

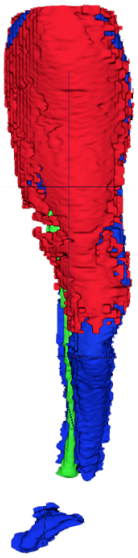

Figure C.2: Muscles, fat and bone marrow of the human right leg

Table C.2: Volumes of tissues obtained from the VHP

Tissue	**Volume** ($\times 10^6$ **mm**^{3})
Fat	2.91
Muscle	4.92
Bone Marrow	0.42

C.3 Segmentation of images obtained from the VHP

Three tissues of the human leg are segmented from the MRI scans provided by the VHP [75]: bone marrow, muscle and fat. The bones and the blood vessels are not segmented due to low resolutions of the images. A medical image segmentation tool, ITK-Snap [3], is utilised to condition and segment the MRI images to obtain the tissue volumes. Since the resolution of the images is low, the segmentation results are coarse with low accuracy. The segmented 3D voxel model is depicted in Figure C.2 and the tissue volumes are shown in Table C.2.

C.4 Combination of Tissue Volumes from VHP and BP3D

The image data used to calculate the tissue volumes are from two different sources. This results in discrepancy of various tissue volumes as the models and images are not based on the same human leg. However, since both sources have the volumetric data of muscle, other tissues are scaled according to the difference in muscle volume. The data from the two sources are combined to yield a complete tissue model.

Table C.3: Final volumes of all five tissues of the human leg

Tissue	**Volume** ($\times 10^6$ **mm**^{3})
Bone Marrow	0.31
Cortical Bone	0.7
Muscle	3.67
Blood	0.22
Fat	2.17

Muscle volume obtained from the VHP shown in Table C.2 is 1.34 times more than the muscle obtained from the BP3D shown in Table C.1. All tissues from the VHP are scaled accordingly by a factor of 1.34.

The volume of bone calculated in Section C.2 is the total bone volume of the right leg. The bone marrow volume in Section C.3 is subtracted from the total bone volume in order to obtain the volume of cortical bone (cancellous bone is ignored in this work).

The total blood vessel volume is used to calculate the total blood volume. For muscular artery, the vessel wall thickness is approximately $\frac{1}{6}$ of the diameter of the artery [92]. Assuming that all blood vessels in the voxel model are muscular arteries, the total volume of blood contained in the arteries is $\frac{5}{6}$ of the total blood vessel volume. Since the voxel model of veins in the leg is unavailable, the volume of blood in veins is assumed to be identical to the volume of blood in the arteries. Therefore, the blood volume is doubled to account for blood in the veins.

The final volumes of the tissues are shown in Table C.3.

C.5 Conclusion

Tissue volumes of five tissues of the human leg are obtained from image segmentation of two sources: VHP and BP3D. These tissues are: bone marrow, bone, blood vessel, muscle and fat. From these tissues, assumptions and approximations are carried out to yield the final volumes of: bone marrow, cortical bone, blood, muscle and fat.

Appendix D

Lightning Injury Analysis using SLCM

D.1 Preface

This appendix is a conference paper that was accepted and presented at the *International Conference on Lightning Protection (ICLP)* held in Shanghai, China in October 2014. The paper is titled: **Use of dielectric properties in the analysis of lightning injuries**.

D.2 Overview

This paper discusses the use of dielectric properties in simulation to determine the tissue impedances and tissue power dissipation. The DEF is used to model the FSS with frequency components up to 100 kHz. Nineteen human tissues are modelled as SLCMs and simulated using the EMF approach in COMSOL.

The tissue impedances are correlated with lightning injuries and the results show that the use of dielectric properties in lightning injury analysis is viable.

2014 International Conference on Lightning Protection (ICLP), Shanghai, China

Use of dielectric properties of human tissues in the analysis of lightning injuries

Y-C. H. Lee, D. M. Rubin and I. R. Jandrell
School of Electrical & Information Engineering,
University of the Witwatersrand, Johannesburg,
Private Bag 3, Wits 2050,
Johannesburg, South Africa

***Abstract*—This paper focuses on the use of dielectric properties of human tissues in analysing injuries as a result of the lighting short stroke current. The lightning short stroke current is decomposed into its frequency components and the effects of these frequency components on human tissues are analysed. The dielectric properties of nineteen types of human body tissues are examined and the correlations between the impedances of these tissues and the lightning stroke current pathway are investigated. The human tissues are modelled as cylindrical structures using a FEA (Finite Element Analysis) approach and simulated using the COMSOL Multiphysics software suite. The results obtained from the simulations include: current density, complex impedance and total absorbed power of the tissues. Only the first short stroke of the lightning flash is considered as the test parameter. The direct strike mechanism of lightning injury is examined in this paper with the possibility of including other mechanisms of lightning injury in the future. The first short stroke of the lightning flash is modelled using a double exponential model and exhibit a 4 kA $1.8/30\mu$s waveform. This waveform consists of frequencies up to 100 kHz. The skin and bone marrow is found to have the most varying impedances within this frequency range and the heart is found to be the organ with the least impedance. The results from the simulations depict physical properties of real human tissues and hence are valid in the analyses of lightning injuries.**

***Keywords*—COMSOL; Dielectric properties; Lightning impulse waveform; Lightning effects; Lightning injuries**

I. INTRODUCTION

Lightning current waveforms can be described by its similarity to impulse waveforms and hence several standards require high voltage impulse testing as test parameters [1–3]. The resemblance of lightning current waveforms to impulse waveforms is equally significant in the analysis of human lightning injuries. Grounding of structures are commonly designed for power frequencies as the human body is more susceptible to $50/60\ Hz$ current than high frequency currents [4]. However, lightning injuries still occur and hence the research into the frequency components of the lightning strokes is necessary. The use of dielectric properties of human tissues in analysing lightning injuries as a result of the lighting stroke current is the main focus of this paper. The dielectric properties of various human tissues are examined, and the correlations between the tissue dielectric properties and the lightning stroke current pathway are investigated. Only the first short stroke of the lightning flash and the direct strike lightning injury mechanism are considered. The effects of other components of the lightning flash and other lightning injury mechanisms can be analysed using the same approach described in this paper.

In order to investigate the effects of lightning short stroke current through the body, two principal aspects are surveyed: the lightning first stroke current waveform and the dielectric properties of human tissues. Since the lightning stroke current exhibits the properties of impulse waveforms, frequency components of the lightning stroke current need to be examined. The double-exponential expression model of the lightning current waveform proposed by Wang and Zhang [5] is used in this paper due to its effective yet uncomplicated approach. It is simpler to transform a double-exponential function into the frequency domain than using the more common Heidler function model such as proposed by Vujević and Lovrić [6].

The dielectric properties of human tissues are obtained from the Italian Research Council - Institute for Applied Physics [7]. The dielectric properties of the provided human tissues include effective conductivity, relative permittivity and loss tangent. These are used to define the material properties of the tissues from the electrical perspective.

A finite element analysis (FEA) approach is adopted in this paper with the use of the COMSOL Multiphysics software suite as the simulation platform. Cylindrical models of various human tissues are constructed in COMSOL Multiphysics. The model of the lightning current waveform is applied to the various human tissue models and the results are analysed and correlated with lightning injuries.

II. BACKGROUND

The extent of lightning injuries is dependent on the current discharge pathway through the human body when struck by lightning [8]. Hence, it is crucial to analyse the critical biological structures that are affected along this pathway. The clinical symptoms of lightning injuries can be classified into three major categories namely: neurological injuries, cardiac injuries and external burns [9].

Rakov and Uman [10] describes the possibility that a direct strike to a human body results in a flash over, which decreases the peak current and voltage of the lightning stroke at the attachment point. They further describe that the arc of the flash over results in a decrease of the electric field to $2kVm^{-1}$ and ultimately reduces the current flowing through the body to $5\ A$. However, this is applicable only if the human body is considered to be purely resistive. When analysing from the frequency perspective, the human body may exhibit inductive and capacitive properties which results in the change of the total impedance of the human body.

A. Lightning short stroke current waveform

The lightning short stroke waveform is described by the IEC-62305-1 [1] as shown in Equation (1). It is difficult to obtain the frequency components of this equation as complex mathematical procedures are required to transform the equation into the frequency domain [11]. A simpler version of the lightning short stroke waveform that is commonly used is the double exponential function shown in Equation (2). The disadvantage for using the double exponential function is due to its unrealistic instantaneous rise at time 0 [10]. Equation (2) is used as a proof of concept in this paper albeit less accurate than Equation (1) or the Heidler function [12].

$$i(t) = \frac{I}{k} \cdot \frac{(t/\tau_1)^{10}}{1 + (t/\tau_1)^{10}} \cdot e^{(-t/\tau_2)} \tag{1}$$

$$i(t) = I(e^{-\alpha t} - e^{-\beta t}) \tag{2}$$

B. Dielectric properties of human tissues

The Italian Research Council - Institute for Applied Physics devised parametric models for the dielectric properties of human tissues [7]. Fifty six human tissues are available, however, only nineteen tissues are examined in this paper. Several tissues are disregarded as these are less significant in the analysis of lightning injuries. The dielectric properties given for each tissue include: effective conductivity, relative permittivity and loss tangent. These material properties are frequency dependant and therefore present different characteristics at various frequencies. These parameters are required to define the electrical properties of human tissues.

C. Human models in FEA

From literature, the human body is typically modelled as cylindrical structures when using the FEA approach. Ruan et al. [13] analysed the electrical properties of human tissues and organs by using a cylindrical model of the human body. Werner and Webb [14] used a six-cylinder model of the human body in the study of human thermoregulation. Muramatsu et al. [15] calculated the impedance of the human arm in human body communication by developing a multilayered cylindrical model of the human arm.

III. Lightning short stroke current waveform

The first negative short stroke current waveform parameters are taken from IEC-62305-1 [1] as a $1.8/30\ \mu s$ waveform with a peak value of $4\ kA$. These values are chosen as they lie in the 95% probability range. The double exponential function waveform which satisfies these parameters is shown in Fig. 1.

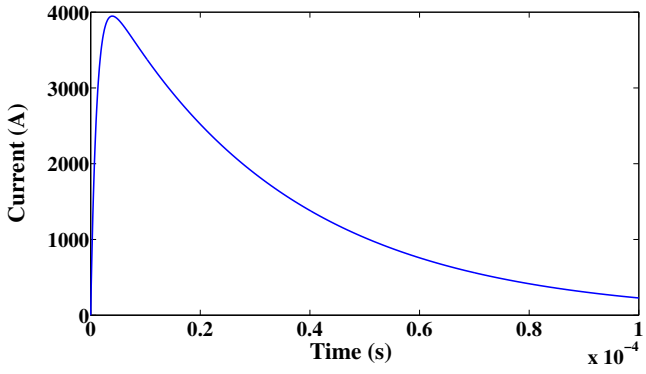

Fig. 1: Double exponential function

A. Frequency components of the lightning short stroke

The frequency components of the double exponential short stroke model in Fig. 1 is calculated by the use of the Fourier transform and shown in Equation (3). Expanding Equation (3) and separating the equation into its real and imaginary components yields Equation (4).

$$i(jw) = I(\frac{1}{\alpha + jw} - \frac{1}{\beta + jw}) \tag{3}$$

$$i(jw) = I(\frac{\alpha}{\alpha^2 + w^2} - \frac{\beta}{\beta^2 + w^2} + j(\frac{-w}{\alpha^2 + w^2} + \frac{w}{\beta^2 + w^2})) \tag{4}$$

The magnitude of the current waveform at each frequency can thus be calculated using Equation (5) and plotted in Fig. 2.

$$\begin{aligned} |i(jw)| &= I\sqrt{\text{Re}(i(t))^2 + \text{Im}(i(t))^2} \\ &= I\sqrt{\frac{(\alpha - \beta)^2}{(\alpha^2 + w^2)(\beta^2 + w^2)}} \end{aligned} \tag{5}$$

The double exponential function model has a frequency range below $100\ kHz$ as shown in Fig. 2. This concurs with the findings of Wei et al. [11]. For the purpose of this paper, the double exponential model is sufficient in the analysis of the dielectric properties of the human tissues. Real lightning

short stroke current waveforms can be applied to the model in the future for more accurate results.

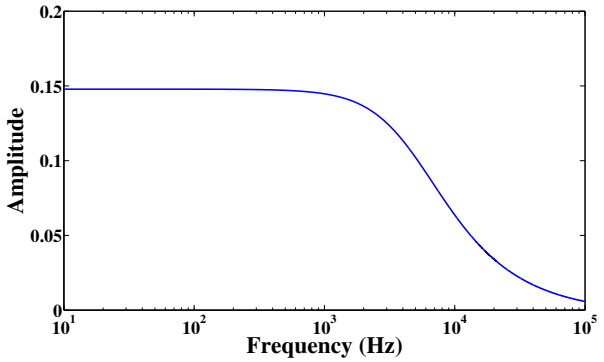

Fig. 2: Double exponential function in the frequency domain

IV. Simulated Model

COMSOL Multiphysics is used for the simulation and construction of the human tissue model. The frequency components of the lightning impulse waveform are analysed separately. Coronal discharge and breakdown voltages are not simulated as the lightning short stroke is assumed to have already attached to the human body. Side flashes are assumed to have taken place and hence not considered in the model.

A. Model Construction

1) Initial model: The various human body tissues are initially modelled individually as cylindrical structures. Each model is subjected to two contact points which are plates each attaching to leads representing the lightning attachment point and ground. The contact points and the model are connected uniformly with no air gaps. This model consequently resembles a capacitor as shown in Fig. 3. A region of surrounding air is further implemented to account for the electric and magnetic fields developed around the tissue.

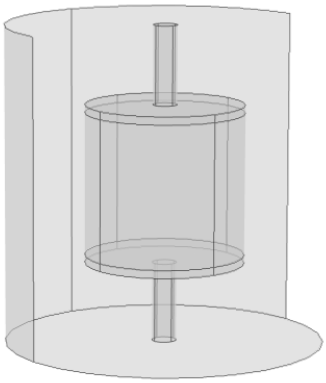

Fig. 3: Initial Tissue model

2) Simplified model: After simulations of the initial model, it is noted that the model introduces additional mesh points to the geometry around the contact plates and the leads which drastically increases simulation time. The model is simplified by removing the contact plates and the leads to represent a cylinder surrounded by air as shown in Fig. 4. The current is injected into the model from the top end of the cylinder and a ground plate is placed at the bottom end of the cylinder. The cylinder is of a homogeneous medium and assumes uniform distribution of voltage and current in a vertically downwards propagation.

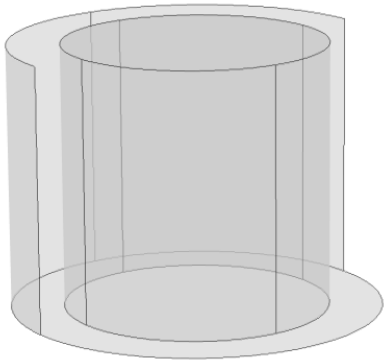

Fig. 4: Simplified tissue model

The liver is the largest organ in the human body with a mean length of $10.5\ cm$ [16]. Hence, all the human tissues are modelled according to this size for the ease of comparison. The cylindrical model thus is constructed with a diameter and height of $10\ cm$. Nineteen models are constructed each consisting of one type of human tissue and analysed individually. Since alternating current (AC) waveforms are used, magnetic fields and its induced currents are simulated in the model.

The size of the mesh is chosen such that it is uniform across the entire model, this is done by setting the maximum element size to be $1.4\ cm$ and the minimum element size to be $0.25\ cm$. Since the electric fields, magnetic fields and induced currents are significant in the model, the *Magnetic Fields* module in COMSOL Multiphysics is used for simulation in the frequency domain.

V. Results and Analysis

The developed model adopts a signal analysis approach whereby each frequency is analysed individually irrespective of the other frequencies. The modelling of each tissue may not be a good representation of real life tissues; such as modelling the skin as a cylinder. However, this is done such that the comparison of the dielectric properties between tissues can be carried out. The important results from the model are: tissue impedance, current density and power absorbed. The impedances of the tissues are used to analyse the current pathway of the lightning short stroke current through the

human body. The severity of the lightning injury to the tissue is indicated by the power absorbed.

A. Current density

The current through the cylinder is obtained from the surface integration of the current density over the cross section of the cylinder. Since the model is a homogeneous medium, the current density is uniform throughout the model and hence the current waveform for all tissues conform with Fig. 2. This result is as expected considering the current that is injected into the model and forced to flow within the cylinder is the current calculated using Equation (5). The electric field fringing effects in the air around the contact points are not considered and therefore do not contribute to the total current density of the model.

B. Impedance

The complex impedance of the model is obtained from the inverse of the admittance measured across the top and bottom end of the cylinder. From the imaginary part of the complex impedance, the inductive and capacitive properties of the tissue model are derived. The total impedance of the model is obtained by calculating the magnitude of the complex impedance. The simulation results of the impedances of various tissues at various frequencies are shown in Fig. 5-8. The impedance of each tissue is used only for comparison and do not describe the actual impedance of the tissue or organ.

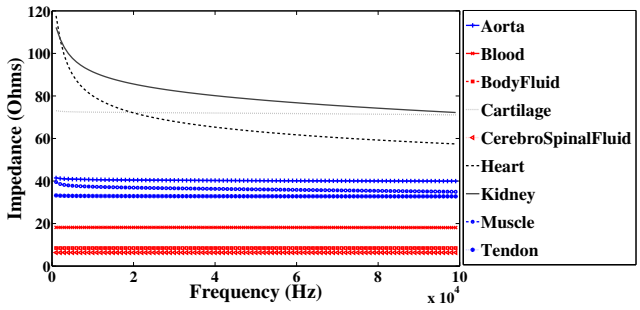

Fig. 5: Frequency vs Impedance of tissues which have average impedances less than 100 Ω

1) Tissues with average impedance less than 100 Ω*:* This section refers to Fig. 5. Aqueous tissues (blood, body fluid and cerebrospinal fluid) show little or no change in impedance over the entire frequency range. This is due to the mobility of hydrated ions which results in constant tissue conductivity and permittivity for all frequencies [17] and contributes to the low overall impedance. Connective tissues except for bones, fat and bone marrow (cartilage, muscle and tendon) have fairly low and constant impedances. The electrical conductive fibres within the cardiac muscle may attribute to the low impedance of the heart as these conductive fibres allow current pathways to be established. The low impedance of the kidney may be a result of high concentrations of ions such as sodium and potassium within the tissue [18] which increases electrical conduction.

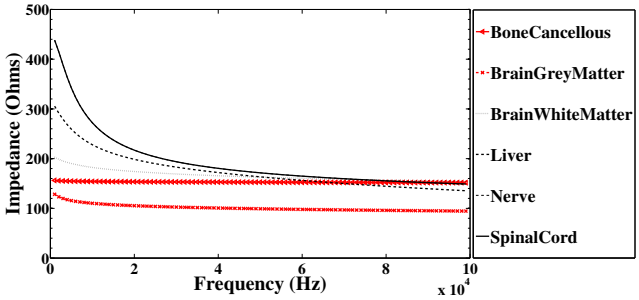

Fig. 6: Frequency vs Impedance of tissues which have average impedances 100 ∼ 200 Ω

2) Tissues with average impedance between 100 Ω *and* 200 Ω*:* This section refers to Fig. 6. The spinal cord and nerve tissues are inherently composed of the same biological materials and hence exhibit identical impedances for all frequencies. The grey matter of the brain consists of mainly cell bodies and hence have a lower impedance than the white matter of the brain which mainly consists of lipid tissue. This result coincides with the findings of Latikka et al. [19]. Both grey and white matter show identical graph shapes which indicates that a scaling factor is the only difference between the impedances of the two tissues. The cancellous bone is highly vascular and filled with fluids which results in the constant impedance for all frequencies.

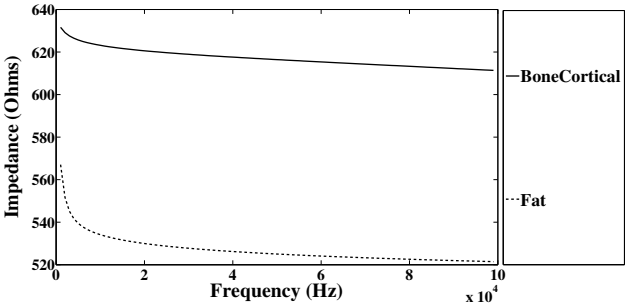

Fig. 7: Frequency vs Impedance of tissues which have average impedances 200 ∼ 700 Ω

3) Tissues with average impedance of more than 200 Ω*:* Fat is considered an electrical insulator [20] and hence has a high impedance as shown in Fig. 7. Cortical bone is compact bone which consists of densely packed osteocytes with no marrow spaces [21]. This contributes to the high impedance of the tissue as shown in Fig. 7.

From Fig. 8, skin and bone marrow have the widest impedance range. From the results, skin only exhibits low impedances at high frequencies, this indicates that only the

high frequency components of the lightning stroke current can penetrate the skin.

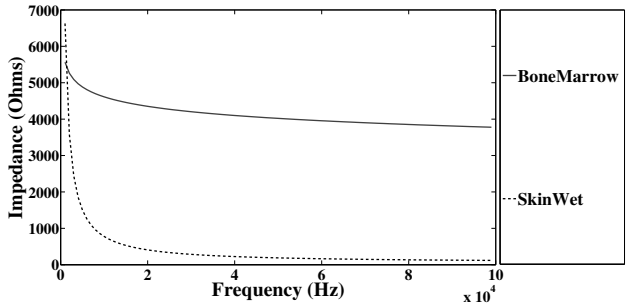

Fig. 8: Frequency vs Impedance of tissues which have a wide range of impedance

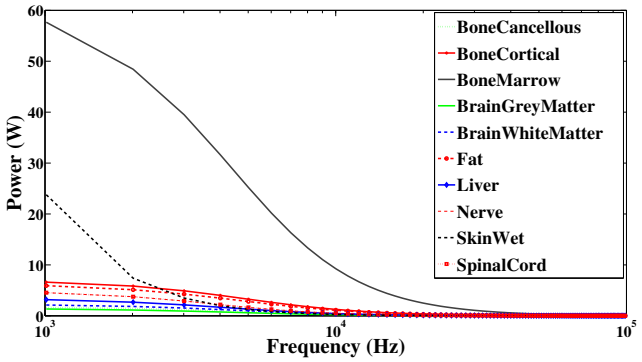

Fig. 9: Frequency vs Power of tissues which have a wide range of impedances

C. Power absorbed

The power absorbed by the tissue model at various frequencies is calculated by the volume integration of power over the cylinder. The power losses into the surrounding air is not calculated as only the electromagnetic effects of the tissue is concerned. The power absorbed corresponds to the current waveform and impedance of the tissue. From the results shown in Fig. 9, power absorbed by the tissue is proportional to the impedance of the tissue. Skin and bone marrow have the highest impedance and hence absorb the most power. The tissues with average impedances less than 100 Ω are not shown in Fig. 9.

D. Lightning injuries

The three main categories of lightning injuries are: neurological injuries, cardiac injuries and external burns [9]. From the results of the tissue models, these injuries can be correlated with the impedances of the tissues. Current pathway is established along the route of least impedance and hence tissues with low impedances are at more risk. The brain and the spinal cord are immersed in cerebrospinal fluid which has the lowest impedance out of all the tissues. Hence, current is likely to cause neurological damage to the brain and spinal cord by traversing through the cerebrospinal fluid. All internal organs of the body are immersed in fluids and since blood and body fluids have the second and third lowest impedances, the lightning short stroke current can be assumed to traverse all organs in the body. The heart has the lowest impedance compared to other organs and hence more current travels through the heart resulting in cardiac injuries. Assuming attachment of the lightning short stroke has occurred, the skin is the initial contact point. Since the skin has a high impedance, large amount of energy is required to establish a current pathway through the skin which results in heat generation and causes external burns.

The severity of the lightning injury also depends on the point of contact of the lightning stroke with the body. The current pathway is dependant on the impedances of the tissues and since the body is composed of heterogeneous tissues, the point of contact is a significant factor in determining the current pathway.

VI. Future Work

The simulation results are based on tissue models that have the same size and shape. These results are then used to explain the possible current pathway through the human body base on different tissue impedances. However, real human tissues are of various sizes and shapes and are mostly not homogeneous. An anatomical voxel model of the human body using the dielectric properties of tissues described in this paper can be used to obtain more realistic results.

The power losses can be further analysed in terms of energy by considering resistive losses. This can be used in the analysis of heating effects of various tissues under various frequencies of the lightning stroke.

Other mechanisms of lightning injuries such as side flash, contact voltage and step voltage as described by Lee [8] can be included using the same model and approach described in this paper.

VII. CONCLUSION

The current waveform of the first short stroke of the lightning flash is characterised by the use of the double exponential model. Fourier transform is applied to the double exponential model to obtain the frequency components. Only the first short stroke of the lightning flash and the direct strike mechanism of injury is considered in this paper. COMSOL is used to construct nineteen cylindrical models using the dielectric properties of various human tissues. AC waveforms corresponding to the frequency components are passed through the models and the current density, complex impedance and power losses are calculated. The impedances of the tissues

reflect properties of real tissues which are used to explain well known lightning injuries. The approach and results of this paper can be applied to an accurate human body voxel model to observe the current pathway through the human body. Other lightning injury mechanisms can be analysed using the approach and results of this paper.

ACKNOWLEDGEMENTS

The authors would like to thank CBI-electric for funding the Chair of Lightning at the University of the Witwatersrand and for direct support of the Research Group. They would also like to thank Eskom for the support of the Lightning/EMC Research Group through the TESP programme. Thanks are extended to the department of Trade and Industry (DTI) for THRIP funding as well as to the National Research Foundation (NRF) for direct funding of the Research Group.

REFERENCES

[1] *Protection Against Lightning-Part 1: General Principles*, Int. Std. IEC 62305-1, Jan. 2006.

[2] *High-voltage test techniques-Part 1: General definitions and test requirements*, Int. Std. IEC 60060-1, Feb. 2006.

[3] *Assessment of the Risk of Damage Due to Lightning*, Int. Std. IEC 61662, Apr. 1995.

[4] *IEEE Guide for Safety in AC Substation Grounding*, Int. Std. IEEE 80-2000, Jan. 2000.

[5] J. Wang and X. Zhang, "Double-Exponential Expression of Lightning Current Waveforms," in *The 2006 4th Asia-Pacific Conference on Environmental Electromagnetics*. Ieee, Aug. 2006, pp. 320–323.

[6] S. Vujević and D. Lovrić, "Exponential approximation of the Heidler function for the reproduction of lightning current waveshapes," *Electric Power Systems Research*, vol. 80, no. 10, pp. 1293–1298, Oct. 2010.

[7] D. Andreuccetti, R. Fossi, and C. Petrucci, "An Internet resource for the calculation of the dielectric properties of body tissues in the frequency range 10 Hz - 100 GHz," *Website at http://niremf.ifac.cnr.it/tissprop/*, vol. IFAC-CNR.

[8] W. R. Lee, *Lightning Injuries and Death*. London: Academic Press, 1977, ch. 16, pp. 521–543.

[9] C. J. Andrews and M. A. Cooper, *Clinical Presentation of the Lightning Victim*. CRC Press, 1992, ch. 5, pp. 47–68.

[10] V. A. Rakov and M. A. Uman, *Lightning: Physics and Effects*. Cambridge University Press, 2007.

[11] H. Wei, X. Ba-lin, and G. You-gang, "Analysis of the lightning waveshape," in *2004 Asia-Pacific Radio Science Conference, 2004. Proceedings.* IEEE, 2004, pp. 627–630.

[12] F. Heidler, "Analytical lightning current function for LEMP-calculation, translation from German," *International Conference on Lightning Protection (ICLP)*, vol. 18, pp. 63–66, 1985.

[13] F. Ruan, T. Dlugosz, D. Shi, and Y. Gao, "Cylinder model of human body impedance based on proximity effect," in *Microwave, Antenna, Propagation and EMC Technologies for Wireless Communications, 2009 3rd IEEE International Symposium on*, Oct. 2009, pp. 16–19.

[14] J. Werner and P. Webb, "A Six-cylinder Model of for General Use on Human Thermoregulation Personal Computers," *The Annals of physiological anthropology*, vol. 12, no. 3, pp. 123–134, 1993.

[15] D. Muramatsu, F. Koshiji, and K. Sasaki, "Multilayered cylindrical human arm model for impedance analysis in human body communication," in *Communications (APCC), 2012 18th Asia-Pacific Conference on*, Oct. 2012, pp. 478–479.

[16] D. C. Wolf, "Evaluation of the Size, Shape, and Consistency of the Liver," in *Clinical Methods: The History, Physical, and Laboratory Examinations*, 3rd ed., H. Walker, W. Hall, and J. Hurst, Eds., Boston, 1990, vol. 62, no. 6, ch. 94, pp. 478–481.

[17] R. Pethig and D. B. Kell, "The passive electrical properties of biological systems: their significance in physiology, biophysics and biotechnology," *Physics in Medicine and Biology*, vol. 32, no. 8, p. 933, 1987.

[18] C. Lote, *Principles of Renal Physiology*, 5th ed. Springer, 2012.

[19] J. A. Latikka, J. A. Hyttinen, T. A. Kuurne, H. J. Eskola, and J. A. Malmivuo, "The conductivity of brain tissues: comparison of results in vivo and in vitro measurements," in *Engineering in Medicine and Biology Society, 2001. Proceedings of the 23rd Annual International Conference of the IEEE*, vol. 1, 2001, pp. 910–912 vol.1.

[20] T. Ito, S. Yamada, and H. Kazama, "Measurement of Body Fat Distribution by Using Electrical Impedance Tomography," in *SICE-ICASE, 2006. International Joint Conference*, Oct. 2006, pp. 2551–2554.

[21] C. M. Langton and C. F. Njeh, *The Physical Measurement of Bone*, ser. Series in Medical Physics and Biomedical Engineering. Taylor & Francis, 2003.